BREAST CANCER DETECTION ON AUTOMATED 3D ULTRASOUND WITH CO-LOCALIZED 3D X-RAY.

by

Sumedha Sinha

A dissertation submitted in partial fulfillment
of the requirements for the degree of
Doctor of Philosophy
(Biomedical Engineering)
in The University of Michigan
2010

Doctoral Committee:

Professor Paul L. Carson, Chair
Professor Jeffrey A. Fessler
Professor J. Brian Fowlkes
Professor Mitchell M. Goodsitt

ACKNOWLEDGMENTS

I was fascinated by the term 'Biomedical Engineering' the first time I heard it and I have wanted to work at the interface of engineering and medicine ever since. Fortunately, I have been afforded the privilege of studying and working with extremely intelligent and motivated people at one of the best Universities in the world. During the course of my research, I have occasionally thought of the direst predictions of the witches of Macbeth, but on the whole, I must admit it has been rather a pleasant experience!

First and foremost, I would like to thank my advisor Dr. Paul Carson for his great ideas, joie de vivre and unwavering support. I would also like to thank the other members of my dissertation committee, Dr. Mitchell Goodsitt, for his attention to detail, Dr. Brian Fowlkes, who can always put things in the proper perspective, and Dr. Jeffrey Fessler, who provided invaluable guidance. I thank Dr. Ernest Madsen at the University of Wisconsin, Madison, who made a special effort to deliver our breast phantom in a short time frame. I would also like to thank Dr. Charles Meyer for his support, and express my gratitude to Dr. Marilyn Roubidoux and the other radiologists at the Breast Imaging Clinic for being generous with their time. In addition, I must thank all my other teachers, not just at the University of Michigan, but also during my high school and undergraduate years in India.

Many more names come to mind. Dr. Bing Ma, a faithful friend with whom I have shared many enjoyable Friday lunches, and who can usually simplify complicated situations for me. Another loyal friend, PhD candidate Fong Ming Hooi, granted the dubious appellation of my partner in crime, whose unfailingly optimistic response to

any frantic communications is usually ‘Oh, but that’s OK, because...’.

The very German Dr. Oliver Kripfgans, who is always ready with a helping hand and has often made me smile with his quicksilver repartee, the very French Dr. Frederic Padilla, who frequently found the time for obscure discussions, academic or not, PhD candidate Mario Fabiilli (count the ‘i’s), and all the other Professors, postdocs and graduate students in the Basic Radiological Sciences Division. Sharon Karahan and Carol Cribbins for wonderful administrative support.

Finally, let me thank my family. Their unconditional love and support has carried me through many difficult times. My parents, Usha and Prashant Sinha, who applied the Pareto principle to our upbringing; if they got the important 20% right, the rest was noise. My father, who can explain anything better than almost anybody I know, my mother, who set high standards but loved us anyway if we fell short. My sister Jayita, who is also working toward a PhD and who has undying faith in her big sister. My grandparents, who would be proud if they were alive today.

Ann Arbor, Michigan

July, 2010

TABLE OF CONTENTS

LIST OF FIGURES

Figure

LIST OF TABLES

Table

ABSTRACT

Breast cancer detection on automated 3D ultrasound with co-localized 3D x-ray

by

Sumedha Sinha

CHAIR: Paul L. Carson

X-ray mammography is the gold standard for detecting breast cancer while B-mode ultrasound is employed as its diagnostic complement. This dissertation aimed at acquiring a high quality, high-resolution 3D automated ultrasound image of the entire breast at current diagnostic frequencies, in the same geometry as mammography and its 3D equivalent, digital breast tomosynthesis, and to extend and help test its utility with co-localization. The first objective of this work was to engineer solutions to overcome some challenges inherent in acquiring complete automated ultrasound of the breast and minimizing patient motion during scans. Automated whole-breast ultrasound that can be registered to X-Ray imaging in the same geometry eliminates the uncertainty associated with hand-held ultrasound. More than 170 subjects were imaged using superior coupling agents tested during the course of this study. At least one radiologist rated the usefulness of X-Ray and ultrasound co-localization as high in the majority of our study cases. The second objective was to accurately register tomosynthesis image volumes of the breast, making the detection of tissue growth and deformation over time a realistic possibility. It was found for the first time to our knowledge that whole breast digital tomosynthesis image volumes can be spatially registered with an error tolerance of 2 mm, which is 10% of the average size of cancers in a screening population.

The third and final objective involved the registration and fusion of 3D ultrasound image volumes acquired from opposite sides of the breast in the mammographic geometry, a novel technique that improves the volumetric resolution of high frequency ultrasound but poses unique problems. To improve the accuracy and speed of registration, direction-dependent artifacts should be eliminated. Further, it is necessary to identify other regions, usually at greater depths, that contain little or misleading information. Machine learning, principal component analysis and speckle reducing anisotropic diffusion were tested in this context. We showed that machine learning classifiers can identify regions of corrupted data accurately on a custom breast-mimicking phantom, and also that they can identify specific artifacts on *in vivo* breast images. Initial registrations of the phantom image sets with many regions of artifacts removed provided robust results as compared to the original datasets.

CHAPTER I

Introduction

1.1 Motivation

Breast cancer takes the heaviest toll of all cancer-related deaths among women worldwide [WHO, 2009]. One in ten women will develop breast cancer at some time in her life and women living in North America have the highest rate of breast cancer in the world [ACI 2006]. X-ray mammography is the most widely used screening tool for breast cancer detection while the most readily accepted use of ultrasound (US) in the United States has been diagnostic, in distinguishing a simple cyst from a solid lesion[Kolb et al., 2002, Moss et al., 1999, Novak, 1983, Taylor et al., 2002]. Stavros et al. [Stavros et al., 1995] stated that if all the criteria for a simple cyst are met, the accuracy of US is 96-100%. Furthermore, they identified benign solid lesions in ultrasound images with a 99.5% negative predictive rate. However, on the subject of the operator dependence of hand-held ultrasound [Baker et al., 1999, Conway et al., 1991], Conway et al. stated that: "In five of 50 cases, masses detected with freehand US and initially believed to correspond to the mammographically detected mass were subsequently found to represent different areas of the breast." Automated whole-breast ultrasound that can be registered to X-Ray imaging in the same geometry eliminates some of this uncertainty by pinpointing the lesion's location in the breast, ensuring that the relevant mass is found and also avoiding confusion between multiple masses. Co-localization with

MRI would also be helpful since MRI has demonstrated efficacy for a high-risk population [Saslow et al., 2007] but this particular aspect has not been addressed in this work. The main advantage of ultrasound imaging in this context lies in its superior ability to identify and cull benign masses and cysts, in addition to being cost-effective and independent of potentially harmful contrast agents [Goldberg et al., 1994].

We are developing an automated ultrasound-tomosynthesis system wherein a digital X-ray tomosynthesis unit has been augmented with a motorized ultrasound transducer carriage above a special compression paddle [Carson et al., 2004, Kapur et al., 2004, LeCarpentier et al., 1999]. This system allows for the acquisition of 3D X-ray and ultrasound images in the same geometry. The first objective of this work was to engineer solutions to overcome the challenges inherent in acquiring complete automated ultrasound of the breast and minimizing patient motion during scans. The second objective was to accurately register tomosynthesis images of the breast acquired at different times, and test the usefulness of geographical correlation between 3D X-Ray and ultrasound. For screening, co-localization may be essential to retain the sensitivity of ultrasound in detecting additional cancers without introducing a higher fraction of false positives or call-backs. The third and final objective involved the acquisition of volumes of opposed view images (OVI) from the top and the bottom of the breast, using pulse echo B-mode ultrasound. With ultrasound, there is a trade-off between imaging depth and resolution due to the fact that higher frequencies, which provide finer resolution, are attenuated disproportionately. Relatively low frequencies are needed for depth penetration of more than 4 cm. To retain the resolution of high frequency ultrasound [Rizzatto et al., 1997], we can image the breast from both sides in the mammographic geometry (i.e., breast compressed between two plates), which we will refer to as dual-sided imaging. The goal is to register and fuse these volumes to produce a high

resolution, high quality 3D ultrasound image of the complete breast. This is a novel, feasible technique for higher quality images formed by registering and fusing opposite views. The improved resolution at higher frequencies will facilitate detection of micro-calcifications [Cleverley et al., 1997, Nagashima et al., 2005] and estimation of tumor margins [Kolb et al., 1998], characteristics highly indicative of breast cancer.

1.2 Background of Thesis

1.2.1 Improvements in current scanning techniques

3D automated ultrasound (US) is rarely acquired in the mammographic geometry, due to the technical problems associated with this configuration. Automated US systems with other configurations have been built and tested recently with good results. Jackson et al. [Jackson et al., 1993] and U-Systems [Wenkel et al., 2008] described a system that requires the patient to lie supine, whereas Shipley et al. [Shipley et al., 2005], Duric et al. [Duric et al., 2007] and Gooding et al. [Gooding et al., 2010] described a system that needs the patient to lie prone. However, accurate mechanical registration with mammograms is not possible in such a setup. Richter et al. [Richter et al., 1997] achieved some success in lesion characterization with a system on which 3D automated US could be acquired in the mammographic geometry, but emphasized the need for technical improvement.

Automated ultrasound images can be acquired with the dual-modality system in the conventional mammography views: cranio-caudal (CC), medial-lateral-oblique (MLO), lateral-medial-oblique (LMO), lateral-to-medial (LM), and medial-to-lateral (ML). On our automated US system, images were initially acquired through a TPX (4-methylpentene-1 based polyolefin) plastic compression paddle [Booi et al., 2007] a device used to compress the breast in mammography, and later through a fiber mesh paddle. Compression reduces image degradation due to motion, x-ray scatter and x-ray beam hardening, and lowers the required radiation dose. Inasmuch as a longer

duration of compression is necessary for automated ultrasound, a compression force of about 4 to 10 dN is typically used with the dual-modality system to minimize patient discomfort while stabilizing the breast. (The FDA specifies a maximum compression force of 17.7 dN in Rule 663(4) of the Ionizing Radiation Rules.) The ultrasound transducer is placed in a holder that is attached to an x-y translator drive, which moves the transducer across the compression paddle under computer control. One to three adjacent automated US transducer sweeps are performed as needed for the area of coverage, depending on the shape and size of the patient's breast. The 3D US images obtained are later registered and fused in order to visualize the entire breast volume. The first important consideration is to image the entire breast with US. Stacey-Clear et al. [Stacey-Clear et al., 1993] observed that 73% of the 86 cancers they studied were "found at the periphery of the breast as defined by a zone 1 cm wide beneath the subcutaneous fat or anterior to the retro-mammary fat". This zone may include up to 50% of the breast volume, owing to the hemispheric shape of the breast. Hence, including this region in the ultrasound scan is of the utmost importance on our dual modality system. Other considerations include improving the quality of the adhesive coupling between the ultrasound transducer and the skin surface and stabilizing the breast while in compression.

Solutions to the technical problems described above would ensure that the peripheral region of the breast is included in the 3D automated US image and that fusion of multiple US sweeps into a seamless image volume [Chang et al., 2010, Tozaki et al., 2010] is not compromised by motion artifacts. Consequently, mechanical registration of 3D US and tomosynthesis would result in more accurate localization and characterization of the suspected lesion(s).

1.2.2 Tomosynthesis image registration

In this study, 3D digital X-ray tomosynthesis [Claus et al., 2006, Eberhard et al., 2006, Zhang et al., 2006] and 3D automated ultrasound images of patients' breasts were

acquired in the same geometry with a unique dual-modality system. X-ray tomosynthesis shows great promise for use as a primary screening tool in breast imaging and its efficacy in detection and assessment is enhanced by anatomic correlation with an automated ultrasound scan acquired in the same geometry. It would be a decided advantage to be able to register pairs of these images before and after chemotherapy, to measure the change in volume of the malignant lesion and compare measurements to those obtained with automated ultrasound. At the time of detection, the average breast tumor diameter is 21 mm. [Sickles et al., 2005, Sommer et al., 2003] Registration should be able to detect at worst a 10% change in tumor size. Therefore our goal was a registration error of less than 2 mm.

Meyer et al. [Meyer et al., 1999] reported early success with volumetric US registration and Krucker et al. [Krücker et al., 2000] reported registration error values of 0.31 mm on a phantom image and 0.65 mm *in vivo*. Narayanasamy et al. [Narayanasamy et al., 2007] were able to register 9 out of 10 pairs of automated grayscale ultrasound images to each other with a mean error of 1.2 mm +/- 0.9 mm. These were repeat scans with less than 15 minutes between the two acquisitions. If changes in lesion volume can be measured on 3D tomosynthesis images as well as 3D ultrasound images, this further enhances the usefulness of dual modality breast imaging.

Registration of breast tomosynthesis images had not been attempted in the past and I had the opportunity to use MIAMIFUSE [Kim et al., 1997, Meyer et al., 1997, Meyer et al., 1999] for this attempt. Accuracy was limited by the poor axial resolution of the tomosynthesis images (1 mm) and angle-dependent artifacts.

1.2.3 Multi-modality mass characterization

Ultrasound images aid the radiologist in assessing the malignancy of a suspicious mass seen on the X-ray image, especially in identifying benign masses (e.g., cysts) to prevent unnecessary biopsies. Kotsianos-Hermle et al. showed 72%

correlation between automated ultrasound and manual ultrasound in a recent study [Kotsianos-Hermle et al., 2009]. True and exact co-location of a suspicious mass with 3D mammography is possible only with mechanically registered automated ultrasound. When the lesion(s) of interest is visible in both modalities, anatomic correlation afforded by the dual modality system localizes the mass within the breast with more accuracy. Richter et al. [Richter et al., 1997] stated that a combination of mammography and B-mode automated ultrasound was successful in detecting 83-92% (by 4 readers) of 41 malignant lesions in their study. The radiologist's level of confidence in identifying the lesion of interest in both the X-ray and ultrasound images increases to certainty when mechanical registration is used for co-location.

1.2.4 Opposed view whole breast imaging

Automated 3D US does present good potential for screening purposes [Kelly et al., 2010, Lister et al., 1998], especially for women with dense breasts [Kolb et al., 1998, Jackson et al., 1993]. Kolb et al. stated that forty-two percent of non-palpable cancers in their study would not have been detected without screening US (all of these cancers were in dense breasts). However, the poor image quality of automated US and technical problems in its implementation have prevented mainstream clinical adoption. Where hand-held ultrasound is concerned, it is possible to position the transducer directly above the lesion at a minimally aberrating orientation, but this is not possible with automated ultrasound.

Attempts have been made to improve the quality of 3D automated US to a level where it can and should be used routinely for screening. Carson et al. [Carson et al., 1981] first discussed the use of ultrasound pulse echo imaging in conjunction with transmission ultrasound tomography. Andre et al. [Andre et al., 1999] and Duric et al. [Duric et al., 2007] achieved some success with ultrasound tomography, where they employed both reflection and transmission imaging. However, Duric et al could only achieve an out-of-plane resolution of 12 mm

and they were unable to detect masses of size <15 mm. Transmission imaging had an in-plane resolution of 4 mm, which compares poorly with the in-plane resolution of pulse echo US which is less than 0.5 mm. Shipley et al. [Shipley et al., 2005] documented a volumetric automated US system with specialized attenuation compensation (using information from backscatter), wherein the patient lay prone and the breast was held in a cone. However, none of these ultrasound scanning techniques involved image acquisition in the same geometry as a mammogram and hence could not implement mechanical registration or co-location.

Pulse echo or B-mode ultrasound in the mammographic geometry is a more feasible technique for screening applications, especially when opposed view images are acquired (dual-sided imaging). A unique approach to 3D grayscale ultrasound is proposed wherein the breast will be imaged along the same plane but from opposite sides. Opposing image volumes can be registered, possibly compounded [Moskalik et al., 1995, Krücker et al., 2000, Krücker et al., 2002] and fused. Artifacts caused by shadowing and refraction would be minimized. The finer resolution and increased sensitivity to small scatterers at higher frequencies [Rizzatto et al., 1997], will also facilitate the detection of small scatterers in solid hypoechoic lesions and their discrimination from fat and cysts, besides improving the visibility of tumor margins. The opposing images thus obtained can be fused together, using the information in the overlap region for intrinsic registration.

Dual-sided imaging would also allow the use of frequencies at 10MHz or higher, since the image from either side need not cover the entire thickness of the breast. Compression thickness for the average breast is between 4 and 5 cm; Helvie et al. [Helvie et al., 1994] documented a mean compression thickness of 4.4 cm in the cranio-caudal view and 4.8 cm in the mediolateral oblique view in a study population of 250 paired mediolateral oblique and craniocaudal mammograms. Hence depth penetration of more than 3 cm will rarely be required on either side of the average

breast, further strengthening the case for imaging at a frequency equal to or greater than 10 MHz, as opposed to a lower frequency such as 7.5 MHz. Frequencies in this range are commonly used clinically for B-mode breast ultrasound. Roubidoux et al. [Roubidoux et al., 2005] documented results obtained with the GE M12L at 9 MHz. However, since automated ultrasound requires greater depth penetration than the far more flexible hand-scanning technique, investigators have been wary of using higher frequencies for single-sided imaging.

Opposed view images can be taken within minutes or even seconds of each other. However, success in registration of these images is complicated by the low signal-to-noise ratio (SNR), poor resolution and refraction and attenuation artifacts in the central region of the breast where the two views will overlap. The replacement of a TPX paddle with a mesh paddle has done away with one of the biggest drawbacks of the former setup by reducing attenuation [Booi et al., 2007] and facilitating good acoustic coupling. Opposed view imaging through a filament mesh paddle results in superior contrast, spatial resolution and a higher SNR. It is possible that these images will be of a quality that justifies their use for screening purposes, especially for subjects with dense breasts.

From our knowledge of the relevant literature, this is the first time that opposed view ultrasound imaging of the breast has been attempted in the mammographic geometry, with potential for automation and registration with tomosynthesis.

1.3 Contributions of Thesis

Both quantitative and qualitative advancements were made in automated ultrasound whole-breast scanning and its co-localization with tomosynthesis.

With regard to obtaining better image quality for our existing system, several innovations were made with the author's participation [Sinha et al., 2007a]. Filling the gaps between the breast and compression paddle with a highly viscous ultrasound

gel using a syringe reduced gap lengths by about 60%. This solution was only partial as 73% of malignant lesions are present at the periphery of the breast, as defined by a zone 1 cm wide beneath the subcutaneous fat or anterior to the retromammary fat. However, it is possible to image the axillary tail and extreme medial regions of the breast better by using lateral views. The subareolar region can be imaged better by compressing the breast such that the nipple is closer to the TPX paddle, therefore reducing the gap between the paddle and the subareolar region. Breast slippage is a problem with coupling gel between the paddle and the breast. An adhesive hairspray was found to provide acoustic coupling of the compression paddle to the breast. This coupling agent preserved image quality, was empirically found to be a close second-best for adhesively coupling the breast to the paddle and was easy to remove and clean up. Viscous bubble-free ultrasound gel proved most effective for coupling the transducer to the paddle for LM views, when the paddle is vertical. As of the current date, more than 170 subjects have been imaged in CC and LM views of the affected breast using the experimentally determined superior coupling agents. Patient motion artifact analysis carried out in both B-mode and IQ mode proved that shallow patient breathing and breath-hold were not harmful to image quality, whereas speech and sudden breathing produced unacceptable artifacts. By aiding the stabilization of the compressed breast, we succeeded in minimizing technical difficulties in image splicing and registration caused by slippage of the breast.

We found for the first time to our knowledge that whole breast digital tomosynthesis mammography image volumes taken at different times can be spatially registered [Sinha et al., 2009]. The registration process was complicated by several factors; primarily, the compression of the breast at different times results in different mammographic appearances. Digital tomosynthesis mammographic volumes also contain reconstruction artifacts that are dependent on the viewing angle. Furthermore, these digital tomosynthesis mammographic images have a

slice thickness of 1 mm (this value can vary from 0.1 mm to half the lateral extent of the image for simpler reconstruction algorithms), depending on the extent of target object in the direction of x-ray tube motion. The axial resolution is clearly poorer than the 0.1 mm x 0.1 mm resolution in the image plane (voxel size was 0.1 x 0.1 x1 mm^3). With care in selecting nearly identical locations in each of two same-modality image volumes of the breast as control points, image based registration was quite successful. Although the achieved average registration error of 2 mm is relatively large compared to the tomosynthesis resolution of 0.1 mm, this error is small compared with the average size of mammographically detected breast cancers in a screening population. A tolerance of +/- 10% in tumor diameter change estimation(average tumor size at first detection is 20 mm [Sickles et al., 2005, Sommer et al., 2003]) in this first attempt at tomosynthesis registration is promising.

When digital breast tomosynthesis was compared to mammography, tomosynthesis outperformed mammography in mass detection (BIRADS 3 to 5), mass margin delineation and cancer detection. When automated ultrasound was compared to clinical hand ultrasound, it was consistently judged as inferior. However, when lesions were detected on automated ultrasound, mean correlation between the radiologists' assessments of percentage malignancy on the clinical hand US and the research auto US was 0.81. Hence, in spite of its limitations, automated US performed well enough to justify geographic co-location with tomosynthesis [Sinha et al., 2007b]. In this pilot study of 26 cases (See Fig 2), the mean ranking for usefulness of correlative imaging was moderate. At least one reader rated usefulness as high in 62% of our cases. On the whole, when lesions were visible in automated US, they were characterized with an accuracy comparable to that achieved with clinical hand US. Progress needs to be made in producing ultrasound scans with greater breast coverage, especially at the chest wall and the breast periphery. Automated US in

its current setup cannot replace clinical hand US for screening purposes but can aid radiologists in lesion detection and assessment.

Finally, significant progress was made in developing improved registration and fusion techniques for dual-sided imaging of the compressed breast. We expected extensive direction-dependent artifacts in the overlap zone and hence elimination of these artifacts was investigated. Principal component analysis and speckle reducing anisotropic diffusion were two of the noise-removal techniques we considered for this purpose. Our results imply that principal components may be somewhat useful in registration of locally warped breast ultrasound images that are partially obscured by noise. Implementing some form of edge detection or segmentation was an alternative approach, and finally, machine learning was successfully used for isolating noise and artifacts in ultrasound images [Sinha et al., 2010]. Machine learning has been used in the past to identify suspicious masses on ultrasound images [Kotropoulos and Pitas, 2003, Piliouras et al., 2004]. We achieved an accuracy of almost 100% for automated classification of true and corrupted ultrasound data obtained from a custom breast-mimicking phantom. For a limited *in-vivo* image set, we demonstrated that specific image artifacts, namely shadows and enhancements can be reliably separated from background image data, with an accuracy of more than 90%. This classification can be ported to a fusion algorithm that enables automated registration of images acquired from opposed views of the breast. Segmented images of the phantom could be registered successfully in 6 of 6 runs with different sets of control points, with an average error of 1.67 mm, while registration failed on the original image set in half of these runs, thus proving the utility of artifact removal in opposed view image registration.

1.4 Publications related to Thesis

1.4.1 Publications

- Sinha S.P., Narayanan R., Ma B., Roubidoux M.A., Liu H. and P.L. Carson,. Image Registration for Detection and Quantification of Change on Digital Tomosynthesis of Mammographic Volumes. *American Journal of Roentgenology, Cover*. 192: 384-387, February 2009.

- Sinha S.P., Goodsitt M.M., Roubidoux M.A., Booi R.C., LeCarpentier G.L., Lashbrook C.R., Thomenius K.E., Chalek C., and P.L. Carson. Automated Ultrasound Scanning on a Dual Modality Breast Imaging System: Coverage and Motion Issues and Solutions. *Journal of Ultrasound In Medicine*. 26: 645-655, May 2007.

- Yang Z., Sinha S.P., Booi R.C., Roubidoux M.A., Ma B., Fowlkes J.B., LeCarpentier G.L. and P.L. Carson. Breast Ultrasound Image Improvement By Pixel Compounding of Compression Sequence. *IEEE Transactions in Ultrasonics, Ferroelectrics and Frequency Control*. 56: 465-473, March 2009.

1.4.2 Conference Publications

- Sinha S.P., Hooi F.., Syed Z.H.., Pinsky R.W., Thomenius K.E., and P.L. Carson. Machine learning for artifact removal on breast ultrasound images. *Proceedings of IEEE Ultrasonics Symposium*. accepted, October 2010.

- Sinha S.P., Roubidoux M.A., Helvie M.A., Nees A.V., Goodsitt M.M., LeCarpentier G.L., Fowlkes J.B., Chalek C.L., and P.L. Carson. Multimodality 3D breast imaging with X-Ray tomosynthesis and automated ultrasound. *Proceedings of IEEE Engineering in Medicine and Biology Annual Conference*. 1335-1338, 2007.

- Yang Z, Sinha S.P., Booi R.C., Roubidoux M.A., Ma B, Fowlkes J.B., LeCarpentier G.L. and P.L. Carson. , Sub-Pixel Compounding From Elasticity Imaging Data, *Proceedings of SPIE International Symposium on Medical Imaging*. 1-8, 2007.

- Narayanasamy G, Naraynan R, LeCarpentier G, Fowlkes JB, Roubidoux MA, Sinha S, Zabuawala S, Carson PL, Non-rigid registration of three-dimensional (3D) grayscale and Doppler ultrasound breast images. *Proceedings of IEEE Engineering in Medicine and Biology Annual Conference*. 91-94, 2007.

1.4.3 Posters and Presentations

- Sinha S.P., Madsen E.L.., Frank G.R., Goodsitt M.M. and P.L. Carson. Ultrasonic breast-mimicking phantom for pulse-echo and transmission imaging. *Ultrasonic Imaging and Tissue Characterization Symposium*. Arlington,VA, 2010.

- Sinha S.P., Roubidoux M.A., Goodsitt M.M., Hadjiski L.M., Thomenius K., and P.L. Carson. Time-efficient mass localization on automated breast ultrasound with dual-modality information. *Annual Convention of the American Institute of Ultrasound in Medicine*. New York, NY, 2009.

- Sinha S.P., Narayanasamy G., Narayanan R., Roubidoux M.A., LeCarpentier G.L., Goodsitt M.M., Fowlkes J.B. and P.L. Carson. Image Registration for Change Detection and Quantification in Multimodality Breast Tomosynthesis and Ultrasound.*Annual Meeting of the American Association of Physicists in Medicine*. Minneappolis, MN, 2007.

- Sinha S.P., Roubidoux M.A., Goodsitt M.M., LeCarpentier G.L., Zabuawala S.I., Lashbrook C.R.., and P.L. Carson. Stabilization of the compressed breast and image processing for improved automated ultrasound. *Annual Conference*

of the Biomedical Engineering Society. Baltimore, MD, 2005.

CHAPTER II

Automated Ultrasound Scanning on a Dual Modality Breast Imaging System

2.1 Introduction

This study is part of a project aimed at improving the efficacy of breast cancer diagnosis and characterization by acquiring images of the breast in the same geometry with x-rays and ultrasound (US) [Carson et al., 2004, Kapur et al., 2004, LeCarpentier et al., 1999]. The automated ultrasound is acquired though a special compression paddle [Booi et al., 2007] that is also used for x-ray imaging. Possible ultrasound modes are: 3-D ultrasound in grayscale (B-mode), Doppler color flow imaging, elasticity imaging and compounding. This report focuses on grayscale ultrasound.

X-ray and ultrasound images can be acquired with the dual-modality system in the conventional mammography views: cranio-caudal (CC), medial-lateral-oblique (MLO), lateral-medial-oblique (LMO), lateral-to-medial (LM), and medial-to-lateral (ML). The ultrasound transducer is placed in a holder that is attached to an x-y translator drive, which moves the transducer across the compression paddle under computer control. One to three adjacent automated US transducer sweeps are performed as needed for the area of coverage, depending on the shape and size of the patient's breast. The 3D US images obtained are later registered and fused in order to visualize the entire breast volume. Fusion requires a high degree of accuracy.

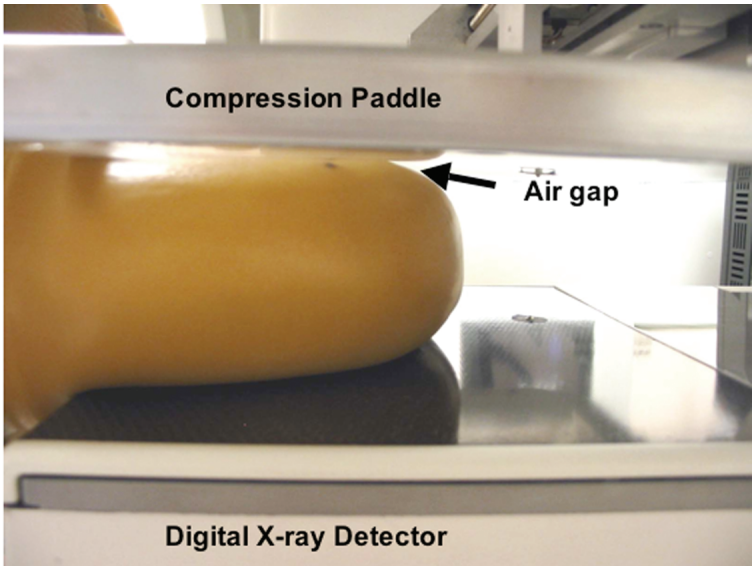

Figure 2.1: Photograph of breast-simulating phantom illustrating air gap between phantom and compression paddle at the periphery.

The final image volume is usually evaluated [Sahiner et al., 2007] in conjunction with a 3-D mammogram [Chan et al., 2005] (tomosynthesis). Two approaches to achieve adjacent sweep alignment are stabilizing the breast while in compression and post-processing (i.e., shifting, tilting, warping, etc.) the obtained images.

A major problem associated with performing ultrasound scans through a compression paddle is that there can be an appreciable air gap between the paddle and the breast surface near the breast periphery. This gap is illustrated in Fig. 2.1.

Since ultrasound is highly reflected at the paddle/air interface, and very little ultrasound at diagnostic imaging frequencies transmits through air, any region of the breast where there is such an air gap will not be visible in the ultrasound image. Our purpose was to investigate the magnitude of the US coverage problem and possible solutions.

An additional issue is how to minimize breast motion, and yet provide coupling of the breast to the compression paddle. Traditional US gels exhibit excellent US transmission properties, but are too slippery for maintaining the breast in a fixed position in contact with the paddle throughout scan times that can last several

minutes. In addition, patient motion due to breathing and speaking can create artifacts that distort the grayscale ultrasound image. Furthermore, breast slippage is undesirable for elasticity imaging, which may be implemented after the automated US sweeps are obtained by further compressing the human subject's breast in small increments up to an additional 5% strain (elasticity imaging carried out by R.C. Booi). Digitized radio-frequency (RF) signals acquired for elasticity studies are later correlated and displacement estimates are converted to strain images. Though elasticity imaging has proven to be a valuable diagnostic tool, like image fusion, it is very sensitive to breathing motion. We quantified four different motion artifacts for B-mode and IQ (In phase/Quadrature phase) RF data, and explored methods to minimize such artifacts.

2.2 Materials and Methods

IRB approval was obtained for this study (2002-0584, University of Michigan) and informed consent was obtained for every patient in these trials. Initially, testing was done on a first generation dual-modality ultrasound/digital mammography system consisting of a GE (General Electric Healthcare, Milwaukee, WI) LOGIQ 9 US system and a GE Senographe 2000D digital mammography unit. Subsequent testing was performed on a combined system consisting of a GE LOGIQ 9 US system and a second generation GE research tomosynthesis unit [Eberhard et al., 2006]. The US transducer that was employed was a GE M12L linear matrix array operating at maximum center frequencies of 10 to 12 MHz. The US system was augmented with a motorized transducer carriage that translated the transducer from left to right over a water-filled or gel-filled TPX (4-methylpentene-1 based polyolefin) plastic compression paddle of 2.5 mm thickness (see Fig. 2.2).

Water is employed as a coupling agent between the transducer and the paddle for CC-views and gel is employed for oblique and lateral views. Software developed

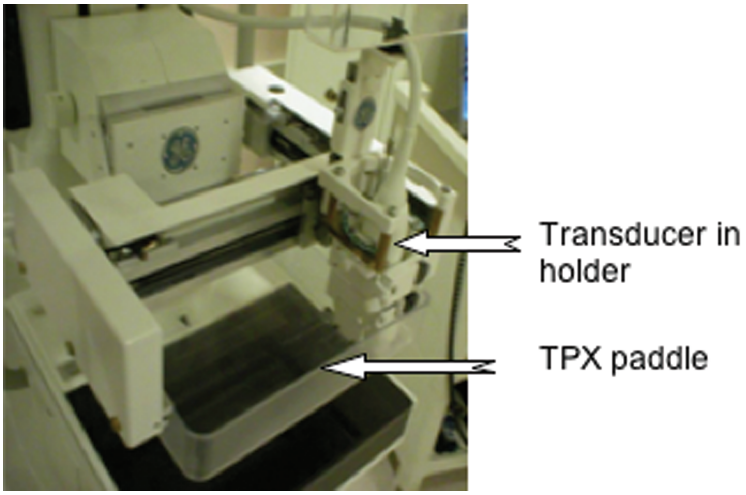

(a)

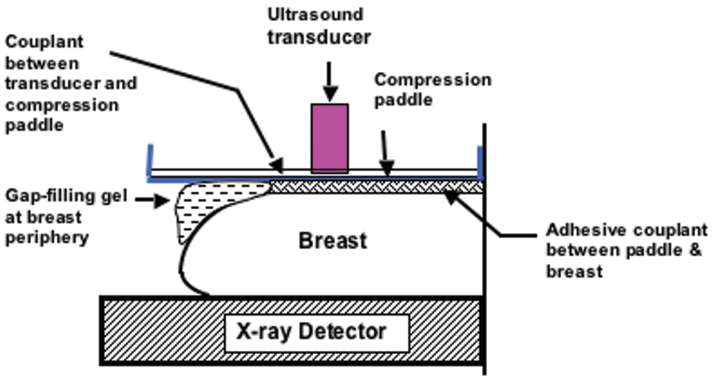

(b)

Figure 2.2: (a) Close-up of automated scanning equipment. (b) Schematic drawing illustrating relative positions of the breast, x-ray detector, transducer, compression paddle, and couplants. (Thickness of adhesive couplant is exaggerated for improved visibility in drawing.)

by GE Global Research is used to drive the motorized carriage.

The compression paddle is a device used to compress the breast in mammography, where compression reduces image degradation due to motion, x-ray scatter and x-ray beam hardening, and lowers the required radiation dose. Inasmuch as a longer duration of compression is necessary for automated ultrasound, a compression force of about 4 to 10 dN is typically used with the dual-modality system to minimize patient discomfort while stabilizing the breast.

2.2.1 Estimation of coverage

These experiments were carried out by M.M. Goodsitt. To estimate the fraction of the breast surface area that is in contact with the compression paddle, technologists made visual tracings of the paddle-to-breast contact region and the outer breast border on transparencies placed on the compression paddle. These tracings were drawn for 10 patients [7 with known breast cancer and 3 normal volunteers]. The tracings were then digitized with a flatbed scanner and analyzed with ImageJ, a public domain Java image processing program inspired by NIH Image [NIH, 2010] to measure the contact and total breast surface areas and the linear dimensions of the peripheral air gaps. To fill-in the air gap between the breast and the compression paddle at the curvature of the breast periphery, we developed a technique utilizing a syringe to dispense bubble-free gel at this location. The linear dimensions of the gap filled with US gel were estimated from US images of 10 different volunteers.

2.2.2 Couplant Selection

- Couplant between Breast and Compression Paddle

  To test agents for coupling the breast to the paddle, various adhesives were qualitatively assessed for the absence of coupling gaps and shear/ slippage resistance. The tests were carried out on a human wrist. These experiments were carried out under the supervision of M.M. Goodsitt. The compression

paddle was in the CC position and was filled with water for coupling the transducer to the paddle. The couplant candidates were then each applied to the wrist and the wrist was lightly compressed with the paddle. Gray-scale ultrasound images were then acquired of the same area of the wrist. The adhesive couplant candidates that were tested included included: Got2bglued hairspray (Schwarzkopf & Henkel, Irvine, CA), Gigahold hairspray (Continental Consumer products, Birmingham, MI), Skintac adhesive (Torbot Group Inc, Cranston, RI), SonTac Gel pads (Diagnostic Ultrasound Corporation, Bothell, WA), Shaped Gel Concept Pads (Gel Concepts, Whippany, NJ), Tensive Glue (Parker Laboratories, Fairfield, NJ), YES paste (Gane Brothers and Lane, Elk Grove Village, IL), Got2bglued spiking glue (Schwarzkopf & Henkel, Irvine, CA), and Poligrip dental paste (GlaxoSmithKline, Moon Township, PA). Aquasonic Gel (Parker Laboratories, Fairfield, NJ), a conventional ultrasound coupling gel was utilized as a gold standard for comparisons. In addition to the absence of gaps and good shear/slippage resistance, we also qualitatively evaluated image quality, ease of use and after-effects, if any.

Next these agents were quantitatively assessed by measuring the contrast-to-noise ratios in images of the 2.4 mm diameter anechoic and -9 dB cylindrical targets within a CIRS (Computerized Imaging Reference Systems, Inc., Norfolk, VA) Model 047 Gray Scale Contrast-Detail Ultrasound phantom. Cross-sectional B-mode images of these targets were taken at different depths (namely 2.5 cm and 4 cm) with and without an intervening 2.5 mm thick piece of TPX plastic. The TPX plate was a smaller version of the compression paddle that was more convenient to use when imaging the phantom. The coupling agents were placed between the TPX and the phantom scanning window. The resulting images were then analyzed to compute the contrastto-noise ratios within selected targets in the phantom. The contrast-to-noise ratio was

evaluated [van Wijk and Thijssen, 2002] as:

$$\mathrm{CNR} = \frac{(\mu_{\mathrm{t}} - \mu_{\mathrm{b}})}{\sigma_{\mathrm{rms}}} \tag{2.1}$$

where μ_t is the mean signal level in the target region of interest, μ_b is the mean signal level in the background region of interest and σ_{rms} is the root mean square noise in the background. μ_b and σ_{rms} were obtained as the average of mean and standard deviation values in six background ROIs in the phantom, at the same depth as the targets. We also obtained comparable images of a cyst in a patient's breast using Got2BGlued (the most viable coupling agent from our qualitative and quantitative results) and Litho Clear ultrasound gel. The CNRs for the cyst were evaluated using the formula above, picking six background ROIs all around the periphery of the cyst.

- Couplant between Transducer and Compression Paddle in ML and LM Views
  For coupling the transducer to the paddle in the LM and ML views, various gels, lotions and oils were qualitatively assessed for viscosity. These were Sonotech Litho Clear Gel (Sonotech, Bellingham, WA), Sonotech Clear Image Gel (Sonotech, Bellingham, WA), (Both Low and High Viscosity Types), Medichoice Gel (Owens and Minor, Richmond, VA), Polysonic lotion (Parker Laboratories, Fairfield, NJ), Aquasonic Gel (Parker Laboratories, Fairfield, NJ), General Imaging Gel (ATL, Reedsville, PA), Primrose Oil (Cedar Vale Natural Health, Crocker St. Cedar Vale, KS), Nutra-E Oil (Nature made Nutritional Products, Los Angeles, CA), Glycerin and three mixtures of Polysonic Gel with Litho Clear Gel (Ratios 1:2, 1:1 and 2:1). The parameters for this test were: gel movement after 3 minutes and after 6 minutes for a given layer thickness.

- Motion Analysis

Ultrasound image data were collected in B-mode and in IQ mode for analysis of artifacts caused by patient motion during scans. Automated full coverage ultrasound is carried out in B-mode; whereas, IQ data is collected (also in automated mode) during elasticity data acquisitions. Six (7 for elasticity) patient volunteers were asked to do the following during short stationary scans: (1) hold their breath, (2) take a deep breath and release it, (3) breathe shallowly and (4) talk (repetition of a single phrase). Every image was split into eight regions and each of these regions was correlated individually across successive image frames at the pixel level. The minimum observed correlation was noted for each region. Elasticity data was correlated at the sub-pixel level over the whole image and average correlation was noted. Furthermore, the correlation maintained in successive image frames was checked over time for a stationary scan. This was done to quantify the maintenance of adhesive properties over time.

To best splice adjacent US sweep images into a 3-D volume, it is advisable to include redundant data in the form of an overlap between sweeps. The automated US scanning system was programmed to scan the breast with an overlap of 1 cm between adjacent sweeps. The actual overlap could be different due to possible bowing of the compression paddle, looseness of the transducer holder, etc. The true overlaps or shifts were determined using the AVS (Advanced Visual Systems Inc., Waltham, MA) Miami Fuse registration application.

2.3 Results and Discussion

2.3.1 Estimation of coverage

Examples of the visual traces of the breast-paddle contact areas and breast outer boundaries are shown in Fig. 2.3. The percentages of breast area in contact with the

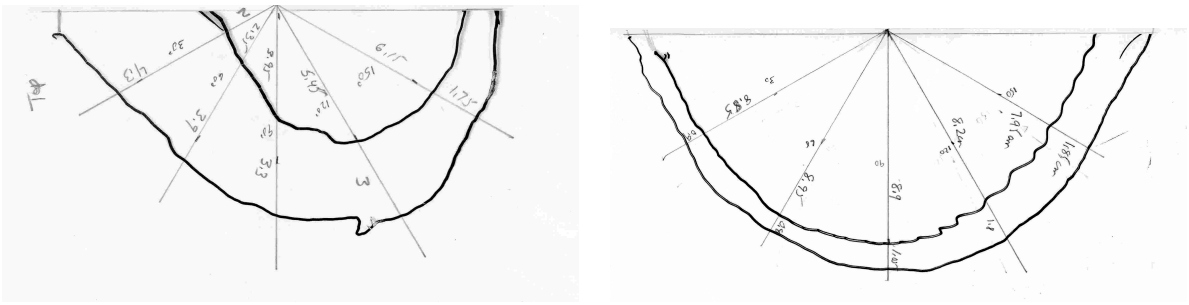

(a) (b)

Figure 2.3: (a)Worst case visual tracing of breast in contact with the paddle (inner curves) and outer breast borders .The area of the breast in contact with the paddle is 28.7 cm^2 and the total breast area is 81.9 cm^2, yielding the minimum contact area of 35%. (b)Best case visual tracing of breast in contact with the paddle (inner curves) and outer breast borders. The area of the breast in contact with the paddle is 80.2 cm^2 and the total breast area is 108 cm^2, yielding the maximum percentage area in contact with the paddle of 74%

compression paddle from the visual tracings without gel are listed in Table 2.1.

The percentages of the breast area in contact with the paddle ranged from 35% (Fig. 2.3a) to 74% (Fig. 2.3b) with a mean of 56% 15%. The linear dimensions of the gaps between the border of the contact region and the outer border of the breast in the tracings are listed in Table 2.2. These gaps were measured at 4 different angles relative to the approximate centers of the breasts at the chest wall [See Fig. 3] For these 10 patients, the gap dimensions ranged from 0.8 cm to 4.3 cm with a mean of 2.2 cm 0.9 cm.

Analysis of the B-mode ultrasound images obtained with the automated system on 10 different volunteers who were subsequently scanned with the gaps filled-in with gel indicated that had gel not been employed, air gaps would have ranged between 0.7 cm and 4.7 cm (mean= 1.7 cm +/- 0.6 cm). The analysis also indicated the percentage of the linear dimensions of the gaps that were filled-in with gel ranged from 42% to 85% with a mean of 61% +/- 10%.

Fig. 2.4 is a B-mode single slice from a 3-D US volume showing how gel fill-in improves breast coverage. Most of the breast beneath the gel-fill region shown in

Subject	Area in contact with paddle(cm^2)	Total breast area (cm^2)	Percentage of breast area in contact with paddle (%)
1	114.8	154.4	74.4
2	65.6	103.7	63.2
3	28.0	62.7	44.7
4	51.9	105.0	49.4
5	735.7	84.7	42.2
6	36.2	80.1	45.2
7	28.7	81.9	35.1
8	126.9	193.1	65.8
9	80.2	108.4	73.9
10	50.4	71.6	70.4

Table 2.1: Percentage of Breast Area in Contact with the Compression Paddle from Visual Tracings (No Gel).

Non-contact Gaps at Breast Periphery (cm)					
Subject	30 degrees	60 degrees	90 degrees	120 degrees	150 degrees
1	0.9	0.8	1.05	1.8	1.85
2	3.6	2.6	2.7	3.1	2
3	3.2	2.5	2.1	2.35	1.8
4	3.85	3.25	3.55	2.7	1.6
5	3.85	2.25	2.1	1.5	1.4
6	2	2.2	3.1	2.9	2.6
7	4.3	3.9	3.3	3	1.75
8	2.6	2.3	2.25	1.75	1.6
9	1.3	0.9	1.45	1	1.1
10	0.85	1	1.9	1.45	1.1

Table 2.2: Linear dimensions of the gaps at the breast periphery from Visual Tracings (No Gel).

this figure would not have been imaged without the gel.

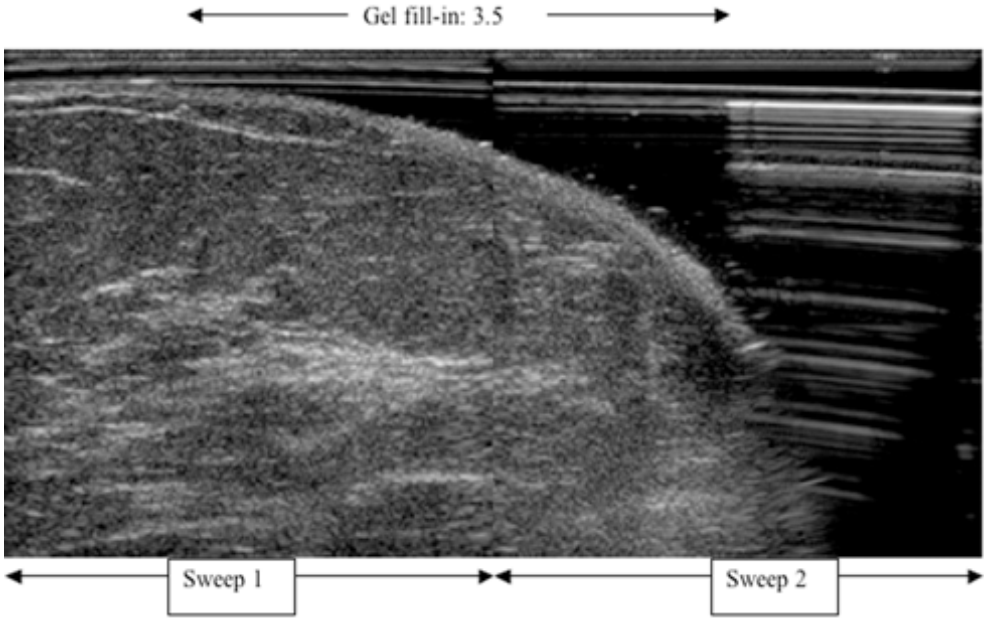

Figure 2.4: Single slice of a spliced grayscale image volume with gel fill-in around the breast border.

2.3.2 Couplant Selection

Our qualitative comparison indicated that the most suitable coupling agent between the breast and the compression paddle was the water-soluble hairspray, Got2BGlued. Another water-soluble hairspray, GigaHold, and a liquid adhesive that is used to attach ostomy and other appliances to skin, Skintac, also performed well. The latter, however, is not water-soluble and must be removed with alcohol.

When various viscous substances were qualitatively tested for coupling the transducer to the compression paddle in the lateral view, Sonotech Litho-Clear gel performed best overall. This was also the gel chosen for filling in the gap at the periphery of the breast.

Figure 2.5 compares the relative image quality obtained with the automated US scanning system using Got2Bglued hairspray and Litho-Clear ultrasound gel as the coupling media between the TPX paddle and the breast.

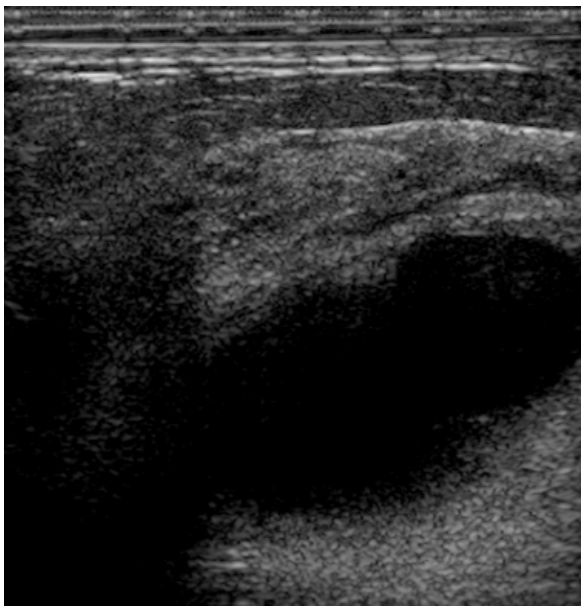

(a)

(b)

Figure 2.5: (a)A cyst in a patient's breast imaged through the compression paddle with Got2Bglued spray between the breast and the paddle. The patient had multiple cysts in both breasts. (b)The same cyst imaged through the compression paddle with US gel between the breast and the paddle.

Visual inspections of these patient images as well as quantitative measurement of a CNR improvement of 2.5% for the Got2Bglued couplant prove that the adhesive spray does not degrade image quality as compared to ultrasound gel. Also, it maintains correlation over time. See Fig. 2.6 for B-mode correlation over 5 minutes, which is the average time during which the patient is in compression.

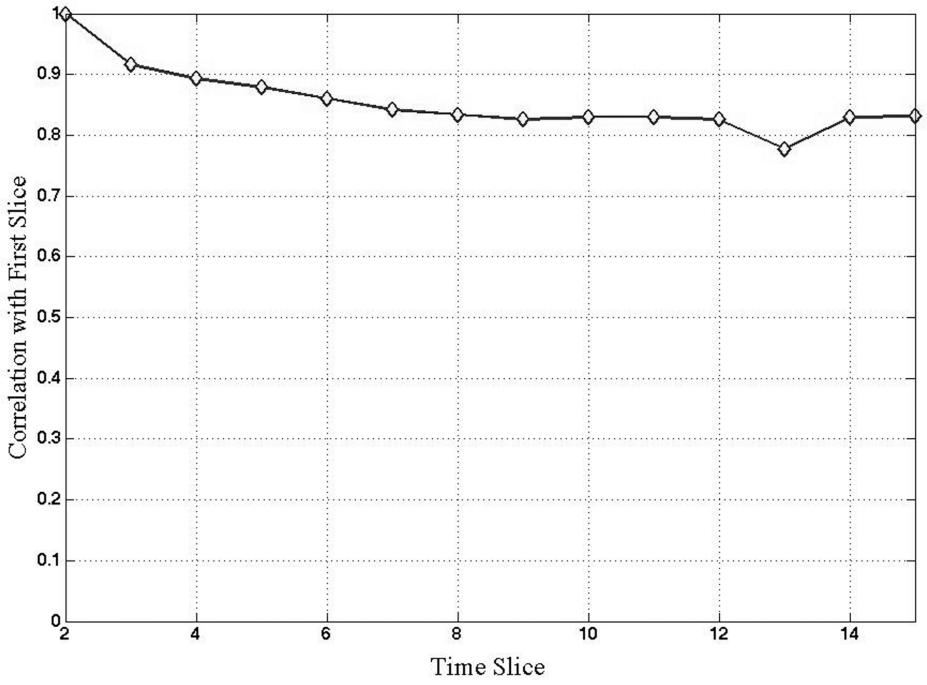

Figure 2.6: Correlation maintained over time for the most suitable coupling agent, for a stationary scan. The value largely stays above 0.8. The drop in correlation for frame 13 is likely to be due to patient motion.

Figures 2.7 and 2.8 graphically represent CNR values obtained for the anechoic and -9 dB (2.4 mm diameter, 4.52 mm^2 cross-sectional area) targets in the CIRS Gray Scale phantom. Circular ROIs of two different sizes [55 pixels (0.92 mm^2) and 130 pixels (2.16 mm^2)] were analyzed in several identical test images and the best results were selected in each case. The ROIs were positioned at the centers of the targets by eye. The smaller ROI provides information about image degradation in the middle of the targets due to the coupling agent, and is related to potential decreases in target conspicuity. The larger ROI provides more generalized

information about image degradation, in particular, fill-in due to the coupling agent. 'Water with TPX' is the gold standard case where a 2.5 mm thick piece of TPX (heretofore referred to as the 'TPX plate') was inserted between the transducer and the phantom and water was used as the coupling agent between the TPX plate and the phantom. 'Water without TPX' is the case where water was used between the transducer and the phantom, without an intervening TPX plate. This plate was a smaller version of the compression paddle that was more convenient to use when imaging the phantom. All of the other agents were tested with the TPX plate inserted. Aquasonic gel was used to couple the transducer to the paddle in all cases, and either water or the agents being tested were used to couple the paddle to the phantom. Of the three agents tested (Got2bglued, Gigahold and Skintac), Skintac had the best CNR value in six cases out of eight.

Figures 2.9 and 2.10 show background mean and RMS noise values obtained in the CIRS Gray Scale phantom at the 2.5 cm and 4 cm depths respectively, for both 55 and 130 pixel areas. In general, inserting the 2.5 mm thick TPX plate between the transducer and the phantom with water as the coupling agent resulted in a decrease in the average background pixel value bv 27.9% at a depth 2.5 cm and 32.5% at a depth of 4 cm. There were small (<10%) additional losses in the average background pixel values for the adhesives with TPX compared to water with TPX. The RMS background noise was less for Water with TPX compared with Water without TPX, probably due to the smaller average pixel values when TPX was present. Finally the RMS background noise for the adhesives with TPX was in most cases within about 10% of those for water with TPX.

2.3.3 Motion Analysis

Figures 2.11 and 2.12 graphically represent the results for B-mode analysis of motion artifacts. Mean and standard deviations for each artifact are included in Table 2.3.

In the graphs in Figures 2.11 and 2.12, the four bars represent the averages

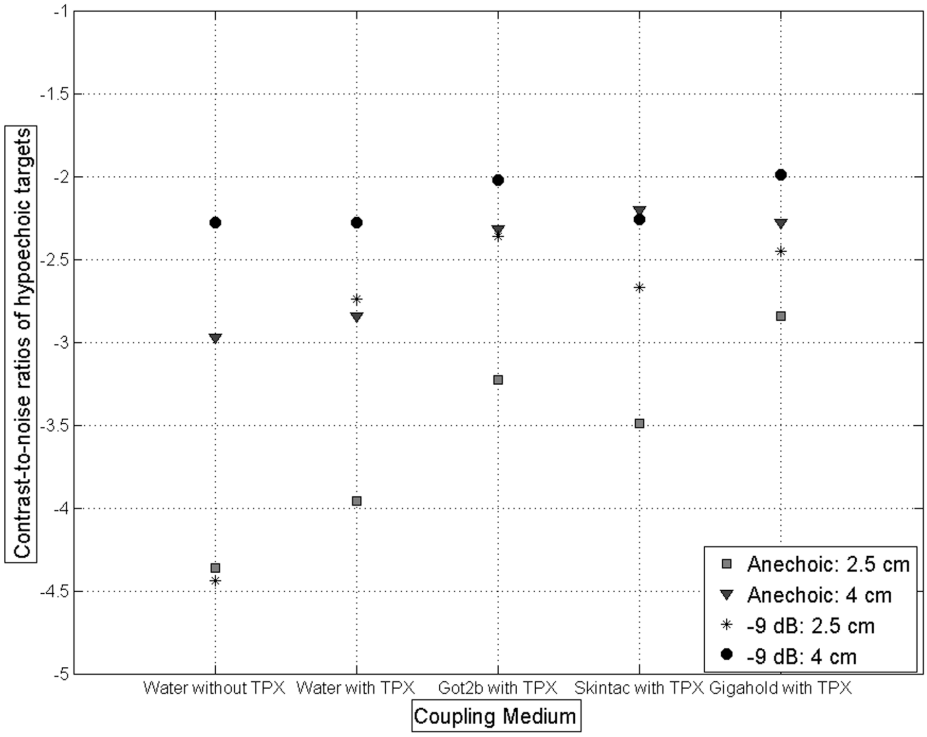

Figure 2.7: CNR values for both anechoic and -9dB targets at depths of 2.5 cm and 4 cm respectively, for each coupling medium, where ROI size is 55 square pixels. The largest (magnitude) value of -4.44 was obtained at 4 cm depth for the anechoic target, when water was used as the coupling medium, in the absence of a TPX plate.

Artifact	Left Breast		Right Breast	
	Mean	Standard Deviation	Mean	Standard Deviation
Breath Hold	0.963	0.056	0.979	0.023
Deep breath and release	0.805	0.128	0.807	0.098
Shallow Breathing	0.974	0.042	0.962	0.034
Talking	0.906	0.106	0.912	0.066

Table 2.3: Mean and standard deviation values for the four motion artifacts analyzed for the left and right breasts.

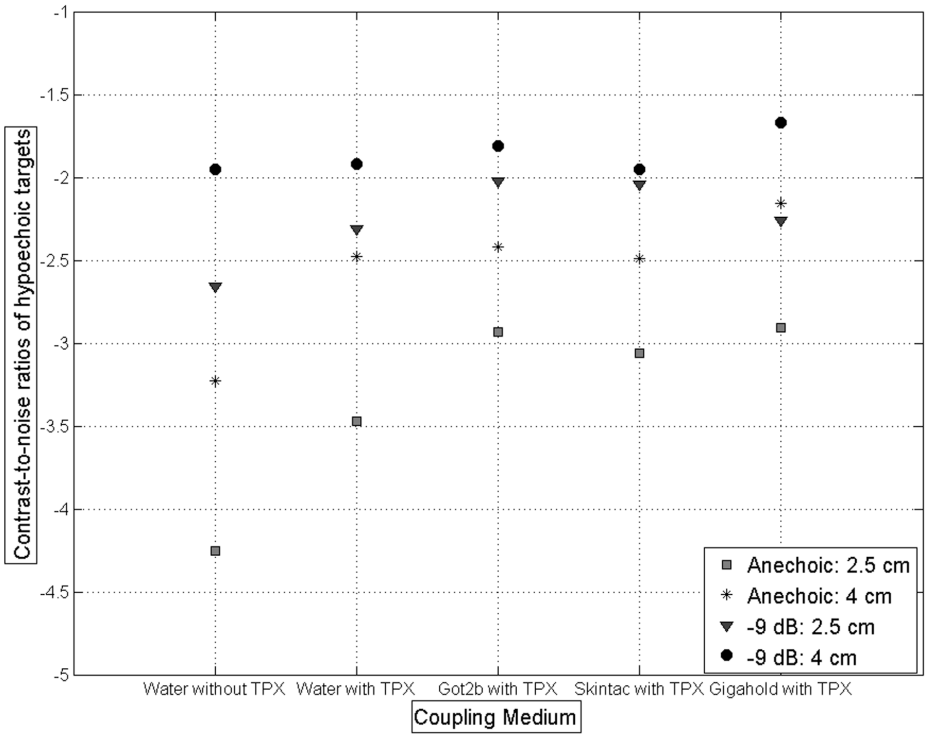

Figure 2.8: CNR values for both anechoic and -9dB targets at depths of 2.5 cm and 4 cm respectively, for each coupling medium, where ROI size is 130 square pixels. The largest (magnitude) value of -4.25 was obtained at 2.5 cm depth for the anechoic target, when water was used as the coupling medium, in the absence of a TPX plate.

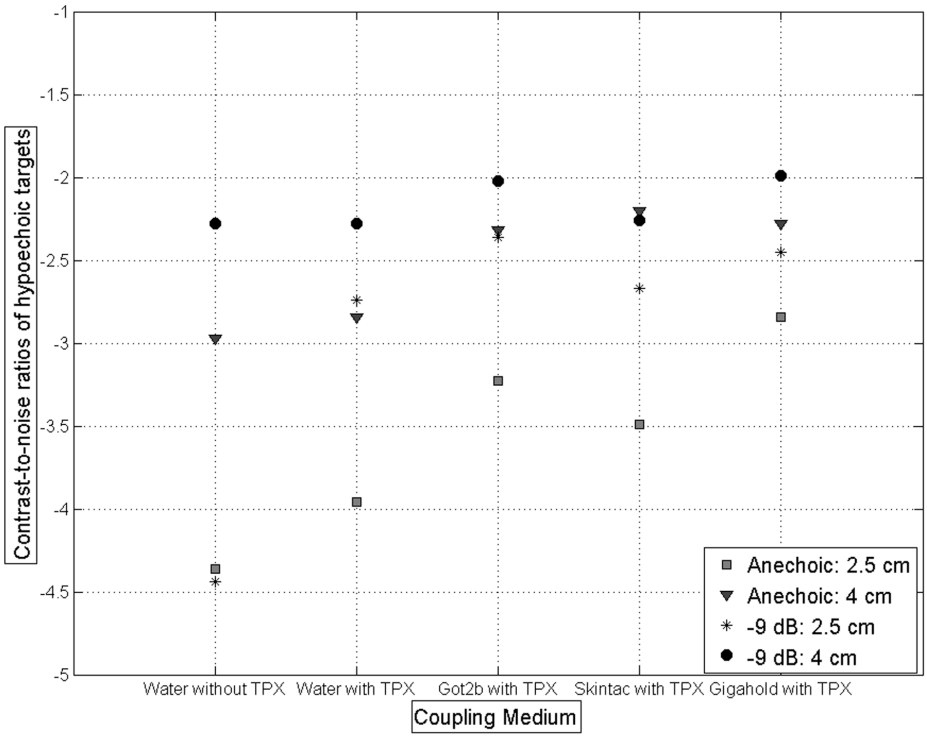

Figure 2.9: CNR values for both anechoic and -9dB targets at depths of 2.5 cm and 4 cm respectively, for each coupling medium, where ROI size is 55 square pixels. The largest (magnitude) value of -4.44 was obtained at 4 cm depth for the anechoic target, when water was used as the coupling medium, in the absence of a TPX plate.

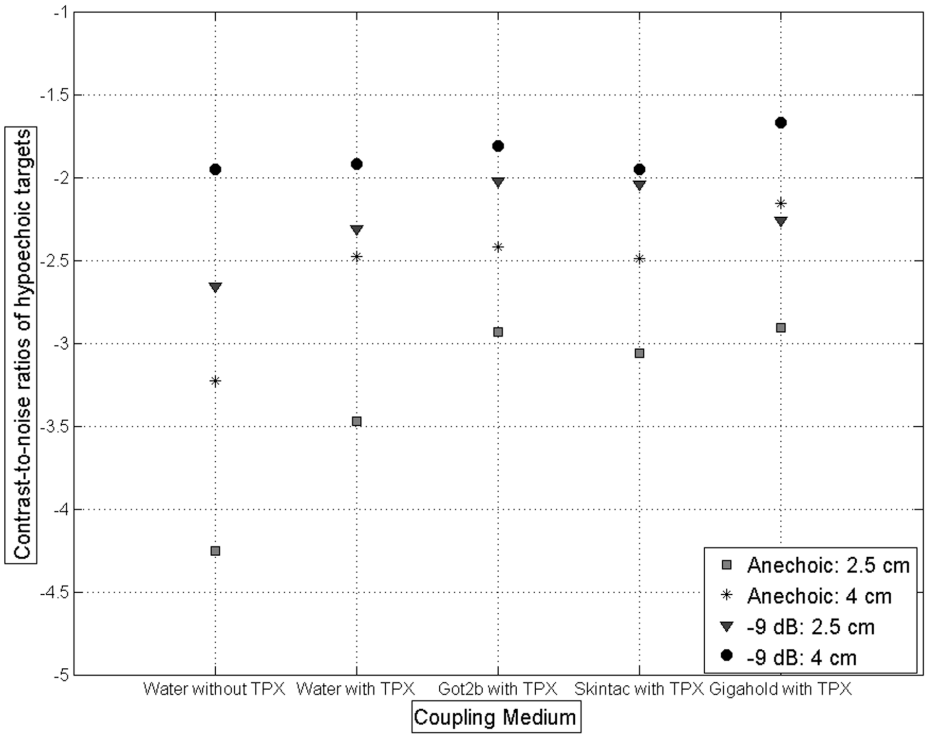

Figure 2.10: CNR values for both anechoic and -9dB targets at depths of 2.5 cm and 4 cm respectively, for each coupling medium, where ROI size is 130 square pixels. The largest (magnitude) value of -4.25 was obtained at 2.5 cm depth for the anechoic target, when water was used as the coupling medium, in the absence of a TPX plate.

of the minimum correlation values (minimum obtained in the 8 areas analyzed in each image) observed for each of the four experimental techniques. The error bars represent +/- one standard deviation.

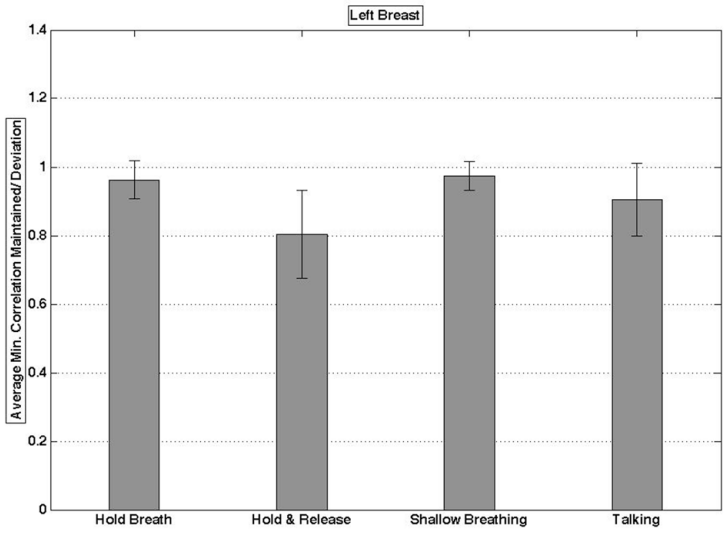

Figure 2.11: Averages and standard deviations of the minimum correlation values observed for the left breasts of six patients in the situations: breath hold, hold and release, shallow breathing and talking (repetition of single phrase).

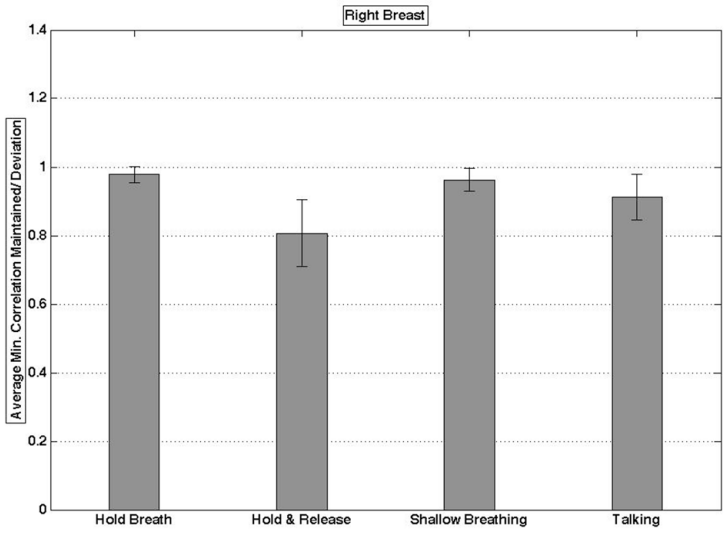

Figure 2.12: Averages and standard deviations of the minimum correlation values observed for the right breasts of six patients in the situations: breath hold, hold and release, shallow breathing and talking (repetition of single phrase).

In general (combining the data for both breasts) when minimum correlation was observed for B-mode data at the pixel level, breath hold (R = 0.97) and shallow breathing(R = 0.97) caused the least decorrelation, while speech caused intermediate decorrelation (R = 0.91) and deep breathing (R = 0.81) caused the most. Two sample Wilcoxon test results over every pair of different artifact correlation results for the left and right breasts individually, indicate that the four methods analyzed had statistically significant mean differences between them ($p << 0.05$). Wilcoxon tests comparing artifact correlations in patients' left breasts to those in patients right breasts did not indicate a statistically significant mean difference between the left and right breasts ($p >> 0.05$), except for breath hold.

These findings were similar to those obtained for elasticity imaging. When average correlation was observed for IQ data at the sub-pixel level, shallow breathing (R = 0.96) caused the least decorrelation, while breath hold (R = 0.93) also had a relatively high correlation value. Speech caused intermediate decorrelation (R = 0.87) and deep breathing (R = 0.73) caused the most. Two sample Wilcoxon test results indicated that shallow breathing, holding breath, and talking were statistically significantly different from deep breathing ($p << 0.05$), but not from each other ($p >> 0.05$). Correlation differences for the same artifact between the left and right breasts were not statistically significantly different ($p >> 0.05$). Registration of shifted sweeps in AVS [Krücker et al., 2000, Meyer et al., 1999, Moskalik et al., 1995] in order to splice them to form the complete 3-D volume resulted in a negligible overlap error of 0.55 - 0.65 mm. Fig. 2.13 is an example of a recently spliced image volume, where two sweeps were trimmed and fused to complete the volume.

2.3.4 Estimation of Coverage

The gaps between the breast and the compression paddle at the breast periphery can limit ultrasound coverage to only half of the total breast area for the combined x-ray/ ultrasound imaging system. Filling the gaps with Litho-Clear ultrasound gel

(a)

(b)

Figure 2.13: (a)Single slice of a spliced grayscale image volume for a recent patient with multiple cysts in the left breast. (b) Same image slice; the vertical line indicates the joint between the adjacent scans.

using a syringe is effective at solving this problem, reducing the gap lengths by about 60%. This solution is only partial as 73% of malignant lesions are present at the periphery of the breast, as defined by a zone 1 cm wide beneath the subcutaneous fat or anterior to the retromammary fat [Stacey-Clear et al., 1993]. However, it is possible to image the axillary tail and extreme medial regions of the breast better by using lateral views. The subareolar region can be imaged better by compressing the breast such that the nipple is closer to the TPX paddle, therefore reducing the gap between the paddle and the subareolar region.

2.3.5 Couplant Selection

9 different materials were tested for acoustic coupling of the compression paddle to the breast. Their coupling strengths, effects on image CNR and practicability were compared and the optimal substance was chosen. In all cases, water without the TPX layer produced the best CNR values. Water with the TPX layer showed better CNR values than the other agents in all cases except one. The insertion of the TPX plate was found to reduce the CNR value on the average by 11.3% at a depth of 2.5 cm and by 15.8% at a depth of 4 cm for gray scale images. It also reduced the average pixel value in the background region by 30.2% with almost no change in the standard deviation. In six out of eight cases, the Skintac adhesive produced better CNR values than the other two agents. Background mean and standard deviation values show that Skintac has consistently low standard deviation values while maintaining high background mean levels. However, the difference in CNR values between Got2Bglued and Skintac was found to be relatively small (less than 10% in all cases except one). Furthermore, in terms of practicality, Skintac is not as viable as the next best agent, Got2bglued; Skintac requires rigorous alcohol clean-up, while Got2bglued can be removed easily with soap and water.

Therefore, we decided that the Got2bglued adhesive hairspray was best for our application. In all cases, CNR values for Got2bglued were degraded by no more

than 20% as compared to pure water. Got2bglued preserves image quality, was empirically found to be a close second-best for adhesively coupling the breast to the paddle and was easy to remove and clean up.

10 pure and 4 compound substances were tested for coupling the transducer to the paddle in the LM view. Litho Clear ultrasound gel maintains high viscosity at body temperature (37 ℃) and proved most effective for coupling the transducer to the paddle for LM views. It is also used to increase area of coverage by filling in the gap between the paddle and the outer edge of the breast. As of September 2006, 73 subjects have been imaged in CC and LM views of the affected breast using the experimentally superior coupling agents.

2.3.6 Motion Analysis

Patient motion artifact analysis carried out in both B-mode and IQ mode proved that shallow patient breathing and breath-hold were not harmful to image quality, whereas speech and sudden breathing produced unacceptable artifacts. The significant difference that was observed in the B-mode breath hold data for the left and right breasts may be caused by cardiac asymmetry i.e., when the patient holds her breath, the heart pulses more strongly due to the baroreceptor reflex [Seidel et al., 1997]. Hence breath hold causes more decorrelation for the left breast. Such a difference between the images of the right and left breasts was not observed with shallow breathing.

The region wise split for all motion conditions indicated that decorrelation was consistently (95% of the time) greatest towards the chest wall. This was expected because the motion of the chest wall causes decorrelation when the patient is breathing or talking. Overall, since patient scans can be more than a minute long, shallow breathing is a more feasible option than breath hold.

By aiding the stabilization of the compressed breast, we succeeded in minimizing technical difficulties in image splicing and registration caused by slippage of the

breast.

2.4 Conclusion

In conclusion, limitations of automated US scanning on a multi-modality breast imaging system have been addressed by developing methods to couple the transducer and breast to the compression paddle, as well as methods to fill-in peripheral gaps, minimize patient motion and register and reconstruct multi-sweep US image volumes after clinical acquisition. The ultrasound techniques described and evaluated here yield ultrasound volumes that provide good comparisons with x-ray attenuation properties of the tissues as viewed in the high speed, wide angle, and low dose x-ray tomosynthesis images. This direct comparison should improve visual and computer-assisted diagnosis.

CHAPTER III

Image Registration for Detection and Quantification of Change on Digital Tomosynthesis Mammographic Volumes

3.1 Introduction

Digital tomosynthesis mammography is a promising modality for routine breast cancer screening and diagnosis. Three-dimensional digital tomosynthesis mammography[Claus et al., 2006, Eberhard et al., 2006] yields images of considerably better quality than does projection mammography [Burgess et al., 2001, Hadjiiski et al., 2004], because anatomical features are displayed in greater detail [Zhang et al., 2006]. On mammograms, these features are often obfuscated by overlying tissue. Tomosynthesis yields substantial three-dimensional information that makes registration, subtraction, and detection of change a more realistic possibility. Precise spatial alignment of these image volumes would aid more rapid detection of changes in tumor appearance and growth over time, especially during neoadjuvant chemotherapy. However, the presence of artifacts caused by the highly asymmetric point spread function of digital tomosynthesis mammography suggests that spatial alignment of the two image sets might be difficult if there are large differences in the volumetric displacements of internal structures during compression. Our purpose was to achieve digital breast tomosynthesis image registration of whole breast image volumes acquired at different

times in the same mammographic position and to assess the magnitude of residual error.

3.2 Subjects and Methods

A system combining automated whole breast ultrasound and digital tomosynthesis mammography [Kapur et al., 2004] is under investigation for the detection and characterization of breast masses. With this system, 21 tomosynthesis projection images can be acquired over a 600 arc in 7.5 seconds. Each 3D tomosynthesis image volume is reconstructed from 21 projection images using simultaneous algebraic reconstruction. To study whether registration was feasible, two such image volumes were acquired in each of our seven cases. Four of these cases consisted of images acquired within minutes of one another after the patients breast was removed from the imaging unit, cleaned, repositioned and recompressed between the paddle and detector. In two of the other three cases, the image volume sets were acquired over a one-year period. In the third case, the acquisition interval was 6 months. All patients had clinical mammographic findings classified as negative (BI-RADS category 1) or benign (BI-RADS category 2). Institutional review board approval was obtained for this study and informed consent was obtained from every patient.

Special care was taken in stabilizing the breast during each examination. The breast was compressed between mammography-style plates and acoustic coupling was used for reproducible, large area scanning through the plates [Sinha et al., 2007a] Registration was performed with mutual information for automatic multimodality image fusion (MIAMI Fuse , University of Michigan) non-rigid 3D registration [Kim et al., 1997, Meyer et al., 1997, Meyer et al., 1999] on the AVS platform (Advanced Visual Systems, Waltham, MA), based on the mutual information objective function (see Equation 1) and thin plate spline interpolation [Bookstein, 1997] .

$$I = \sum^{a} \sum^{b} p(a,b) log_2(p(a,b)/p(a)p(b)) \tag{3.1}$$

'a' and 'b' are the two datasets to be registered in the equation above.

One image set was selected as the reference (usually the first of the two acquired image volumes; either can be selected). The other image set (called the target or homologous image) was spatially transformed to align with the reference frame. We registered the two 3D image sets by selecting 15 corresponding control points placed at key features, e.g. forks or sharp bends in blood vessels, ligaments and ducts. These points were employed as control points by the software and were moved to optimize the so-called mutual information (MI) of the two image volumes (see Figure 3.1).

We estimated registration error by finding a different set of fifteen fiducial points in both image sets and measuring the Euclidean distance between the locations of each point on the reference and registered images. Three expert readers independently marked these points twice each, to provide a total of six measurements per case. The measurements were averaged to produce the final estimate of fiducial registration error.

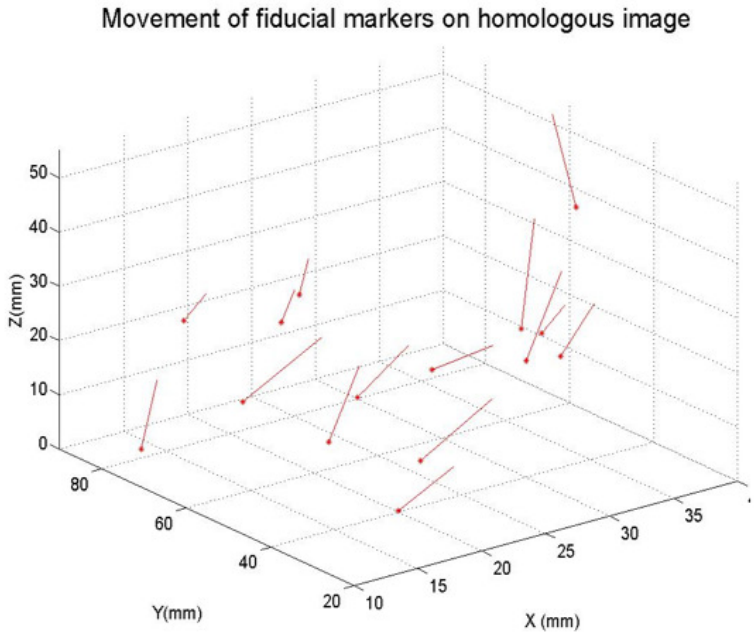

Figure 3.1: Movement of fiducial markers over the course of non-linear registration of tomosynthesis image sets.

3.3 Results and Discussion

The mean registration error was 1.8 mm +/- 1.4 mm. The minimum mean error of 1.2 mm was achieved for a dense breast over scans taken within the hour (see Figure 3.2).

One pair of image volumes acquired over a year-long interval was not be registered satisfactorily. This image set was registered only after down-sampling by a factor of 8, which greatly increased the residual error value. The registration error was only 1.6 mm, however, for an image volume pair on the contralateral breast of the same volunteer over a year-long interval (see Figure 3.3). The maximum mean error of 2.8 mm was observed for a pair of scans obtained with a 6-month gap. Of the four pairs acquired before and after repositioning, without a significant time lapse between the two acquisitions, registration was successful with an average registration error of 1.6 mm +/- 1.2 mm. Table 3.1 shows the errors in every case. Vector plots (not shown) of the displacements of the 15 or so control points throughout the image volumes showed in every case that the registration corrected both local tissue warping and global translation.

We found for the first time to our knowledge that whole breast digital tomosynthesis mammography image volumes taken at different times can be spatially registered. The registration process was complicated by several factors; primarily, the compression of the breast at different times results in different mammographic appearances. Variable breast distortion during compression and actual physiologic changes (in case of a large time interval between scans) offer challenges. In some cases there can be high shear gradients at boundaries between tissues of differing composition. Digital tomosynthesis mammographic volumes also contain reconstruction artifacts that are dependent on the viewing angle. Furthermore, these digital tomosynthesis mammographic images have a slice thickness of 1 mm (this value can vary from 0.1 mm to half the lateral extent of

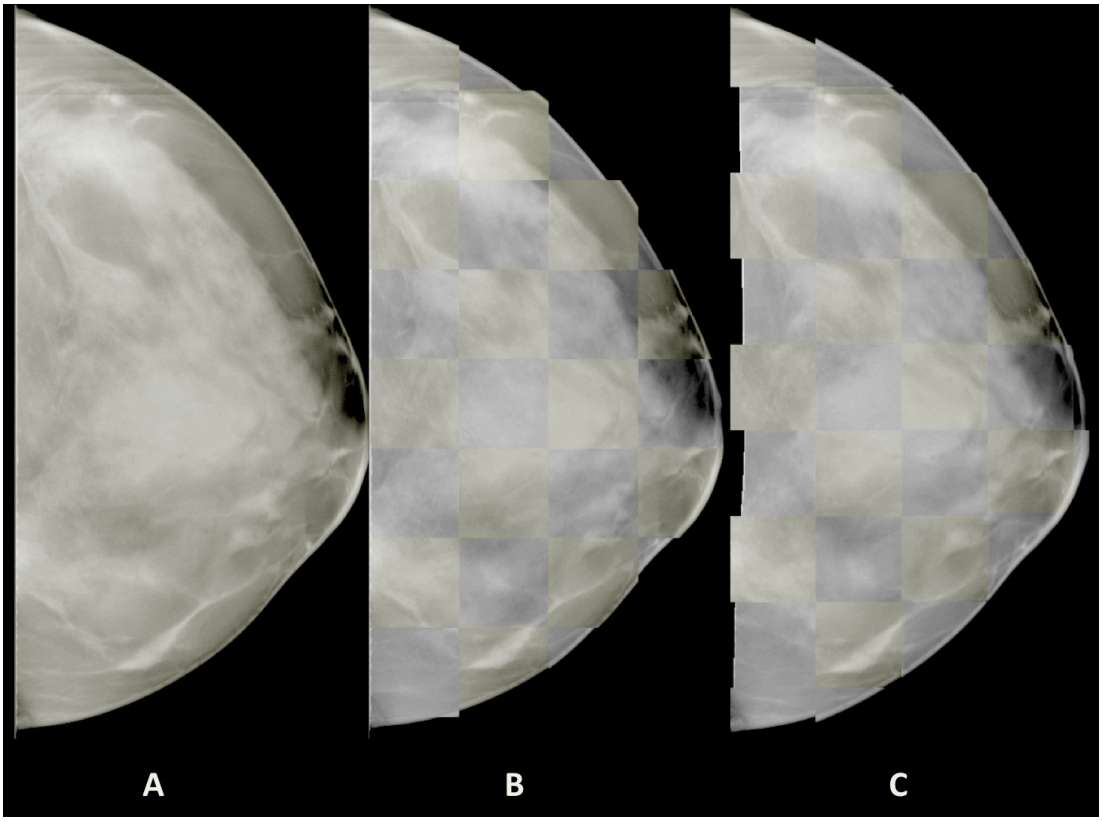

Figure 3.2: 49-year-old woman with simple cyst in breast (case A1, Table 1). Tomographic images from image volumes that were acquired minutes apart and registered with mutual information for automatic multimodality image fusion. A, Reference image. B, Checkerboard display with alternating squares from reference image and target image before registration. C, Checkerboard display with alternating squares from reference image and target image after registration showing better alignment of breast features than in B, especially in top half of image.

Case	Time interval	MRE (mm)	SD (mm)
A1	Less than 15 min	1.2	0.97
A2	Less than15 min	1.39	1.27
A3	Less than15 min	1.8	1.2
A4	Less than15 min	1.85	1.37
B1: LCC	12 mth	1.55	1.24
B2	6 mth	2.76	2.3
B1: RCC*	12 mth	-	-

Table 3.1: Registration Evaluation of Seven pairs of Breast Tomosynthesis Images. Mean registration error (MRE) and standard deviation (SD) values for seven pairs of breast tomosynthesis images. *B1: RCC was an unsuccessful registration because registration did not succeed until the images were downsampled by an unacceptably large factor (8).

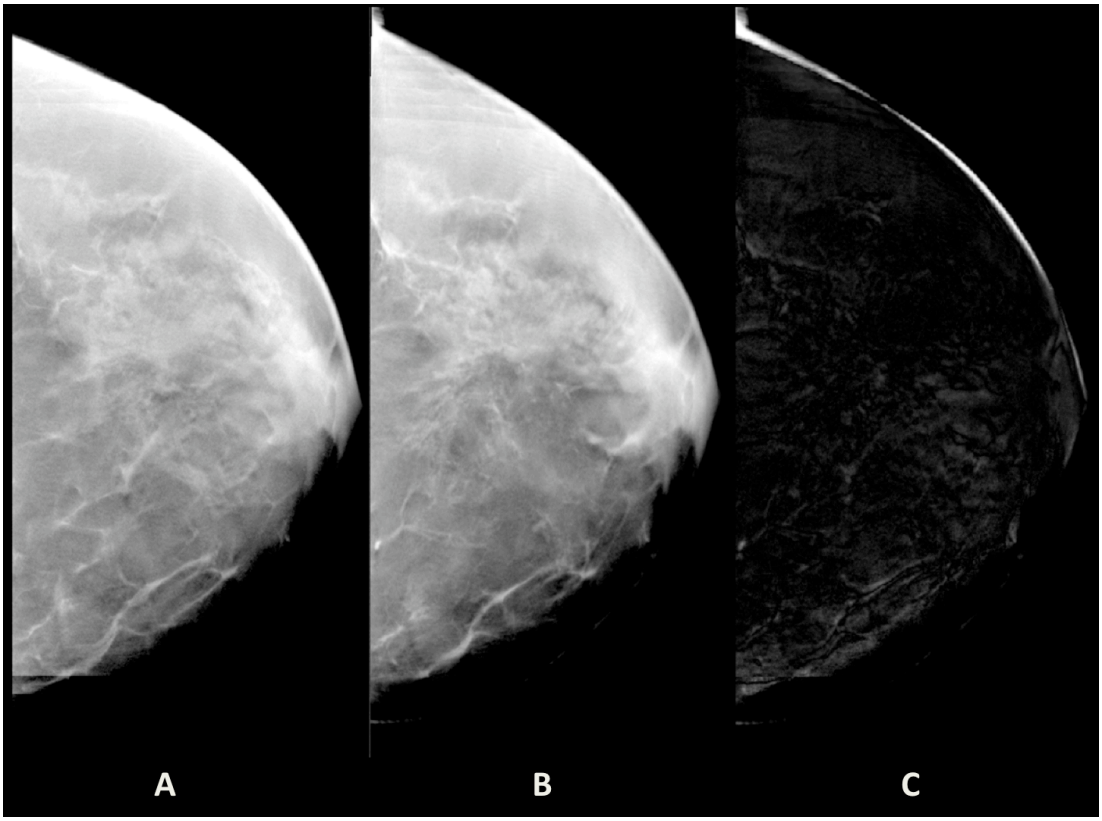

Figure 3.3: 50-year-old woman with normal breast (case B1, left craniocaudal, Table 1). Tomographic images from image volumes that were acquired 1 year apart and registered with mutual information for automatic multimodality image fusion. A, Reference image. B, Registered image from the most recently acquired image volume. C, Difference image shows changes in breast over 1 year, and registration error.

the image), depending on the extent of target object in the direction of x-ray tube motion. The axial resolution is clearly poorer than the 0.1 mm x 0.1 mm resolution in the image plane (voxel size was 0.1 x 0.1 x1 mm^3).

With care in selecting nearly identical locations in each of two same-modality image volumes of the breast, image based registration was quite successful. The exact manual identification of starter points is not always necessary, but we deemed it necessary for this limited study. It may be possible to develop feature recognition for automated selection of corresponding starter points.

Six out of seven tomosynthesis pairs acquired to date were registered with a residual error of l-3 mm. Sickles et al [Sickles et al., 2005] found that the mean and median sizes of cancers detected by mammography in a representative sample population of 332,926 patients were 20.2 and 15 mm respectively. Although an average registration error of 2 mm is relatively large compared to the tomosynthesis resolution of 0.1 mm, this error is small compared with the average size of mammographically detected breast cancers in a screening population. A tolerance of +/- 10% in tumor diameter change estimation in this first attempt at tomosynthesis registration is promising.

The subtraction technique shown in Fig. 2 may prove useful for highlighting change that is not due to registration error. Excepting changes in parenchymal volume and water content over the course of the menstrual cycle [Fowler et al., 1990], certain changes in the appearance of breast tissue over time can indicate the presence of malignancy, and comparison of the reference image and the registered image could help to identify such changes. Any improvement in the spatial registration of two 3D image volumes should aid in finding and comparing changes in breast tissue. When achieved, image registration should be relevant in interpretation of digital tomosynthesis mammographic volumes, particularly for less experienced readers and in computer-aided diagnosis.

3.4 Conclusion

In conclusion, limitations of automated US scanning on a multi-modality breast imaging system have been addressed by developing methods to couple the transducer and breast to the compression paddle, as well as methods to fill-in peripheral gaps, minimize patient motion and register and reconstruct multi-sweep US image volumes after clinical acquisition. The ultrasound techniques described and evaluated here yield ultrasound volumes that provide good comparisons with x-ray attenuation properties of the tissues as viewed in the high speed, wide angle, and low dose x-ray tomosynthesis images. This direct comparison should improve visual and computer assisted diagnosis.

CHAPTER IV

Multi-modality 3D imaging for breast cancer screening X-Ray tomosynthesis and automated ultrasound

4.1 Introduction

Traditionally, X-ray mammography is the gold standard [Stacey-Clear et al., 1993] for breast cancer screening and B-mode ultrasound is used to aid in characterization of the suspicious mass [Stavros et al., 1995]. In this study, 3D digital X-ray tomosynthesis [Claus et al., 2006, Eberhard et al., 2006] (DT) and 3D automated ultrasound [Carson et al., 2004, LeCarpentier et al., 1999] images of every patient's breast were acquired in the same geometry with a unique dual-modality system [Kapur et al., 2004] (see Figure 4.1). X-ray tomosynthesis shows great promise [Chan et al., 2005] for use as a primary screening tool in breast imaging and its efficacy in detection and assessment is enhanced by geographic correlation with an automated ultrasound scan acquired in the same geometry. The automated grayscale ultrasound is acquired though a special compression paddle[Booi et al., 2007] that is also used for X-ray imaging.

X-ray and ultrasound images can be acquired with the dual-modality system in the conventional mammography views: cranio-caudal (CC), medial-lateral-oblique (MLO), lateral-medial-oblique (LMO), lateral-to-medial (LM), and medial-to-lateral (ML). The ultrasound transducer is placed in a holder that is attached to an x-y

Figure 4.1: Patient seated at the dual modality system, being imaged with X-ray and ultrasound methods. The patient's breast is compressed between a TPX (4-methylpentene-1 based polyolefin) paddle and the X-ray detector. The X-Ray tube is contained within the cowling on top, while the ultrasound transducer is attached to a motorized carriage directly above the compression paddle. The GE L9 ultrasound unit is on the right.

translator system, which maneuvers the transducer across the compression paddle under software control. One to three adjacent automated US transducer sweeps are performed, depending on the shape and size of the patient's breast. The US image volumes obtained are registered and fused to visualize the entire breast volume.

For meaningful image fusion in the context of mass detection and characterization, the lesion(s) of interest must be visible in both modalities. When this is the case, geographic correlation afforded by the dual modality system localizes the mass within the breast with more accuracy. Ultrasound images aid the radiologist in assessing the malignancy of a suspicious mass seen on the X-ray image, especially in

identifying benign masses (e.g., cysts) to prevent unnecessary biopsies. It is therefore essential that the quality of the automated ultrasound images not be significantly degraded from those obtained with traditional direct contact and hand-guidance. The challenges of automated US scanning with this system have been addressed [Sinha et al., 2007a] by developing methods to fill-in peripheral gaps, minimize patient motion and register and reconstruct multi-sweep US image volumes. These refinements in technique facilitated this study.

4.2 Methods

IRB approval was obtained for this study and informed consent was obtained for every patient in these trials. Testing was performed on a combined system consisting of a GE LOGIQ 9 ultrasound (US) system and a second generation prototype GE digital tomosynthesis (DT) unit. The US transducer employed in this study was a GE M12L linear matrix array operating at center frequencies of 10 and12 MHz. The US system was augmented with a motorized transducer carriage that translated the transducer across a TPX (4-methylpentene-1 based polyolefin) plastic compression paddle of 2.5 mm thickness. Water was employed as the coupling medium between the transducer and the paddle for CC-views and gel was used for all other views.

To best splice adjacent US sweep images into a 3-D volume, it is preferable to include redundancy in the form of a programmable overlap between adjacent sweeps. In practice, the actual overlap often changed slightly due to possible bowing of the compression paddle, flexion in the transducer holder, etc. Using approximately known overlap values (often verified by eye), complete automated US image volumes were generated for each case.

Twenty-seven patients were imaged on this combined system, 7 cyst cases and 20 with BIRADS 4 lesions. DT image volumes and automated US image volumes were acquired in the same view and in the same geometry. 3 experienced, MQSA certified

radiologists independently reviewed the resulting images in a blinded study. The tomosynthesis and automated US images were assessed separately at first, viewed with ImageJ, a public domain Java image processing application supported by NIH Image [NIH, 2010].

To begin with, research tomosynthesis was compared to clinical mammography. The total numbers of detected masses with BIRADS ratings between 3 and 5 were noted for both techniques. Then, the percentage visible margins were compared for corresponding masses seen in both types of images. Finally, readers were asked to rate their preference for one modality over the other, with 1 being 'Mammogram much better', 3 being 'Equivalent' and 5 being 'Tomosynthesis much better'. A similar comparison was made between research automated ultrasound and clinical direct contact, hand-guided ultrasound. The readers were asked to specify whether the primary mass was a simple cyst ('Yes/No') and then state percentage probability of malignancy for this mass. Finally, readers were asked to rate relative mass visibility, with 1 being 'Clinical hand US much better', 3 being 'Equivalent' and 5 being 'Automated research US much better'.

Lastly, the DT and automated US images were correlated with in-house software and viewed together. Each radiologist gauged the usefulness of multi-planar imaging and correlation between DT and auto US on a scale of 1 to 5, where a rating of 1 was equivalent to 'not useful' and a rating of 5 was equivalent to 'extremely useful'. A second study was conducted on a subset of 10 cases by 2 of the first 3 readers, using more advanced correlation software (see Figure 4.2). The radiologist was able to draw a 3D box around the suspicious mass in one image and the software automatically generated a geographically correlated, similarly boxed region on the other image, within which he or she could confidently localize and further characterize the mass. The reader's confidence level in localizing and identifying the primary mass in both imaging modalities was measured on a scale of 1(low) to

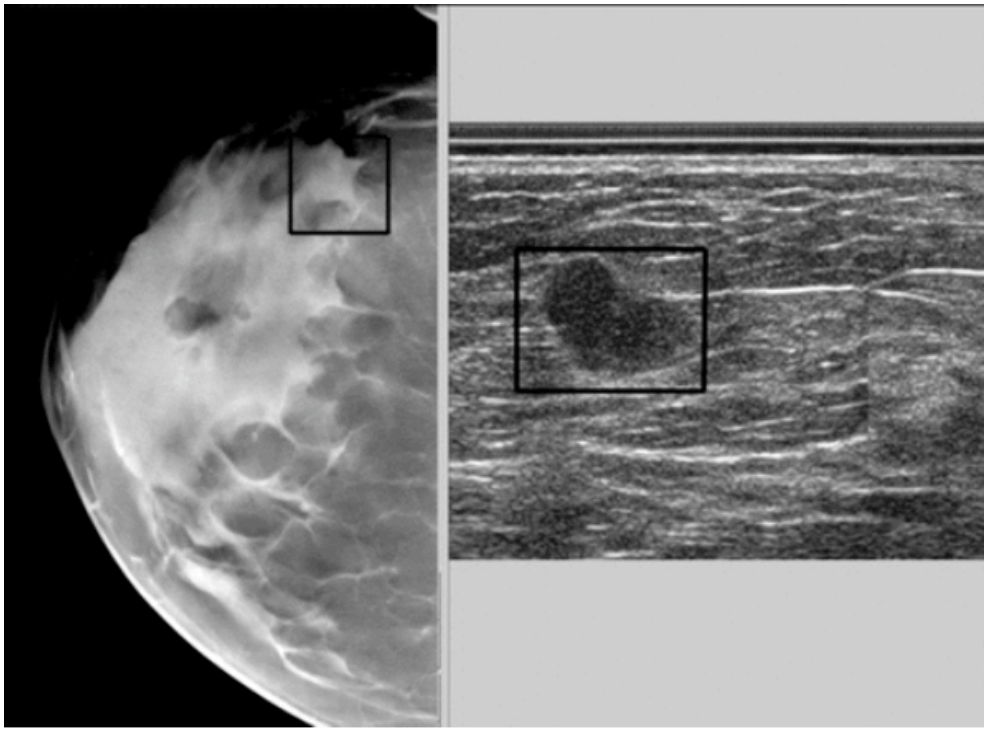

Figure 4.2: For this cancer case, a box was drawn around the lesion by the radiologist on the tomosynthesis image (in red), and transferred (in white) to the orthogonal automated ultrasound image on the right. Ultrasound image is at 2X magnification.

5(high), before and after geographic co-location/correlation.

4.3 Results and Discussion

The mean preference for digital tomosynthesis over mammography was 4.01 (DT much better) on a scale of 1 to 5. Tomosynthesis outperformed mammography in mass detection (BIRADS 3 to 5), mass margin delineation and cancer detection. (Results have been presented and will be published elsewhere.)

The quality of research automated ultrasound was consistently judged to be inferior to clinical hand ultrasound, as the readers expressed a mean preference of 1.67 (clinical hand much better) on a scale of 1 to 5. Out of 78 possible detections for 26 cases (one case out of the 27 had only micro-calcifications and no mass), 16 detections could not be made on automated ultrasound because of current difficulties in reaching lesions against the chest wall. However, when detections could be made

on auto US, mean correlation between the radiologists' assessments of percentage malignancy on the clinical hand US and the research auto US was 0.81. Hence, in spite of its limitations, automated US performed well enough to justify geographic co-location with DT.

In the first study of 26 cases (see Figure 4.3), the mean ranking for usefulness of correlative imaging was 2.75, whereas the median ranking was 3(moderately useful) on the scale of 1 to 5. At least one reader rated usefulness as 4 or 5 in 16 cases out of 26 (62%).

In the additional study of 10 cases, with more advanced software, the mean rating for usefulness of correlation increased to 3.25. At least one reader rated usefulness as 4 or 5 in 6 cases out of 9 (67%). (One case had indeterminate readings). Confidence in localizing and identifying the suspicious mass increased in 7 cases out of 9 (see Figure 4.4). However, a Wilcoxon signed rank test did not indicate a statistically significant change in confidence levels (p value was 0.072 and 0.053 for the two readers respectively).

On the whole, when lesions were visible in automated US, they were characterized with an accuracy comparable to that achieved with clinical hand US. Progress needs to be made in producing ultrasound scans with greater breast coverage, especially at the chest wall and the breast periphery. Automated US in its current setup cannot replace clinical hand US for screening purposes but can aid the radiologists in lesion detection and assessment.

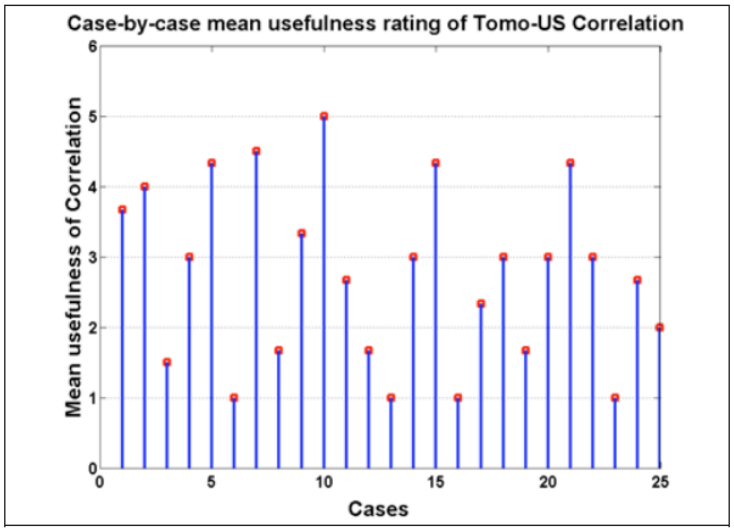

(a)

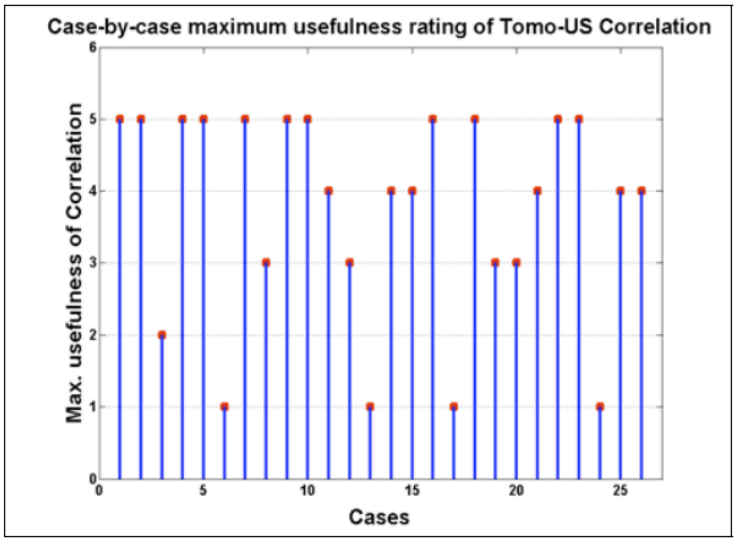

(b)

Figure 4.3: Mean(a) and maximum(b) DT-US correlation utility ratings for 26 cases. A scale of 1 to 5 was used, where a rating of 1 was equivalent to 'not useful' and a rating of 5 was equivalent to 'extremely useful'.

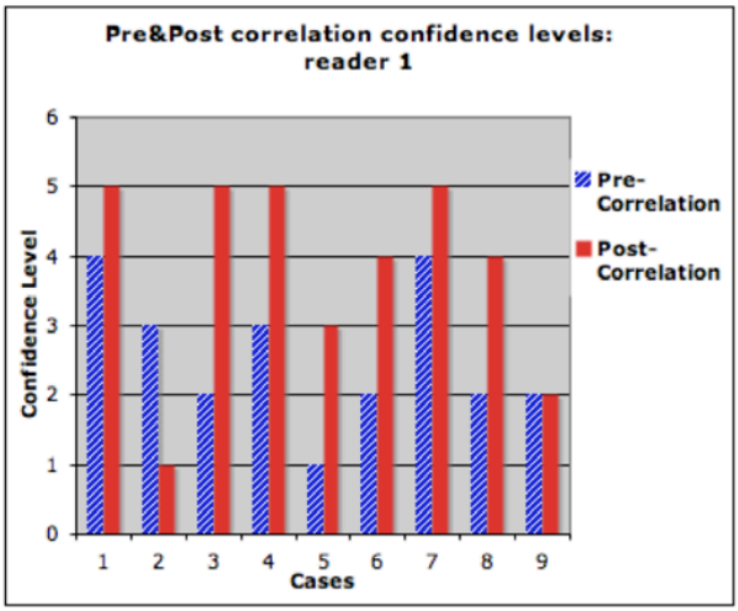

(a)

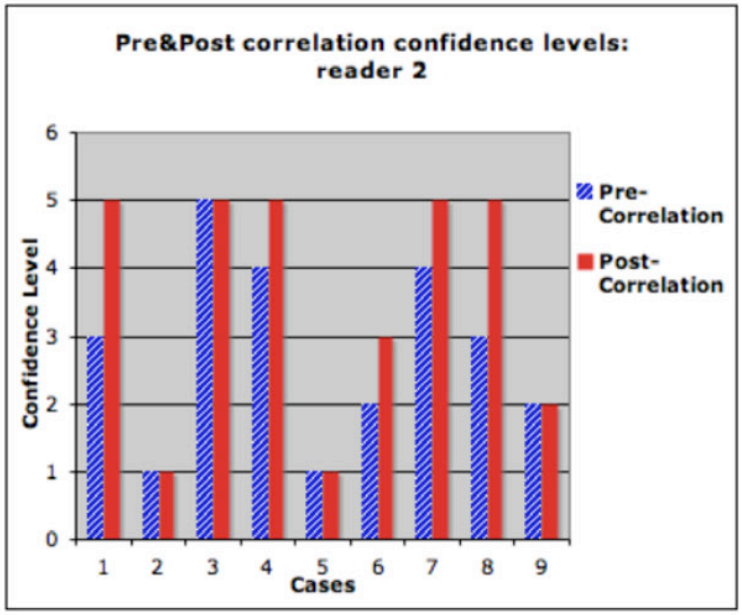

(b)

Figure 4.4: Confidence in localizing and identifying the primary mass in both image modalities, pre and post visual geographic correlation, as expressed by readers 1(a) and 2(b). A scale of 1(low) to 5(high) was used.

4.4 Conclusion

Automated ultrasound aids the radiologists evaluation of a suspicious mass in the human breast and raises the confidence level of his or her assessment. As automated scanning and reading software techniques advance, superior results are expected.

CHAPTER V

Image Processing for Registration and Fusion of Opposed View Breast Ultrasound Image Volumes

5.1 Introduction

Automated 3D ultrasound imaging presents good potential for breast cancer screening purposes, as recently asserted by Kelly et al. [Kelly et al., 2010], especially for women with dense breasts for whom mammography is less effective because the X-Ray attenuation of dense normal tissue is similar to the attenuation of the high water content and connective tissues of cancers.

With ultrasound, there is a trade-off between imaging depth and resolution due to the fact that higher frequencies, which provide finer resolution, are attenuated disproportionately. To retain the resolution of high frequency ultrasound, while maintaining registration with x-ray images, we can image the breast from both sides in the mammographic geometry (i.e., breast compressed between two plates), which we call dual-sided imaging (see Figure 5.1). This is a viable technique for better quality images formed by registering and fusing opposite views since less depth penetration is needed. Improved resolution at higher frequencies facilitates detection of micro-calcifications and estimation of tumor margins, features highly suggestive of breast cancer.

Success in registration of dual-sided images is complicated by low signal-to-noise ratio (SNR) and other artifacts in the central region of the breast where the two

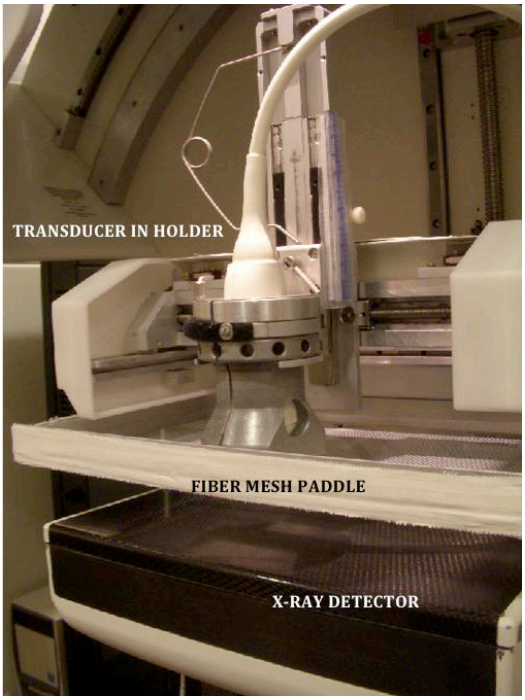

(a)

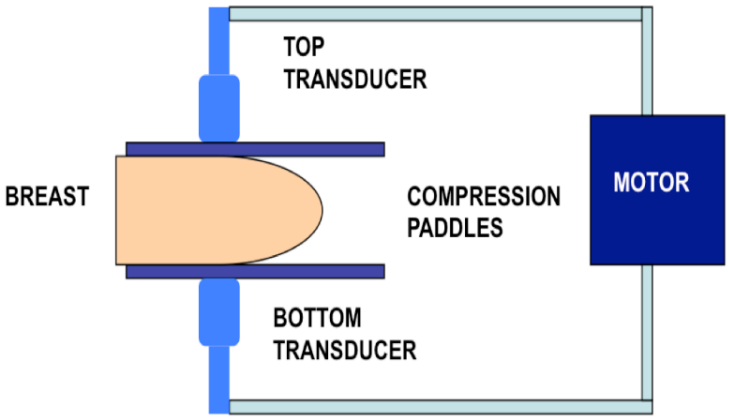

(b)

Figure 5.1: (a) Automated ultrasound acquisition set-up for single-sided imaging. The software-driven motorized transducer carriage moves over a compression paddle. (b)Schematic of setup for automated dual sided imaging of the breast in mammographic compression.

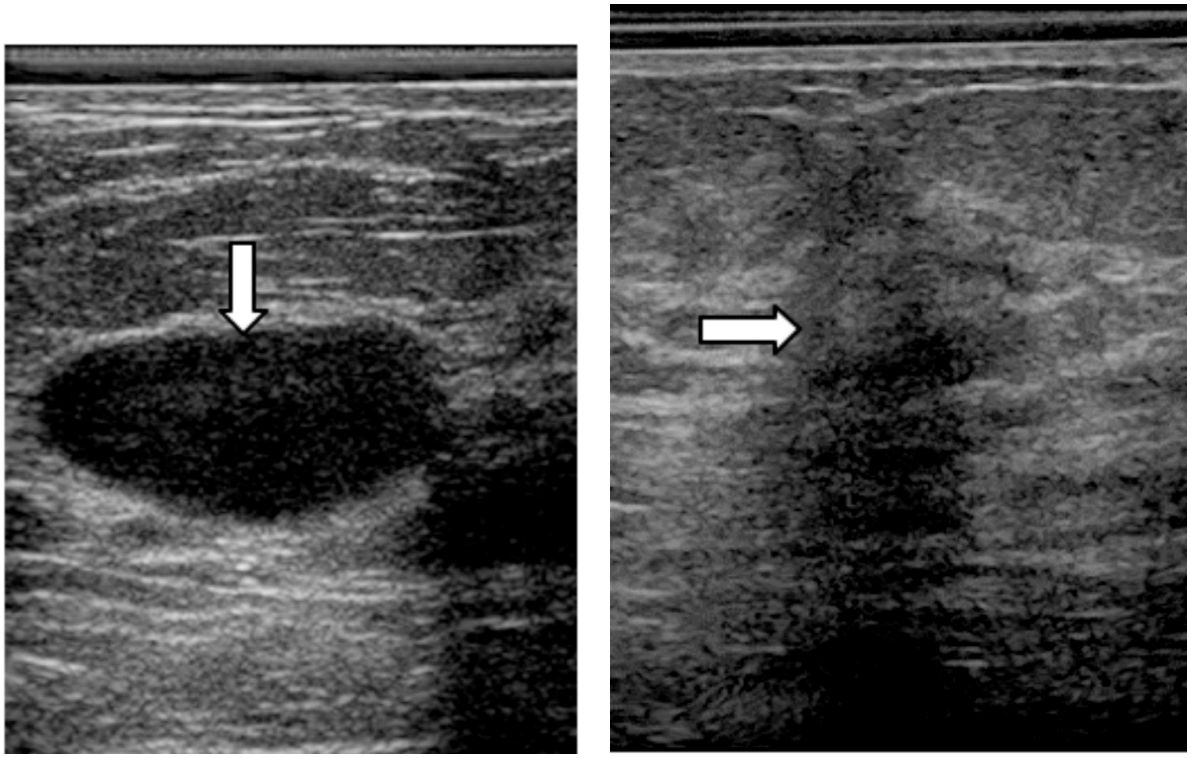

(a) (b)

Figure 5.2: (a)Example of cyst in a breast image (indicated by arrow), with enhancement underneath. (b)Example of cancer in a breast image (indicated by arrow) with shadow underneath.

views overlap [Bude and Tuthill, 2000, Krücker et al., 2000]. Posterior acoustic 'shadows' and 'enhancements' are specific artifacts that are prevalent in breast ultrasound images (see Figure 5.2). They are caused by the differential ultrasonic attenuation of fibrous tissues such as cancers, and by cysts, respectively. The darker region or columnar shadow below a cancer is caused by its higher relative attenuation properties. The brighter enhancement beneath the cyst, a region of higher intensity when compared to the background, is caused by the lower relative attenuation of the water-filled cyst. Strong scattering phenomena including refraction and total internal reflection resulting from speed of sound differences are also responsible for these anisotropic artifacts, which are highly dependent on the insonification direction of the ultrasound transducer.

Compounding, wherein images are acquired at different beam angles and then averaged with varying degrees of sophistication, has been used extensively to eliminate these artifacts [Entrekin et al., 2001, Moskalik et al., 1995, Treece et al., 2007]. However, in practice, a compounded scan would increase the acquisition time of an automated ultrasound scan unacceptably. Currently, in our setup, a single angle full breast scan (15 cm in length) takes less than five minutes, but if multiple angle scans were required to be taken at different times from two sides of the breast, it would be highly undesirable to keep the patient's breast compressed for longer than 20 minutes. The practical difficulties posed by automated compound imaging increase our motivation for dual-sided B-mode imaging.

5.2 Materials and Methods

5.2.1 Experimental Phantom Design

To eventually achieve successful registration of dual-sided in-vivo images, we conducted early experiments with the simpler, reproducible case of a breast-mimicking phantom containing 39 lesions in all, 21 of which simulate cancers and

18 of which simulate cysts. These produce realistic artifacts and provide contrast detectability. The attenuation coefficients of the hypoechoic lesions are not typical of similar lesions in breast tissues, but that particular physical property was not considered essential for these tests. This custom-designed phantom simulates the breast compressed in the mammographic cranio-caudal geometry and was built by E.L. Madsen and G. Frank at the University of Wisconsin, Madison. The phantom is a rectangular solid (Length = 18 cm, Width = 8.5 cm, Height = 6.4 cm), with a 5 cm thick lesion-embedded slab sandwiched between two 7 mm thick aberrating layers of tissue-mimicking subcutaneous fat. The phantom is bounded by acrylic walls and the scanning windows on the top and bottom are covered with 25 μm thick Saran wrap (see Figure 5.3). Pedestal anchors have been inserted for structural stability.

The fat and glandular-mimicking materials are oil-in-gelatin dispersions, while the lesions contain no oil. There are two types of glandular material having slightly different sound speeds. The tissue-mimicking fat has an even lower speed of sound. The oil produces a lowered propagation speed and density and contributes to attenuation. The single hyperechoic lesion contains water-based gelatin with powdered graphite and glass beads (45-53 μm in diameter) [Madsen et al., 1982]. The tissue-mimicking subcutaneous fat layers have scalloped surfaces in order to replicate refraction effects simulating those in an actual human breast. The geometric simplicity of this refracting layer allows for potential quantitative analysis and correction of refraction errors.

The 39 lesions are exactly positioned in the tissue-mimicking glandular region (see Figure 5.4). Each 1.25 cm thick depth zone contains at least 4 'cancers' and 4 'cysts' to provide sufficient statistical test cases per zone [Kofler and Madsen, 2001] when image sweeps at two or more viewing angles are employed. Also, two large double-cone shaped 'cancers' (to partially mimic their irregular shape *in vivo*), one large spherical 'cyst' and one large hyperechoic spherical 'cancer' have been included

Tissue-Mimicking Material	Relative contrast (dB)
High speed glandular	0
Low speed glandular	-7
Hyperechoic lesion	+5
Hypoechoic lesions	-11
Cysts	Anechoic
Fat	-10

Table 5.1: Relative contrast of materials in phantom.

in this phantom. Randomly positioned knots on three 0.3 mm diameter nylon fibers in the central area of the phantom create more echogenic structural elements. A small (1% by volume) concentration of formalin raises the melting point of the materials (by means of formaldehyde cross-linking) to 100°C, and a 5% concentration of 1-propanol is included for preservation.

The first version of this phantom was designed with acoustic properties that appear in the ultrasound literature, specifically in a breast phantom used for the ACRIN 666 trial [Madsen et al., 2006]. This phantom was found to produce minimal shadows (see Figure 5.5). A second phantom with substantially greater contrast in speed of sound, using recently published values from ray-traced ultrasonic CT [Duric et al., 2007] produces image shadows similar to those often seen *in vivo* (see Tables 5.1 and 5.2), largely because of refraction and total internal reflection effects. Attenuation coefficients were almost identical and the speeds of sound of the lesions were similar to the original version, but the speeds of sound in the glandular material and fat were reduced by 100m/s and 40m/s, respectively. This experience suggests an explanation for the significant edge enhancement of transmission images of attenuation.[Lehman et al., 2000]. Angled and irregular boundaries between tissues of quite different speeds of sound might produce differential attenuation and shadows observed in pulse echo images.

Tissue-Mimicking Material	Speed (m/s)	Atten. coeff. at 8 MHz (dB/cm)	Atten. coeff. at 10 MHz (dB/cm)
High speed glandular	1455	3.44	5.26
Low speed glandular	1423	3.61	4.61
Hyperechoic lesion	1550	9.54	11.76
Hypoechoic lesions	1539	11.81	15.64
Cysts	1544	1.26	1.59
Fat	1412	4.07	5.25

Table 5.2: Relevant physical properties of materials in final version of phantom

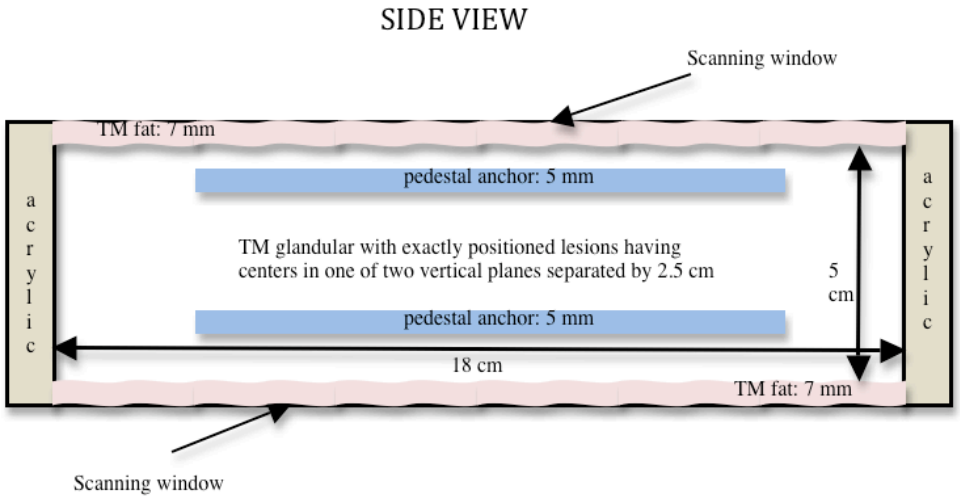

(a)

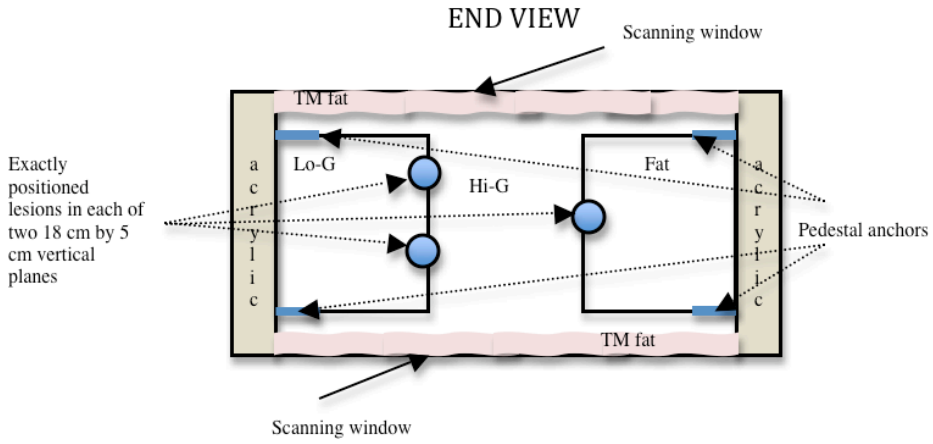

(b)

Figure 5.3: (a) Schematic of phantom: (a) End View (b) Side View.

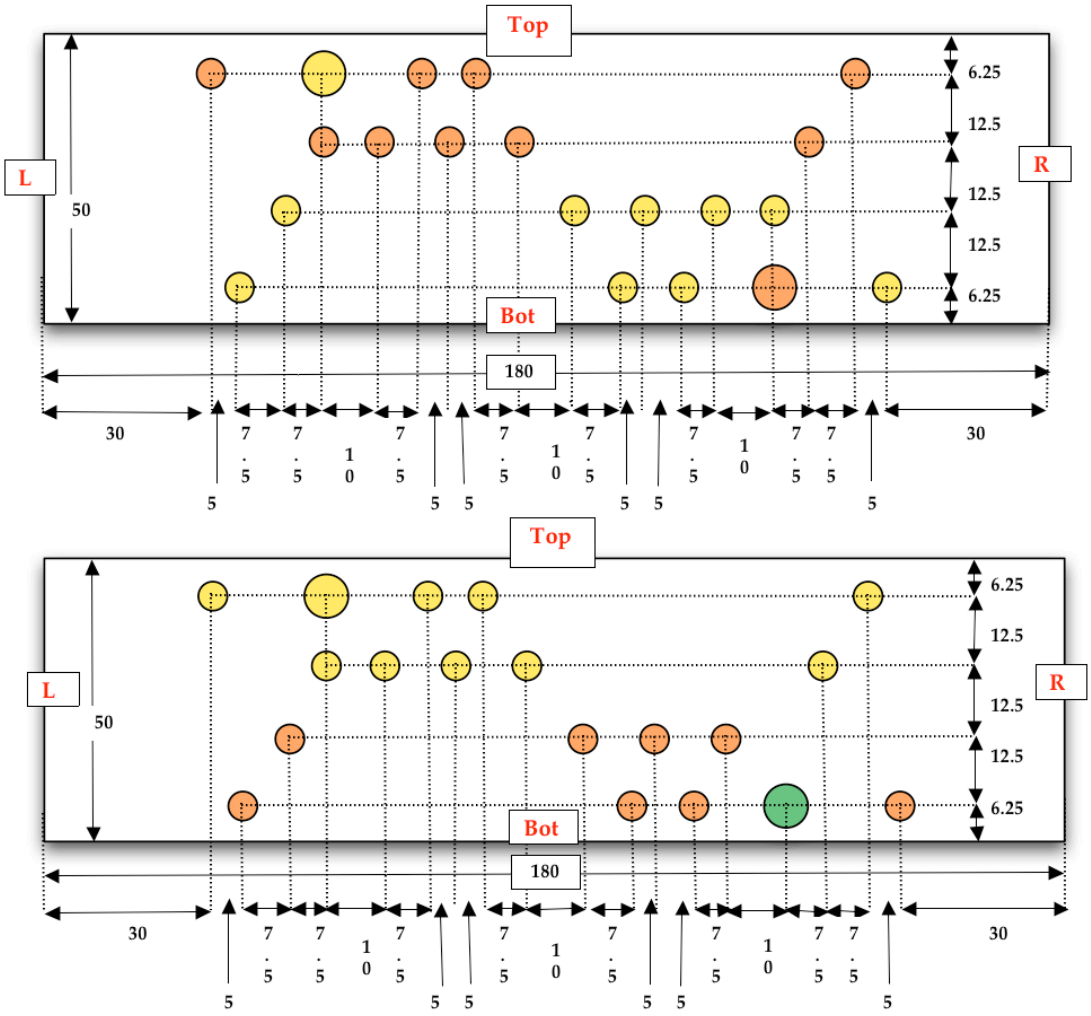

Cyst: **A**-5 mm, **AL**-8 mm.	
Hypoechoic high att.: **B**-5 mm, **BcL**-8 & 10 mm.	
Hyperechoic high att: **CL**-8 mm.	

Figure 5.4: Geometric layout in phantom within the two lesion-containing 18 cm x 5 cm planes.

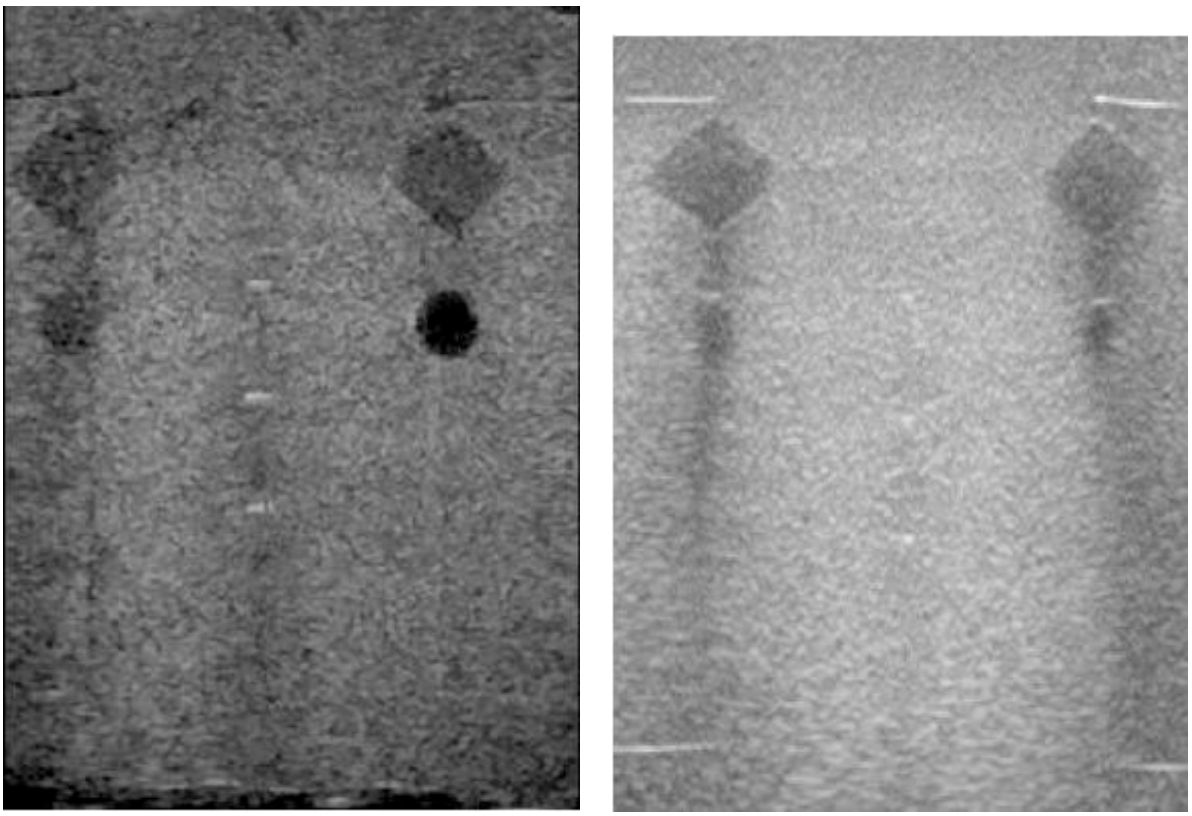

(a) (b)

Figure 5.5: Cancer-like double cones and cysts imaged with the same TGC settings in versions 1 and 2 of the phantom [(a) and (b)]. Note absence of significant shadowing on (a), due to lower speed of sound differences between lesions and background.

5.2.2 Machine learning for breast ultrasound image quality assessment

Machine learning classifiers were used to classify image regions in the bottom half of the ultrasound images, which is the region of overlap between opposed views, into useful and less useful information for image fusion and registration purposes. Machine learning has been used with considerable success for identifying suspicious masses on ultrasound images [Kotropoulos and Pitas, 2003, Piliouras et al., 2004]. Kotropulos et al. achieved a leave-one-out accuracy of 84% in lesion detection and Piliouras et al. were 98.7% accurate in separating cancerous lesions from other lesions. Drukker et al [Drukker et al., 2003] achieved a sensitivity of 100% at 0.43 false-positive malignancies per image, when they undertook computerized recognition of shadow regions on breast ultrasound images for detection and classication of cancerous lesions.

Support Vector Machines

Support Vector Machines (SVMs) are derived from statistical learning theory [Vapnik, 1999]. An SVM is based on the structural risk minimization principle. Support vector machines locate the hyper-plane that maximizes the margin between two separate sets in the training data. For data 'x_i', i = (1,. . . ,n), this classifier finds the best hyperplane ($y_i = wx_i + b$) by solving a constrained optimization problem (using Lagrange multipliers):

$$\min_{\mathrm{w,b}} \frac{1}{2}||\mathrm{w}||^2 \tag{5.1}$$

given that:

$$\mathrm{y_i}(\mathrm{wx_i} + \mathrm{b}) - 1 \geq 0 \tag{5.2}$$

SVMs are well suited to handling imbalanced data sets. Since we have more 'good'

regions of interest (ROIs) than corrupted or 'bad' ROIs, this inherent asymmetry in our data makes SVMs a good choice for our purposes. We decided to use SVM^{light}, an open source program which can process thousands of support vectors, has low computational requirements and is fast and efficient [Joachims, 2008]. A linear kernel was sufficient for our purposes.

Artificial Neural Networks

An artificial neural network (ANN) is a non-linear machine learning classifier that is made up of artificial 'neurons', which are joined by varying weights [Widrow and Lehr, 1990]. It attempts the conceptual approximation of a functional unit of the human brain. Learning is implemented by using a 'connectionist approach'. A feedforward network is the simplest form of an ANN, in which outputs are not directly cycled back to inputs. Multi-layer perceptrons are commonly used types of ANNs, specifically trained by backpropagation. Generally, sigmoid functions drive the outputs of individual neurons. The ANN used for this classification (MATLAB's 'nprtool') consisted of 20 neurons in a feed-forward network with one hidden layer, trained by scaled conjugate gradient backpropagation.

For training and testing the two classifiers described above, we obtained ultrasound images on our breast-mimicking phantom. Early attempts at classification of compressed phantom data with SVMs were jointly conducted with F. Hooi, also at the University of Michigan. ROIs affected by different types of lesions were proportionately distributed amongst training (40%), testing (40%) and validation sets (20%). In order to train the classifiers, the phantom image regions were manually labeled. Eventually, pixel data was decompressed prior to feature extraction. First order image statistics of overlying image pixel columns were sufficient. Six features were extracted, mean and standard deviation of the ROI itself and two ROIs above it.

I also had access to *in vivo* breast images of cysts and cancers and an MQSA-certified radiologist located each mass for labeling purposes. Due to the limited size of these datasets which included 14 cancer cases and 9 cyst cases, they were split only two ways, using 60% of the data for training and 40% for testing. 13 features were employed for cancers, which included mean, standard deviation, ten histogram bins and skewness of the ROIs. Similar features were used for cysts, but ROIs were divided in half to take advantage of the nature of enhancement artifacts where bright areas lie below anechoic regions. The 15 features included mean and standard deviation of each half of the ROI.

Guided classification of phantom data

The dataset consisted of two 323-slice volumetric ultrasound images of the breast phantom. These opposed views were obtained through the top and bottom of the phantom by rotating it and using the single-sided scanning apparatus depicted in Fig. 5.1(a). As artifacts in ultrasound images are very angle dependent, these two views provided significantly different realizations of the same cysts and cancer-like lesions in the phantom. For example, a shadow cast by a cancer-like lesion will point in the exact opposite direction on the top view when compared to the bottom view (see Figure 5.6).

A two-step approach to the problem was adopted, beginning with a guided classification. For this classification, we characterized ROIs in the image as good or bad data by examining overlying structures, because these directly affect the quality of data in the ROIs. Since we knew the precise locations of all the lesions in the phantom and the resulting artifacts, we labeled regions in the image accordingly as (lying below) cancers, cysts or background. The 'bad' data were selected as data lying below a cancer or cyst, while 'good' data were data in the central glandular region that were unaffected by any lesion, and which we will refer to as 'background. We classified these ROIs two ways: cancers vs. cysts, and cancers vs. background.

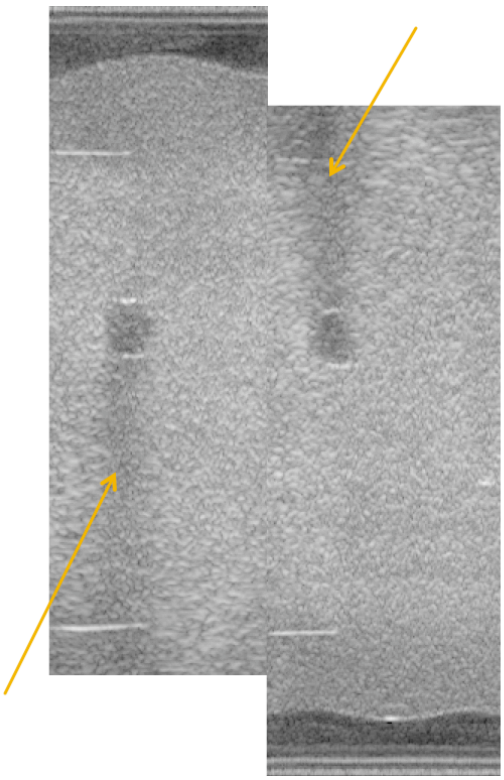

Figure 5.6: Top and bottom views of the same cancer-like lesion in the breast phantom: arrows point to shadows.

We did not attempt cysts vs. background because in the phantom the cysts did not enhance underlying areas significantly, as they would *in vivo*.

Every lesion was clearly visible on approximately 9 image slices. The slices were spaced 0.4 mm apart and the lesion diameter was 5 mm. 24 lesions were imaged (we excluded image slices containing the larger lesions at this stage). 12 of these lesions cast significant shadows on the top view and 12 on the bottom view. Images obtained from the top view were designated as the training dataset, and the images obtained from the bottom view were used as the testing dataset. This could be done because of the inherent top-bottom symmetry of the phantom.

The features chosen for the SVM for each ROI were the mean, standard deviation and seven bin histograms of local pixel amplitude values in a 15x15 window of pixels lying directly overhead. Table 5.3 and Figure 5.7 present a comparison of grayscale features for example ROIs that were found in the background and below a cancer

ROI	Mean	Standard Deviation)
Background	163.76	16
Below Cancer	125.98	17.98

Table 5.3: Feature comparison (grayscale, log-compressed data) for one example of guided classification input (also see Figure 7).

respectively.

Robust classification of phantom data

As our goal of using SVMs is to automate the removal of corrupted data for image fusion and registration purposes, we investigated automated classification of fixed size ROIs in the entire image volume. To simulate this more general application, we selected ROIs from random slices independent of knowledge of lesion location and attempted to classify these ROIs with the model developed by the previous technique. This method allowed us to demonstrate the effectiveness of the SVM in picking out regions of good and bad data automatically with no user guidance.

We divided each ultrasound image into feature ROIs of 30 by 30 pixels wide (the lesions were approximately 30 px wide on the image, so the shadows were rarely wider than 30 px) and labeled these manually(see Fig 5.8). Our first attempt at classification resulted in an accuracy of less than 50%. This was obtained with the same set of features that we used for guided classification.

To improve accuracy, we modified our feature set to include the features from ROIs themselves, along with those from three overlying ROIs. There were 17 features in all. Several first order statistics parameters were used as features to describe the main ROI, including mean, standard deviation, a seven bin histogram and skewness. Depth at which the ROI was located was also used. (See Table 5.4 and Figure 5.9.) We included skewness because true ultrasound data usually has a Rayleigh distribution with a positive skewness value [Abramowitz and Stegun, 1972]. This author hypothesized that the distribution of corrupt data would usually be more

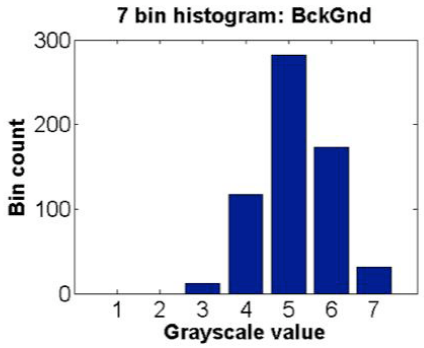

(a)

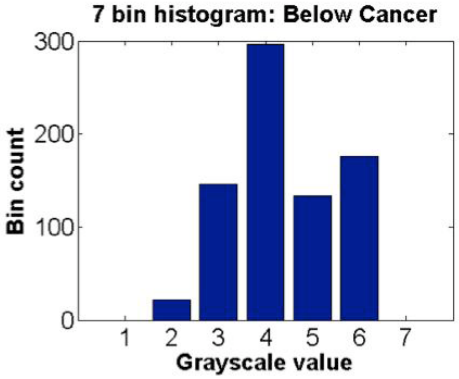

(b)

Figure 5.7: Seven-bin histograms for: (a) Background/normal ROIs (b) ROIs below cancer-like lesions in the phantom.

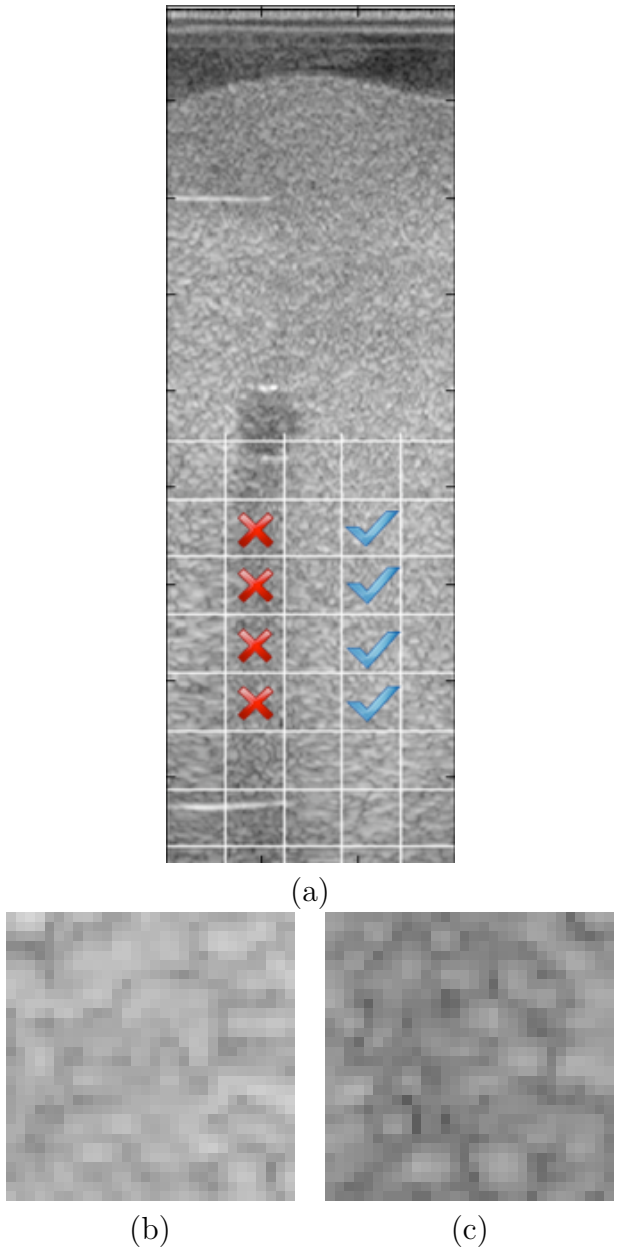

Figure 5.8: (a) Examples of 'good' and 'bad' data ROIs in a phantom image, indicated by check marks and crosses respectively. (b) Good data ROI (c) Bad data ROI.

Feature	True ROI	Corrupt ROI
Mean	5095.74	2369.3
Stdev	1610.69	823.41
Mean (1 above)	4214.42	2682.55
Stdev (1 above)	1348.9	2821.53
Mean (2 above)	3798.5	1044.34
Stdev (2 above)	1257.84	1130.71

Table 5.4: Examples of linearized/ decompressed data features for authentic ROIs vs corrupt ROIs at the same depth in the breast phantom.

Gaussian in appearance, with a lower value of skewness. A median filter was used to smooth the image. The size of the filter window was equal to the speckle spot size of the ultrasound image (3x3 px). For each case, we also investigated the influence of different kernels in classification.

After extensive testing, we found that the first order image statistics of overlying image pixel columns after decompression provided sufficient features for the classifier. Six features were extracted, mean and standard deviation of the ROI itself and two ROIs above it. Median filtering did not improve our accuracy values.

Guided classification of *in vivo* data

This author also applied these classifiers to clinical breast image data. An MQSA-certified radiologist identified and localized shadows caused by cancers and enhancement caused by cysts. We attempted to separate shadows cast by cancers from background, and also to separate enhancement caused by cysts from the background. 10 features were initially chosen: mean, standard deviation, (for a columnar ROI of fixed width and height: 6x60 px), histogram and skewness. The 6 px ROI column width was chosen as it provided better results than either 3 or 9 px. Other ROI widths were not tested. The ROIs were manually selected, given the prior localization information.

The feature set for cysts was modified by dividing the ROI column into halves height-wise and assessing mean and standard deviation separately for these, adding

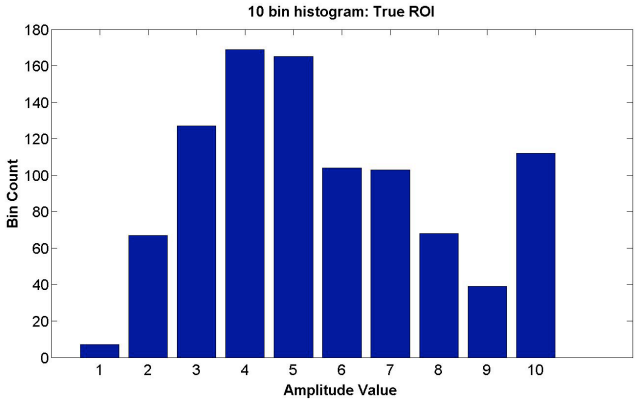

(a)

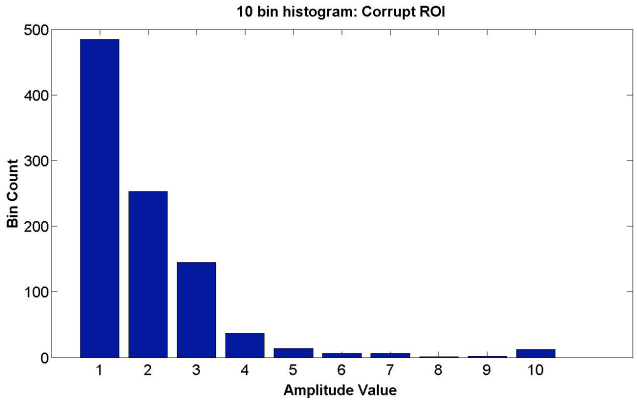

(b)

Figure 5.9: Ten-bin histograms for: (a) 'True' or background data ROIs (b) 'Corrupt' ROIs below cancer-like lesions in the phantom.

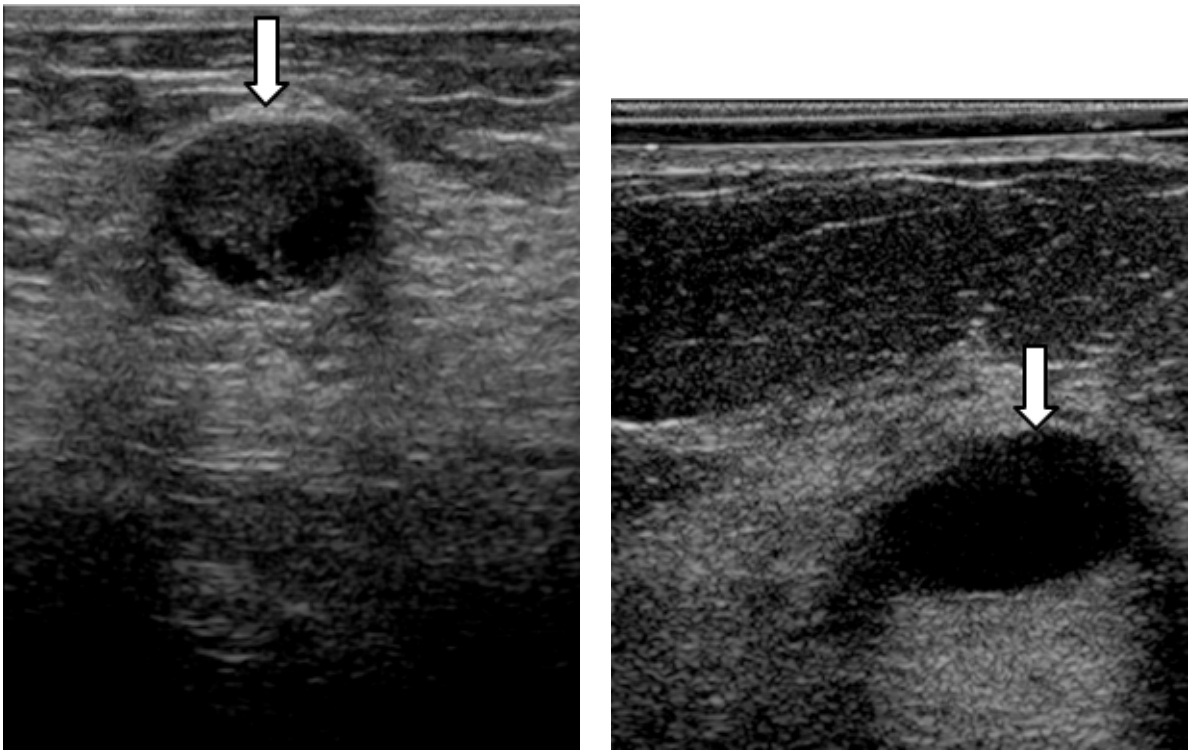

(a) (b)

Figure 5.10: (a) and (b): Examples of enhancement caused by cysts (indicated by arrows).

two more features to this set. Intuitively, one would expect this feature set to perform better because the enhancement below a cyst is always associated with a dark area inside the cyst above. Images of cancerous lesions and cysts were available for 12 patients and 10 patients respectively. Of these images, the location of the mass was verified by the radiologist on a smaller subset: 14 image volumes for 10 cancer patients and 9 image volumes for 8 cyst patients. Although many data points were available for each image volume, these did not vary enough to justify a 3-way split for training, testing and validation. Hence leave-one-out cross-validation was implemented.

See Figures 5.10-5.11 and Table 5.5 for features selected in the cyst data set. See Figures 5.12-5.13 and Table 5.6 for features selected in the cancer data set.

Feature	Background ROI	ROI within cyst and enhancement
Mean(top half)	1112	102
Fractional Stdev(top half)	0.88	0.96
Mean(bottom half)	1417	1250
Fractional Stdev(bottom half)	0.72	1.31
Amplitude bin 1	5	5
Amplitude bin 2	9	30
Amplitude bin 3	16	21
Amplitude bin 4	12	15
Amplitude bin 5	10	12
Amplitude bin 6	10	9
Amplitude bin 7	7	11
Amplitude bin 8	3	4
Amplitude bin 9	11	2
Amplitude bin 10	14	2
Skewness	1.54	3.81

Table 5.5: Examples of linearized/ decompressed data features for cysts vs background.

Feature	Background ROI	Cancer ROI
Mean	830	47
Fractional Stdev	1.34	0.53
Amplitude bin 1	210	356
Amplitude bin 2	104	4
Amplitude bin 3	37	0
Amplitude bin 4	1	0
Amplitude bin 5	2	0
Amplitude bin 6	3	0
Amplitude bin 7	3	0
Amplitude bin 8	0	0
Amplitude bin 9	0	0
Amplitude bin 10	0	0
Skewness	2.21	2.14

Table 5.6: Examples of linearized/ decompressed data features for cancers vs background.

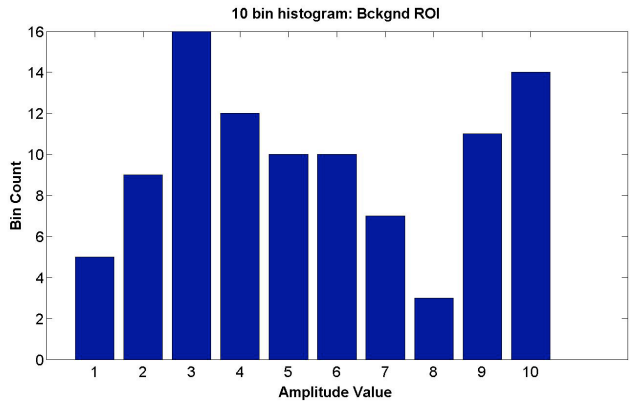

(a)

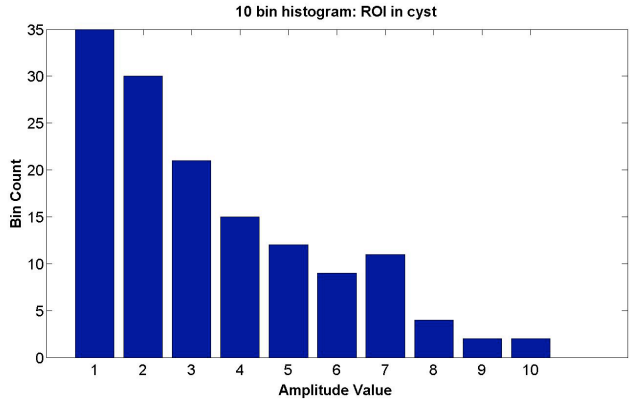

(b)

Figure 5.11: Ten-bin histograms for case 1 (a) Background/normal ROI (b) ROI within cyst in breast tissue.

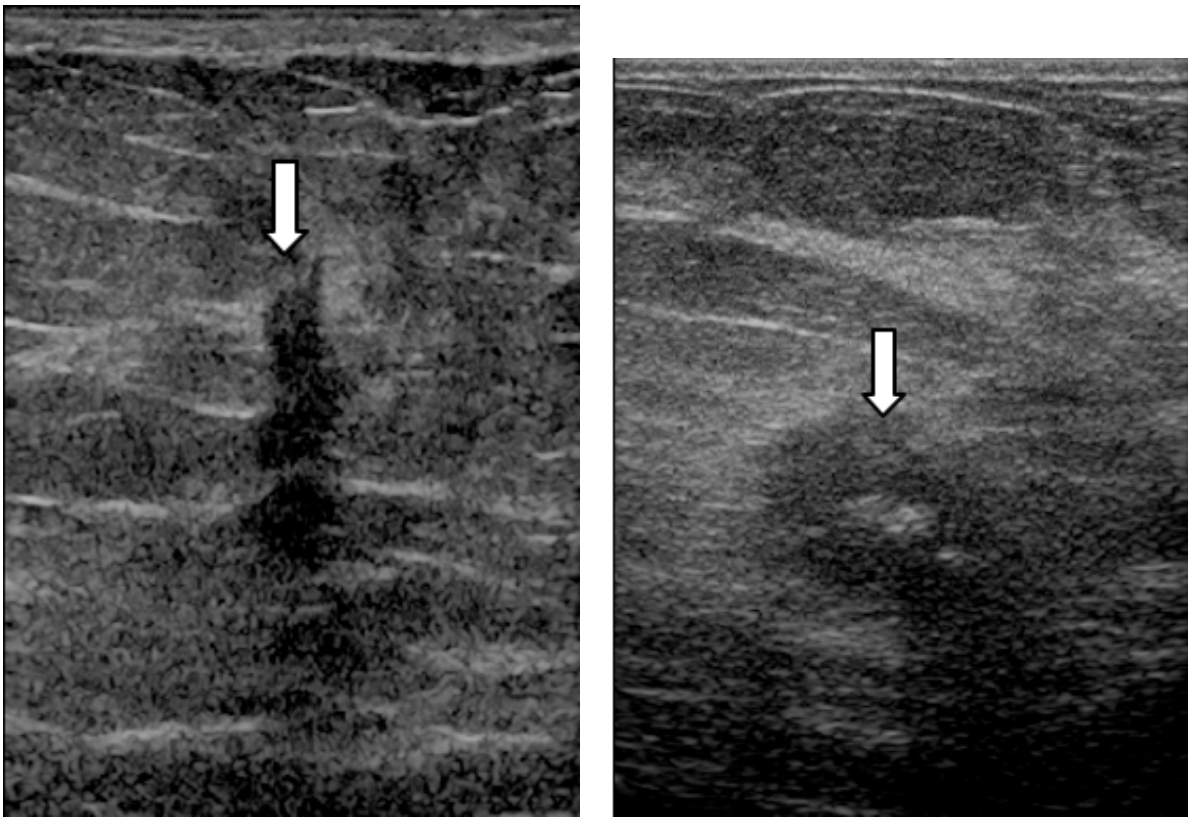

(a) (b)

Figure 5.12: Examples of shadow artifacts caused by cancers (indicated by arrows): (a) More typical columnar shadow (b) Displaced shadow offset from apparent center of cancer.

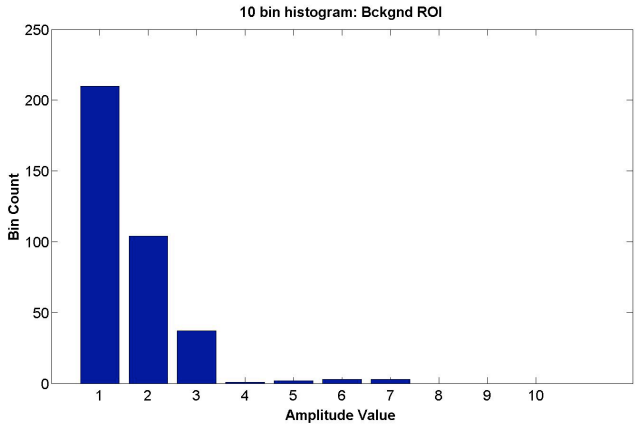

(a)

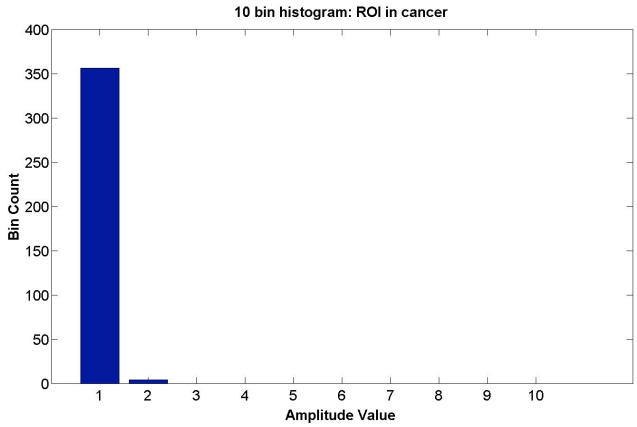

(b)

Figure 5.13: Ten-bin histograms for case 1 (a) Background/normal ROI (b) ROI within cancer in breast tissue.

5.2.3 Non-linear registration of opposed view phantom images

After segmenting the image with our classifiers (see Fig. 5.14), registration was performed with mutual information for automatic multimodality image fusion (MIAMI Fuse^{T}M , University of Michigan) non-rigid 3D registration [Kim et al., 1997, Meyer et al., 1997, Meyer et al., 1999] on the AVS platform (Advanced Visual Systems, Waltham, MA), based on the mutual information objective function (see Equation 1) and thin plate spline interpolation [Bookstein, 1997] .

$$\mathrm{I} = \sum^{\mathrm{a}} \sum^{\mathrm{b}} \mathrm{p(a,b)log_2(p(a,b)/p(a)p(b))} \tag{5.3}$$

'a' and 'b' are the two datasets to be registered in the equation above.

One image set was selected as the reference (usually the top image volume; either can be selected). The other image set (called the target or homologous image) was spatially transformed to align with the reference frame. We registered the two 3D image sets by selecting 9 or more corresponding control points placed at key features, e.g. edges of lesions or echogenic knots. These points were employed as control points by the software and were moved to optimize the so-called mutual information (MI) of the two image volumes.

5.2.4 Non-linear registration using principal components

Eight human studies were selected for this preliminary evaluation: 4 cyst cases and 4 cancer cases. In the absence of a true dual-sided imaging setup, single sided images were duplicated and the copy synthetically warped to replicate the artifacts that might arise in dual-sided images (See Figure 5.15). The original image set was selected as the 'reference'. The warped image set (called the target or 'homologous' image) was spatially transformed to align with the reference frame.

The synthetic warping procedure was carried out as follows [Krücker et al., 2002].

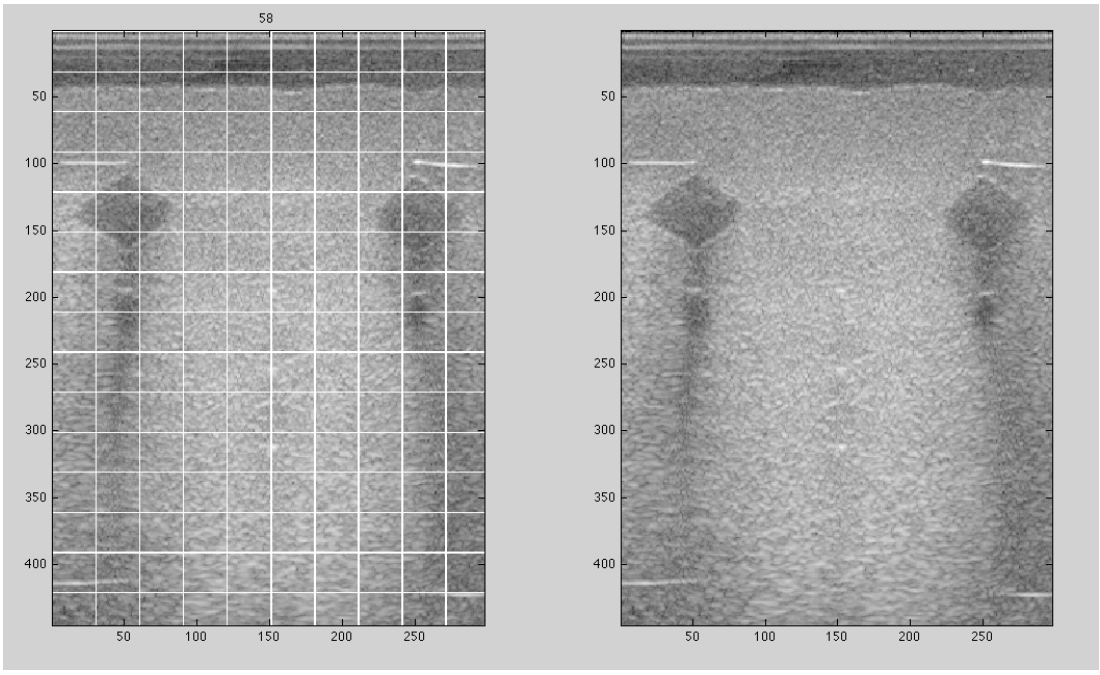

(a)

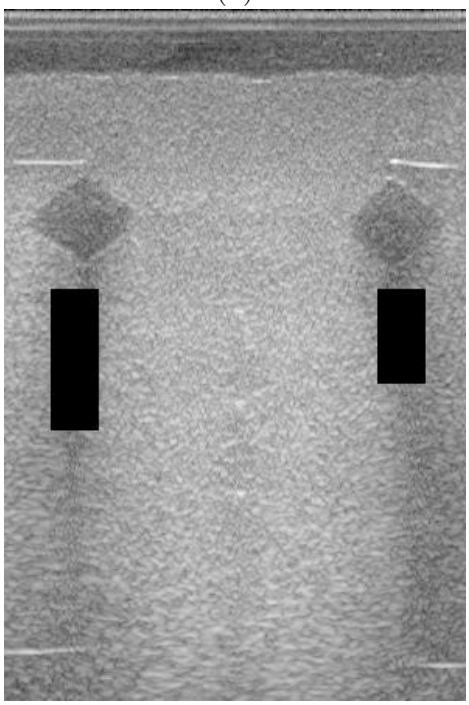

(b)

Figure 5.14: (a)See grid superimposed on image on left, and original image on right. (b)Regions of corrupt data masked by trained machine learning classifier.

Firstly, a uniform grid of points was generated. Then a random translation of up to 5 mm was added to each grid point in x and y. Finally, another random shift vector was added to each reference point in x and y. The mean deformation between the original and shifted points was scaled to 1.2 mm, which is a realistic estimate of observed warp deformation values [Krücker et al., 2002]. The mean deformation D was calculated over the image volume 'V' as:

$$\mathrm{D} = \frac{1}{\mathrm{V}} \int\int\int |\mathrm{x} - \mathrm{T(x)}| \mathrm{d}^3\mathrm{x} \tag{5.4}$$

where x and T(x) are the spatial locations inside the original and warped image volumes respectively. 3-degree polynomials were fitted to the two sets of points. The entire image was then warped by these polynomials.

Principal Component Analysis (PCA) [Jolliffe, 1986] projects data onto a lower dimensional space, ordering the basis vectors such that the projection onto the first vector captures the maximum variance in the data (see Equations 5.5, 5.6 and 5.7) . Every succeeding vector describes as much of the remaining variability as possible. PCA uses the eigenvalue decomposition of the data covariance matrix XX^T (where 'X' is the data) after mean centering. The eigenvalue decomposition provides a set of eigenvectors $\mathrm{e_i}$ corresponding to eigenvalues λ_i. The first PCA component is the projection of the data onto the first eigenvector e_1 (corresponding to the largest eigenvalue λ_1). Let the data 'x' be such that:

$$\mathbf{x} = (\mathrm{x}_1, ..., \mathrm{x}_\mathrm{n})^\mathrm{T} \tag{5.5}$$

Let the mean of this population be $\mu_x = \mathrm{E(x)}$. Then the covariance matrix is obtained as:

$$\mathrm{C_x} = \mathrm{E}[(\mathrm{x} - \mu_\mathrm{x})(\mathrm{x} - \mu_\mathrm{x})^\mathrm{T})] \tag{5.6}$$

An orthogonal basis can be calculated by finding the eigenvalues and eigenvectors of the symmetric covariance matrix. These eigenvectors and their corresponding eigenvalues are the solutions of the following equation:

$$C_x e_i = \lambda_i e_i, i = 1, ...n \tag{5.7}$$

In our study, the PCA basis vectors were extracted from 30 adjoining image slices, spaced 0.4 mm apart. Most masses are 1.2 cm or larger and often their appearance does not change over this scanning distance. A stack of 30 slices was found to reduce noise without blurring details unacceptably. These slices were taken from automated ultrasound image volumes. A single image from the center of the 30-image stack was then projected onto the first basis vector. This projection appeared to have captured the most relevant image information for our purposes. There was however, some loss of edge information along with the significant reduction in speckle, clutter and other noise (see Figure 5.15).

Image registration was performed with mutual information as in Equation 5.2.3. Two sets of control points were independently marked by the author and a radiologist in the original('reference') and warped('homologous') images, thus partially compensating for the effect of the arbitrary selection of these points.

Registration error was estimated by finding a different set of ten fiducial points in the reference image and the registered homologous image and measuring the Euclidean distance between the locations of each point on the two images. Two expert readers (MQSA certified radiologists) independently marked these points for each case. The measurements were averaged to produce the final estimate of fiducial registration error.

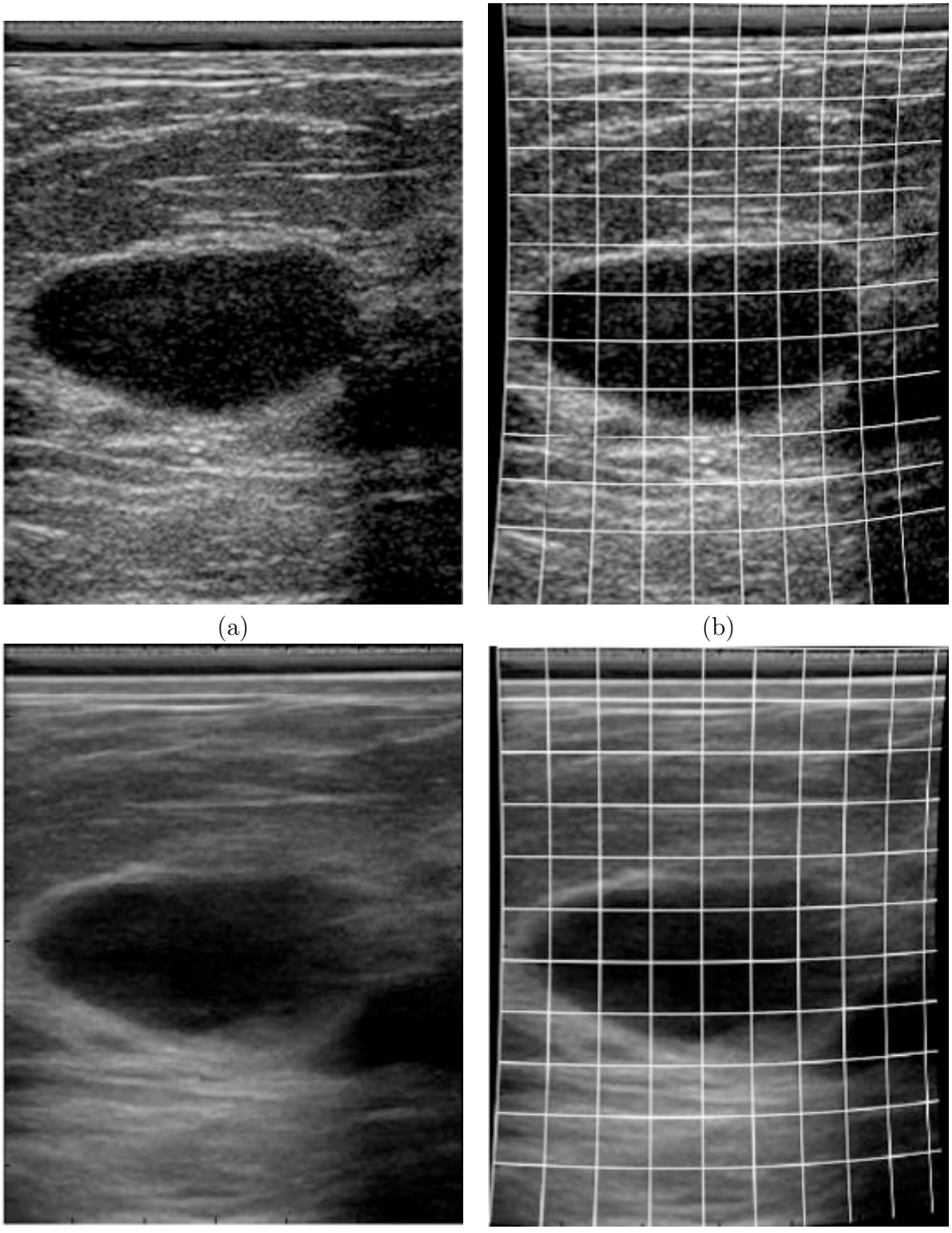

Figure 5.15: (a) Original image containing cyst. (b) 3-degree polynomial warped result. (c) PCA first component. (d) 3-degree polynomial warped result for PCA first component.

5.3 Results and Discussion

5.3.1 Classification of phantom data

For guided classification of ROIs chosen from areas below lesions and in the central background of the breast phantom we obtained near-perfect accuracy of 98%, using an SVM with a linear kernel. The SVM and ANN both achieved excellent accuracy of about 97% for the automated classification of true and corrupt image regions in ultrasound data obtained from the breast phantom. For both classifiers, using the first two features alone (mean and standard deviation) gave us an accuracy of 90%. Using different kernels and median filtering images prior to feature selection did not significantly impact accuracy. The computation time was negligible for both classifiers.

5.3.2 Classification of *in vivo* data

For classification of ROIs in the cancer dataset as either true or distorted by a cancer, SVMs were 94% accurate. For classification of ROIs in the cyst dataset as either true or distorted by a cyst, accuracy was 93%. ANNs were 91% and 89% accurate respectively. Leave-one-out cross-validation showed an average accuracy of 92% for both datasets. Once again, using different kernels and median filtering images prior to feature selection did not improve accuracy.

5.3.3 Non-linear registration of opposed view phantom images

A full affine transform did not succeed in aligning the two opposed views (see Fig. 5.16).

Non-linear registrations were carried out for 9 or more control points. See Tables 5.7 and 5.8 for registration error values over multiple runs for the original phantom images and the segmented phantom images respectively. Mutual information values were actually slightly lower for segmented images, and not indicative of registration

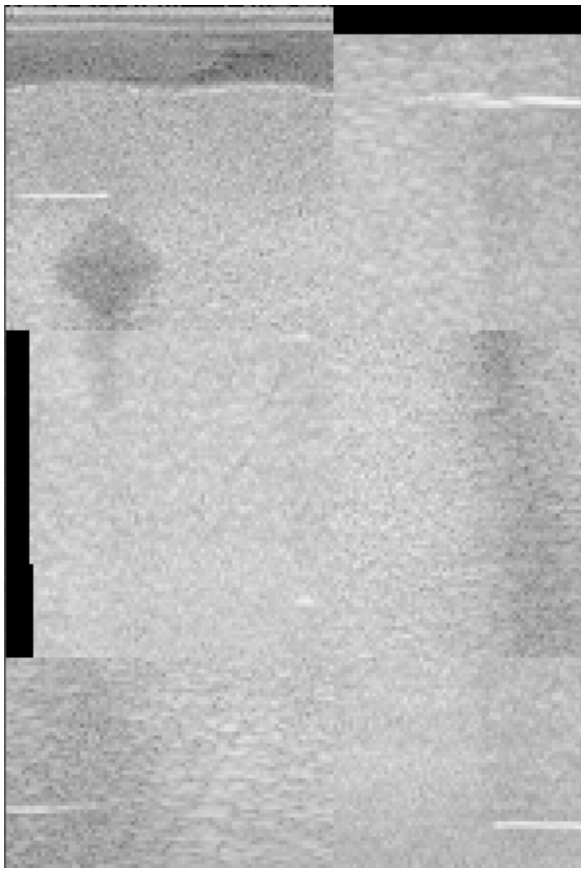

(a)

Figure 5.16: Checkerboard image of mis-registered homologous image, using a full affine transform

Case	Mean error in x(mm)	Standard Deviation of error in x(mm)	Mean error in y(mm)	Standard Deviation of error in y(mm)
Orig 1	0.49	1.06	0.272	1.01
Orig 2	9.54	14.22	8.619	15.69
Orig 3	13.92	6.89	11.9391	13.09
Orig 4	0.50	0.46	0.85	0.69
Orig 5	12.57	7.85	9.2565	7.77
Orig 6	0.69	0.43	1.0846	0.85

Table 5.7: Registration error in x and y for the unsegmented original images; note that cases 2, 3 and 5 did not register at all.

Case	Mean error in x(mm)	Standard Deviation of error in x(mm)	Mean error in y(mm)	Standard Deviation of error in y(mm)
Seg 1	0.71	0.74	1.39	1.91
Seg 2	0.57	1.28	0.53	1.84
Seg 3	0.78	0.80	1.34	2.31
Seg 4	0.83	0.97	1.72	2.83
Seg 5	0.83	0.88	1.74	2.76
Seg 6	0.77	0.81	1.58	2.06

Table 5.8: Registration error in x and y for the segmented images.

accuracy. Error was calculated by averaging the distances between lesion centers in the reference image and the registered homologous image. The centers were marked by hand and then shifted slightly to an optimal position by correlating the surrounding region with a lesion-sized mask. Note that for cases 2, 3 and 5, the original phantom images were grossly misregistered (see Figs 5.17 and 5.18 for examples from case 3).

Since the natural structure of the phantom is such that lesions are divided into four zones depth-wise (1.25 cm each), CNR (contrast-to-noise ratios) for these zones show where the signal begins to degrade substantially. There is only a slight reduction in average lesion CNR while moving from the surface down to the zone directly below it (4.5% and 2.1% respectively for each view), and average CNR dropped by 25% while moving one zone further down. Decisions must be made

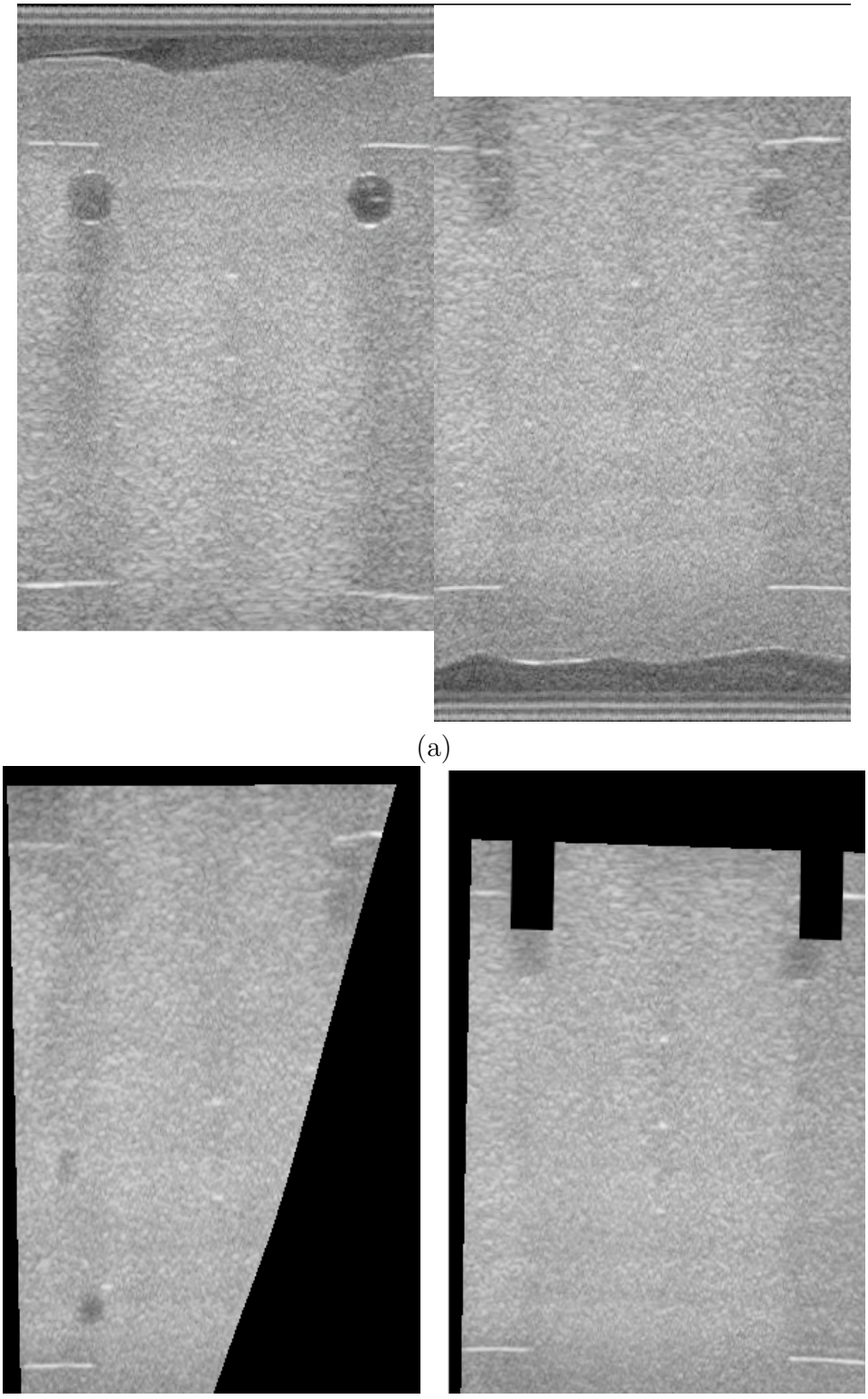

Figure 5.17: (a)Reference image and homologous image taken from opposite sides (b)Misregistered homologous image slice, using a warp transform on the original image(c) Same registered homologous image slice, using a warp transform on the segmented image

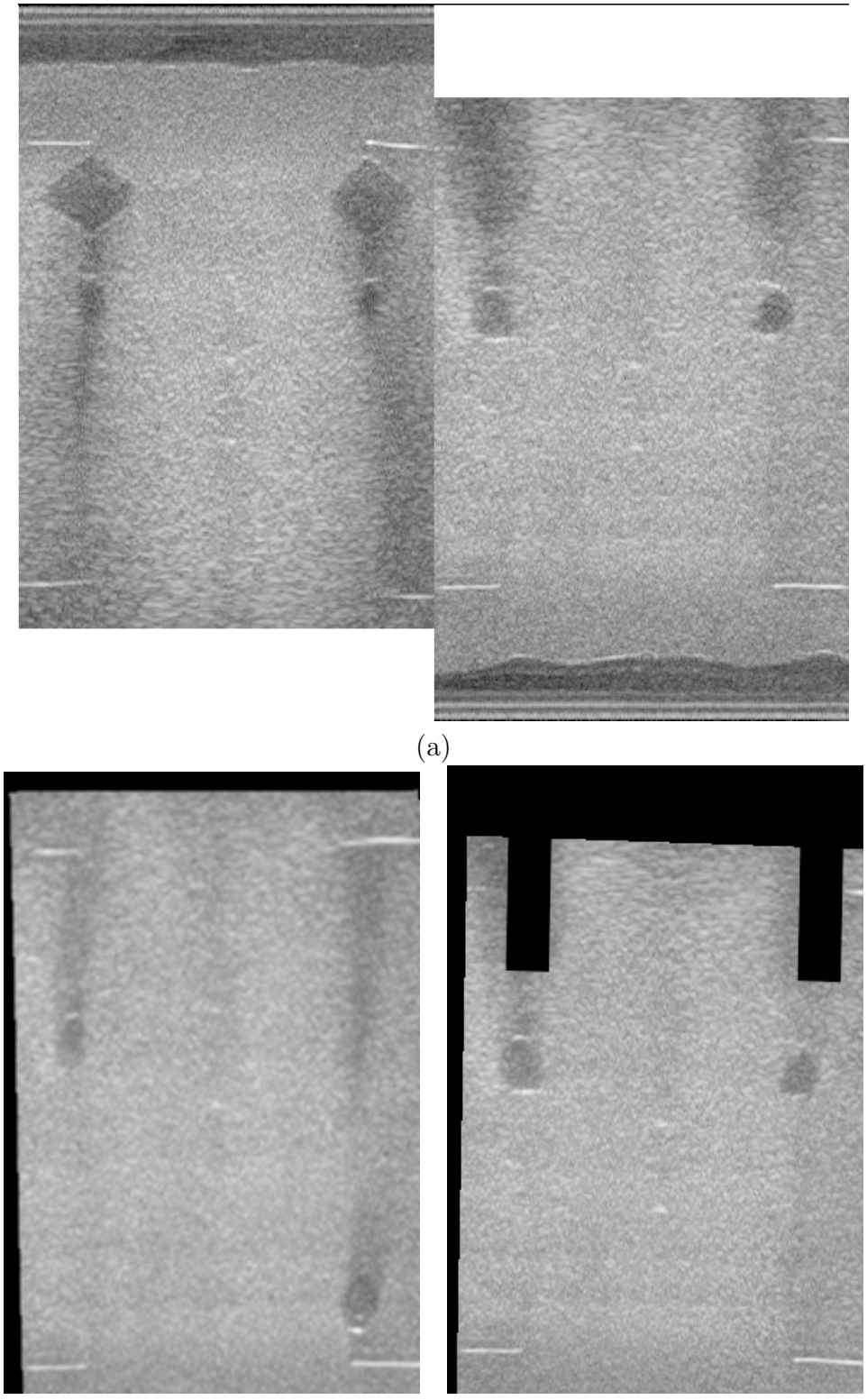

(a)

(b) (c)

Figure 5.18: (a)Reference image and homologous image taken from opposite sides (b)Misregistered homologous image slice, using a warp transform on the original image(c) Same registered homologous image slice, using a warp transform on the segmented image

regarding the selection of image regions in the central two zones, where quality is highly variable and overlap from the two views is usual.

The proposed algorithm for constructing the combined image set retains the original image information in the top and bottom, while fusing the central zone post-registration as follows: if certain image regions have been masked as corrupt on both sides, then fill in those pixels with a pixel by pixel average of the original image information. If an image region is masked only on one side, retain pixels from the unmasked side. Finally, if the machine learning algorithm has not eliminated a particular image region on either side, replace those pixels with the maximum of the two sides. Examples of fused images from the phantom are in Figures 5.19 and 5.20. Note the clear margins of the hypoechoic lesions and the clear delineation of bottom structures in Fig 5.19(b), and the marked improvement in visibility of underlying lesions in Fig 5.20(b). However, resolution is lost on the filaments seen in cross section on a line down the center. The averaging of data from both views causes blurred or even duplicate target points due to registration error or imperfect focussing in either image.

5.3.4 Non-linear registration using principal components

Mutual information values were compared for registration of the original images, the PCA first components of these images, and finally the original images using the PCA-derived warping transform. Mutual information (MI) improved for the PCA first component by 84% and 111% on average, respectively, for the two sets of control points. This effect had multiple causes, but one of those may have been image blurring. MI did not change significantly when the PCA transform was applied to the original images (see Tables 5.9 and 5.10). An exception was an increase in MI of 219% for Cancer 2, when the second set of control points was used.

See Figure 5.21 for examples of the joint 2D histograms obtained for the three stages of registration described above. Note the sharper alignment for the PCA first

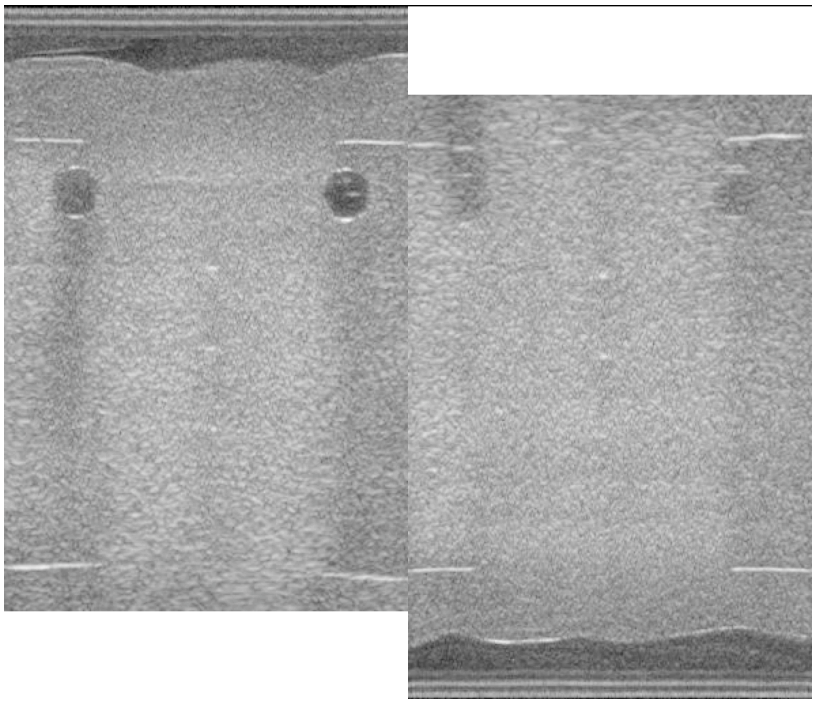

(a)

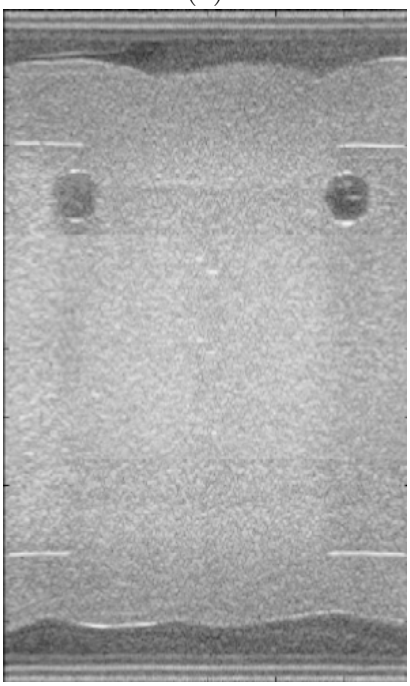

(b)

Figure 5.19: (a)Reference image and homologous image taken from opposite sides (b)Fused image after registration

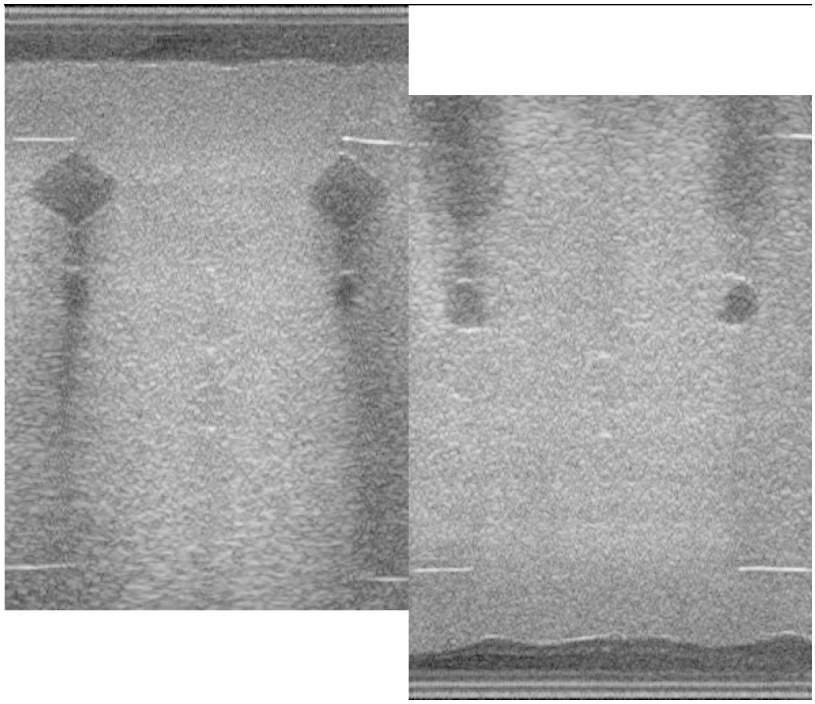

(a)

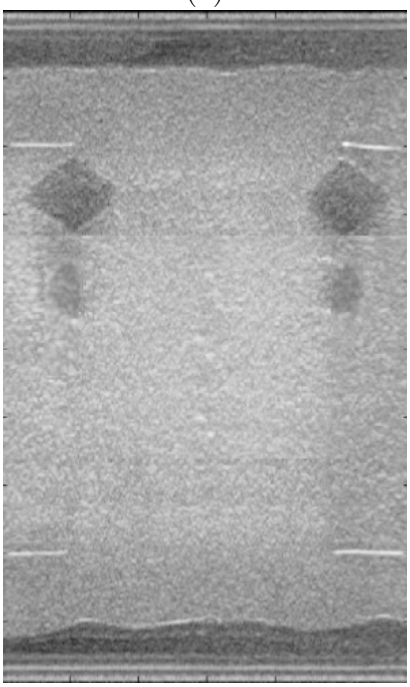

(b)

Figure 5.20: (a)Reference image and homologous image taken from opposite sides (b)Fused image after registration

Case	MI: Original	MI: PCA	MI: Original with PCA TRANSFORM
Cyst 1	1.13	2.04	1.16
Cyst 2	1.14	2.11	1.14
Cyst 3	1.23	2.08	1.01
Cyst 4	0.73	1.63	0.73
Cancer 1	1.11	1.96	1.13
Cancer 2	0.6	1.17	0.63
Cancer 3	1.25	2.05	1.24
Cancer 4	0.94	1.96	0.95

Table 5.9: Comparison of mutual information (MI) values obtained from registration of original images, PCA images and original images with the PCA transform, respectively, for the first set of control points.

Case	MI: Original	MI: PCA	MI: Original with PCA TRANSFORM
Cyst 1	1.17	2.04	1.16
Cyst 2	0.84	2.11	1.14
Cyst 3	1.04	2.16	1.22
Cyst 4	0.65	1.62	0.71
Cancer 1	1.13	1.96	1.13
Cancer 2	0.21	1.57	0.67
Cancer 3	1.25	2.06	1.24
Cancer 4	0.95	1.84	0.96

Table 5.10: Comparison of mutual information (MI) values obtained from registration of original images, PCA images and original images with the PCA transform, respectively, for the second set of control points.

component.

See Figure 5.22 for a case in which PCA helped to align images that were mis-registered the first time. See Figure 5.23 for a case wherein PCA produced a much-improved subtraction or difference image.

Significantly higher values of mutual information were obtained for the first PCA component, with a mean increase of 98%. The meaning of this increase is not apparent, since it could be caused by the speckle reduction from selecting this single component, and not by improved registration. There was no significant difference in the MI value when the same, original image data sets were registered directly and by use of the PCA-derived warping transform.

See Figure 5.24 for registration error estimates with and without PCA. These were obtained independently for the two sets of initial control points. In two cases we see a a drastic improvement in the subtraction images and a significant decrease in registration error values; Cyst 1 (Case 1) for the first set of control points, from 1.76 mm to 0.27 mm, and Cancer 2 (Case 6) for the second set of control points, from 4.13 mm to 0.42 mm. The last result is the most important, suggesting greater robustness when the PCA-derived warping transform is employed.

In the other cases the registrations were quite comparable. The difference in error values with and without the use of PCA was not found to be statistically significant by the Wilcoxon signed-rank test.

5.3.5 SRAD: Speckle Reducing Anisotropic Diffusion

Speckle is a type of multiplicative noise that hinders radiologists in their interpretation of ultrasound images. Speckle Reducing Anisotropic Diffusion (SRAD) [Sun et al., 2004, Yu and Acton, 2002] is the edge-sensitive diffusion for speckled images in the same way that conventional anisotropic diffusion [Perona and Malik, 1990] is the edge-sensitive diffusion for images corrupted with additive noise.

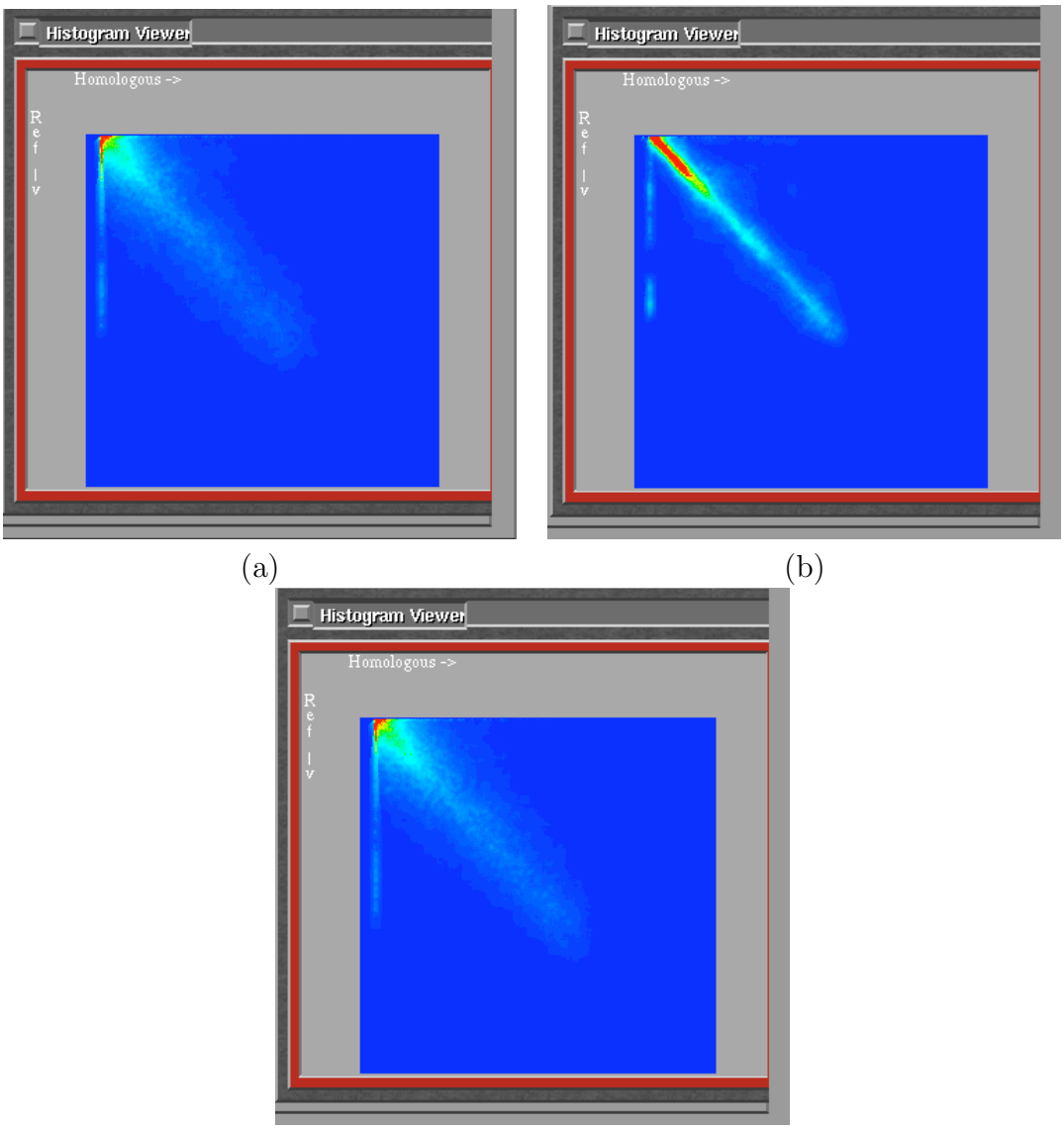

Figure 5.21: (a) Joint 2D histogram of local non-rigid registration on original images. (b) Histogram of registration on PCA first component images. (c) Histogram of registration on original images after applying transform obtained from PCA first component registration.

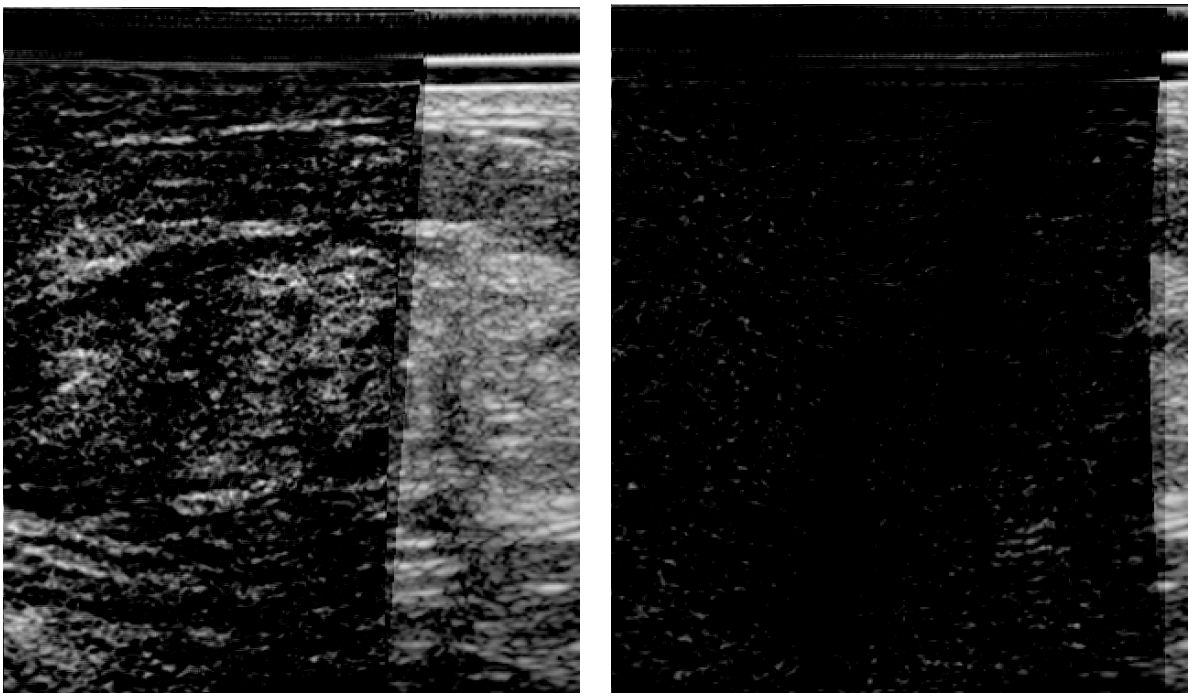

(a) (b)

Figure 5.22: (a) Subtraction image showing differences between original image and registered image for Cancer 2. Bright areas are misregistered sections. (b) Subtraction image showing differences between original image and image registered with PCA first component transform.

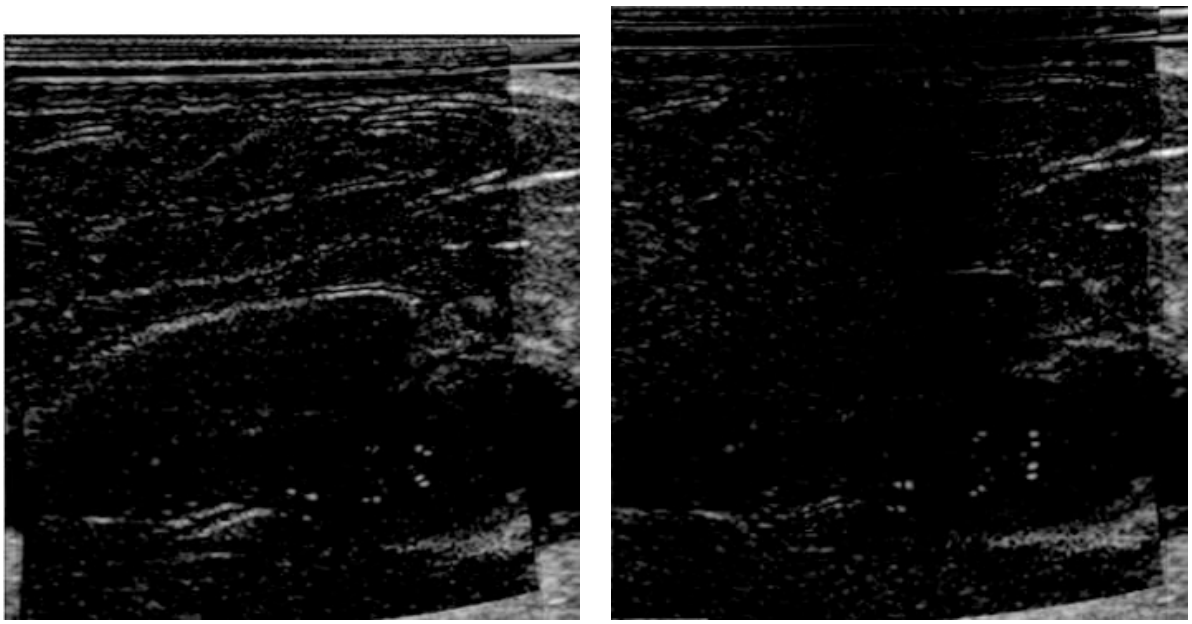

(a) (b)

Figure 5.23: (a) Subtraction image showing differences between original image and registered image for Cyst 4. Bright areas are misregistered sections. (b) Subtraction image showing differences between original image and image registered with PCA first component transform.

Koenderink [Koenderink, 1984] motivates the diffusion equation formulation by stating two criteria:

- Causality.

  Any feature at a coarse level of resolution is required to possess a (not necessarily unique) cause at a finer level of resolution. In other words, no spurious detail should be generated when the resolution is diminished.

- Homogeneity and Isotropy.

  The blurring is required to be space invariant.

The essential idea is: embed the original image in a family of derived images I(x, y, t) obtained by convolving the original image I_o(x, y) with a Gaussian kernel G(x, y; t) of variance t:

$$\mathrm{I(x, y, t) = I_o(x, y)G(x, y; t)} \tag{5.8}$$

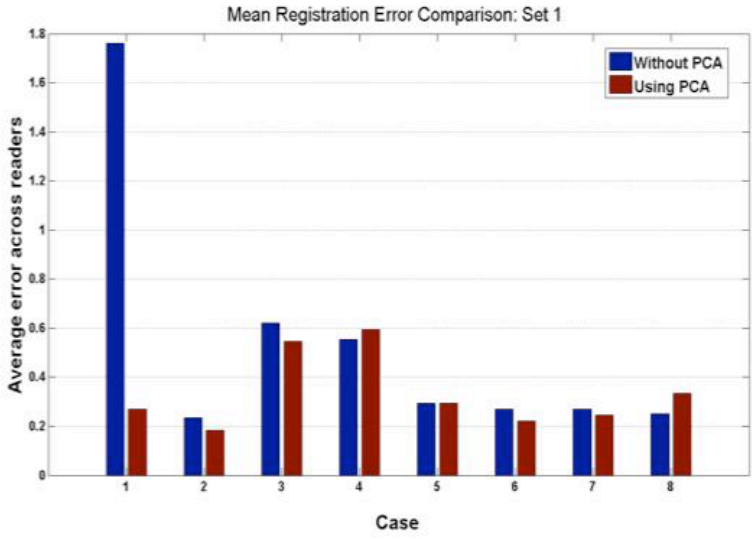

(a)

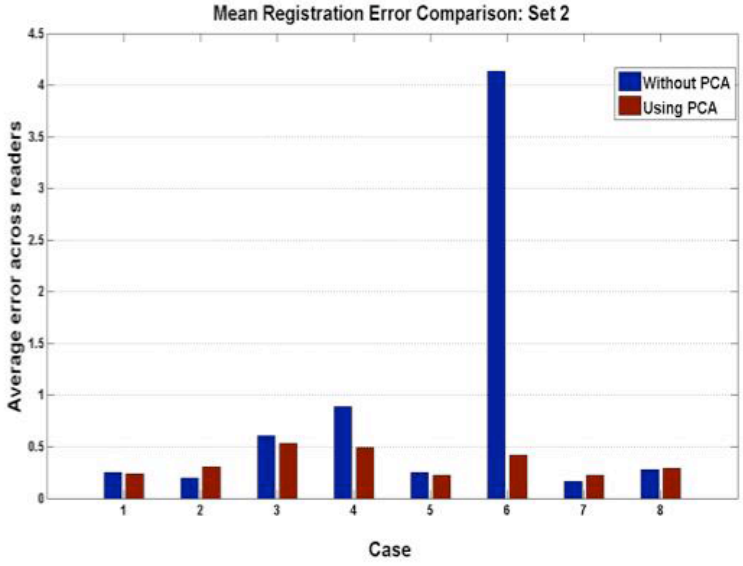

(b)

Figure 5.24: (a) Bar graph showing registration error with and without the use of PCA, for the first set of control points. (b) Bar graph showing registration error with and without the use of PCA, for the second set of control points.

$$I_t = \mathrm{div}(c(x, y, t)\nabla I) = c(x, y, t)\Delta I + \nabla c \nabla I \tag{5.9}$$

We would want to encourage smoothing within a region in preference to smoothing across the boundaries. This could be achieved by setting the conduction coefficient to be 1 in the interior of each region and 0 at the boundaries. The blurring would then take place separately in each region with no interaction between regions. The region boundaries would remain sharp.

SRAD) was applied to smooth images with limited success (see Figures 5.25-5.27). Registration was attempted as in Section 5.2.4, but initial results were not promising. However, it may be possible to obtain better results by using a greater range of the variance step size, i.e., parameter 'Δt' (the value used was 0.05) or changing the pixel step size 'h' (see Appendix 1). The author found that increasing 'h' to values of 3 or more caused unacceptable blurring.

See Appendix 1 for relevant equations.

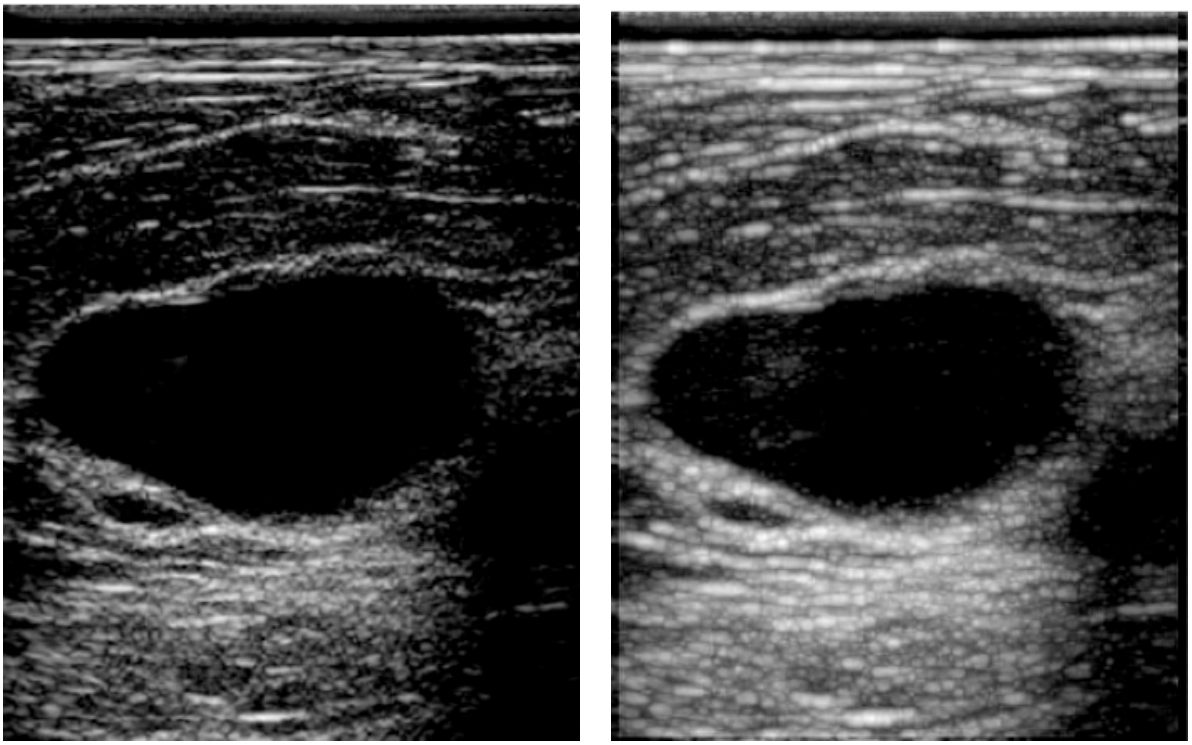

(a) (b)

Figure 5.25: (a) Original cyst image: XY. (b) 3D SRAD with 90 iterations: XY. (All images scaled to max/5: max, 100 z-slices used.)

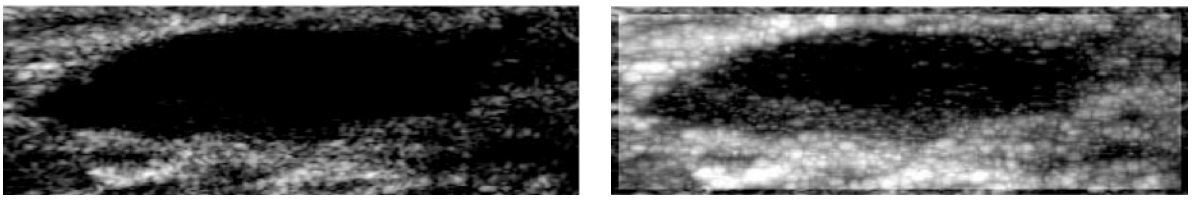

(a) (b)

Figure 5.26: (a) Original cyst image: XZ. (b) 3D SRAD with 90 iterations: XZ. (All images scaled to max/5: max, 100 z-slices used.)

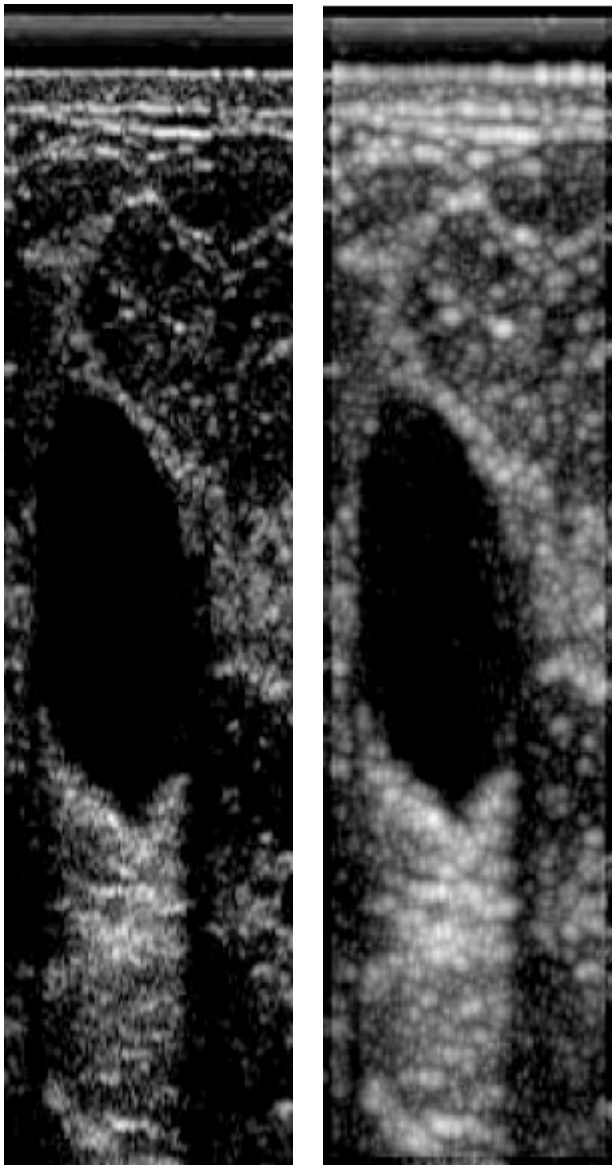

(a) (b)

Figure 5.27: (a) Original cyst image: YZ. (b) 3D SRAD with 90 iterations: YZ. (All images scaled to max/5: max, 100 z-slices used.)

5.4 Conclusion

We have shown that machine learning was able to identify and classify the regions of corrupted data accurately on a breast-mimicking phantom, and also that it could identify specific artifacts on *in vivo* breast images. Opposed view registration was more robust on segmented images of the breast phantom. Also, on *in vivo* breast images, results imply that principal components or other speckle reduction algorithms may be useful in registration of locally warped breast ultrasound images that are partially obscured by noise.

CHAPTER VI

Future Work

We are refining the technical aspects of automated ultrasound scanning and dual-sided scanning in particular. A rubber 'gel dam' was utilized to contain ultrasound gel at the periphery of the breast for the duration of the scan. A molded transducer holder that holds the transducer rigidly in place replaced our older sharp-edged holder that required rubber padding for stiffness. Also, the mesh paddle currently used for scanning is an improvement on the 2.5 mm TPX [4-methylpentene-1 based polyolefin] paddle used in early patient scans, as it does not attenuate and distort the ultrasound beam to the same extent. Additionally, the fiber mesh does not degrade the quality of X-ray images significantly. This work is being prepared for publication.

Six readers have participated in extensive clinical trials covering 52 cases. These trials are being conducted on the benefits of combining digital breast tomosynthesis with registered automated ultrasound (AUS). In this study, the location of the mass on the tomosynthesis image is indicated, to prevent confusion with other masses. Hence, this is more or less a test of how registered AUS contributes to the diagnosis made with tomosynthesis, and not a test of the effectiveness of tomosynthesis as compared to mammography.

This dissertation describes an experimental study on a breast-mimicking phantom, but dual-sided data is not yet available on human subjects. To scan

patients with dual-sided ultrasound imaging, we are currently modifying an Instrumentarium X-Ray unit. Mesh paddles will hold the breast on both sides and scans will initially be conducted with GE's M12L transducer, although we will transition to a lower profile transducer eventually. As for image processing prior to registering and fusing the two sides, to implement principal component analysis(PCA) for 3D image volumes, it may be necessary to exclude fifteen slices at each end of the whole breast image stack (usually 300 slices or more in size) from the registration process. The control points for the PCA transform cannot lie in these slices. However, the resultant warp transform would probably still be an improvement upon the the transform obtained for the original image stack. Smaller subsets of the data could possibly be used for PCA projections instead of 30-slice sets to include end slices in the PCA registration. PCA has not been carried out on 3D images of the breast phantom and this would be a good starting point. Also, PCA and other smoothing techniques such as anisotropic diffusion may compensate for the variation in the accuracy of 3D non-linear registration caused by manual control point selection, and this aspect can be explored further.

Since the machine learning classifier has been trained to identify corrupt data on single-sided images, it can be used on early cases for data differentiation. Classification could be implemented for different-sized regions of interest (ROIs), instead of the fixed sizes used in this work. A finer grid would allow for the detection of more jagged and irregular shadow shapes. A moving grid that does not require fixed centers for the ROIs would be even more flexible. However, the ROI size should not be smaller than the speckle spot size for the ultrasound beam. If this were the case, the features such as mean, standard deviation etc. would not accurately render the nature of the data. Ideally, one could incorporate data classification in the registration itself and run the entire process on one platform. Lastly, presentation of the images is crucial to the radiologist's understanding and ability to interpret the

information at hand. A feasible set-up would be to display both dual sided original image volumes in one window, with a slider that switches from the top view to the bottom view, while displaying the fused image volume in another window. Artifacts such as posterior acoustic shadows and enhancements that are not visible on this image can be evaluated on the original image views. These artifacts do aid in the diagnosis of cancers and cysts, although their elimination allows for a clearer picture of what lies beneath the mass causing the artifact. One very important application of dual-sided imaging is the estimation of the lower margins (i.e., distal to the transducer) of a cancer. These margins are usually obscured by shadowing from the upper part of the cancer.

APPENDIX A

Appendix: Equations for Speckle Reducing Anisotropic Diffusion

Instantaneous coefficient of variation:

$$q = \sqrt{\frac{(\frac{1}{3})(\frac{|\nabla|}{I})^2 - (\frac{1}{6})^2(\frac{|\nabla|^2 I}{I})^2}{1 + \frac{1}{6}(\frac{|\nabla|^2 I}{I})^2}} \tag{A.1}$$

Speckle Scale function:

$$q_o(t) = \lambda \frac{\int\int q^2(x, y; t)dxdy}{\int\int dxdy} \tag{A.2}$$

Diffusion Coefficient:

$$c(q) = \frac{1}{1 + \frac{[q^2(x,y,z;t) - {q_o}^2(t)]}{{q_o}^2(t)(1+{q_o}^2(t))}} \tag{A.3}$$

Calculation of Laplacian:

$$\nabla^2 {I^n}_{i,j,k} = \frac{{I^n}_{i+1,j,k} + {I^n}_{i-1,j,k} + {I^n}_{i,j+1,k} + {I^n}_{i,j-1,k} + {I^n}_{i,j,k+1} + {I^n}_{i,j,k-1} - 6{I^n}_{i,j,k}}{h^2} \tag{A.4}$$

Divergence:

$$\mathrm{d^n_{i,j,k}} = \frac{1}{\mathrm{h}^2}[\mathrm{c^n_{i+1,j,k}}(\mathrm{I^n_{i+1,j,k}} - \mathrm{I^n_{i,j,k}}) +$$

$$c^n_{i,j,k}(I^n{}_{i-1,j,k} - I^n{}_{i,j,k}) + c^n{}_{i,j+1,k}(I^n{}_{i,j+1,k} - I^n{}_{i,j,k}) + c^n{}_{i,j,k}(I^n{}_{i,j-1,k} - I^n{}_{i,j,k}) +$$

$$c^n{}_{i,j,k+1}(I^n{}_{i,j,k+1} - I^n{}_{i,j,k}) + c^n{}_{i,j,k}(I^n{}_{i,j,k-1} - I^n{}_{i,j,k}) \quad \text{(A.5)}$$

Iterative implementation:

$$\mathrm{I^{n+1}_{i,j}} = \mathrm{I^n_{i,j}} + \frac{\Delta \mathrm{t}}{6}\mathrm{d^n_{i,j}} \quad \text{(A.6)}$$

BIBLIOGRAPHY

[Abramowitz and Stegun, 1972] Abramowitz, M. and Stegun, I. A., editors (1972). *Handbook of Mathematical Functions with Formulas, Graphs, and Mathematical Tables*. Dover Publications, 9 edition.

[Andre et al., 1999] Andre, M. P., Janee, H. S., Olson, L. K., Lehman, C. D., and A, F. B. (1999). Novel breast imaging techniques using transmission ultrasound. *The Journal of the Acoustical Society of America*, 106:2134–2135.

[Baker et al., 1999] Baker, J. A., Kornguth, P. J., Soo, M. S., Walsh, R., and Mengoni, P. (1999). Sonography of solid breast lesions: observer variability of lesion description and assessment. *AJR Am J Roentgenol*, 172(6):1621–5.

[Booi et al., 2007] Booi, R. C., Krücker, J. F., Goodsitt, M. M., O'Donnell, M., Kapur, A., LeCarpentier, G. L., Roubidoux, M. A., Fowlkes, J. B., and Carson, P. L. (2007). Evaluating thin compression paddles for mammographically compatible ultrasound. *Ultrasound Med Biol*, 33(3):472–82.

[Bookstein, 1997] Bookstein, F. L. (1997). *Morphometric tools for landmark data: geometry and biology*. Cambridge University Press.

[Bude and Tuthill, 2000] Bude, R. O. and Tuthill, T. (2000). Effect of spectacular reflection on out-of-plane ultrasonographic images reconstructed from three-dimensional data sets. *J Ultrasound Med*, 19(6):391–8.

[Burgess et al., 2001] Burgess, A. E., Jacobson, F. L., and Judy, P. F. (2001). Human observer detection experiments with mammograms and power-law noise. *Med Phys*, 28(4):419–37.

[Carson et al., 2004] Carson, P. L., LeCarpentier, G. L., Roubidoux, M. A., Erkamp, R. Q., Fowlkes, J. B., and Goodsitt, M. M. (2004). Physics and technology of ultrasound breast imaging including automated 3d. In Karellas, A. and Giger, M., editors, *Advances in Breast Imaging: Physics, Technology, and Clinical Applications, RSNA Categorical Course in Diagnostic Radiology Physics*, pages 223–232. RSNA.

[Carson et al., 1981] Carson, P. L., Meyer, C. R., Scherzinger, A. L., and Oughton, T. V. (1981). Breast imaging in coronal planes with simultaneous pulse echo and transmission ultrasound. *Science*, 214(4525):1141–3.

[Chan et al., 2005] Chan, H.-P., Wei, J., Sahiner, B., Rafferty, E. A., Wu, T., Roubidoux, M. A., Moore, R. H., Kopans, D. B., Hadjiiski, L. M., and Helvie, M. A. (2005). Computer-aided detection system for breast masses on digital tomosynthesis mammograms: preliminary experience. *Radiology*, 237(3):1075–80.

[Chang et al., 2010] Chang, R.-F., Chang-Chien, K.-C., Takada, E., Huang, C.-S., Chou, Y.-H., Kuo, C.-M., and Chen, J.-H. (2010). Rapid image stitching and computer-aided detection for multipass automated breast ultrasound. *Med Phys*, 37(5):2063–73.

[Claus et al., 2006] Claus, B. E. H., Eberhard, J. W., Schmitz, A., Carson, P. L., Goodsitt, M. M., and Chan, H. P. (2006). *Digital Mammography*, volume 4046, chapter Generalized Filtered Back-Projection Reconstruction in Breast Tomosynthesis, pages 167–174. Springer Berlin / Heidelberg.

[Cleverley et al., 1997] Cleverley, J. R., Jackson, A. R., and Bateman, A. C. (1997). Pre-operative localization of breast microcalcification using high-frequency ultrasound. *Clin Radiol*, 52(12):924–6.

[Conway et al., 1991] Conway, W. F., Hayes, C. W., and Brewer, W. H. (1991). Occult breast masses: use of a mammographic localizing grid for us evaluation. *Radiology*, 181(1):143–6.

[Drukker et al., 2003] Drukker, K., Giger, M. L., and Mendelson, E. B. (2003). Computerized analysis of shadowing on breast ultrasound for improved lesion detection. *Med Phys*, 30(7):1833–42.

[Duric et al., 2007] Duric, N., Littrup, P., Poulo, L., Babkin, A., Pevzner, R., Holsapple, E., Rama, O., and Glide, C. (2007). Detection of breast cancer with ultrasound tomography: first results with the computed ultrasound risk evaluation (cure) prototype. *Med Phys*, 34(2):773–85.

[Eberhard et al., 2006] Eberhard, J. W., Staudinger, P., Smolenski, J., Ding, J., Schmitz, A., and McCoy, J. e. a. (2006). Proceedings of spie; high-speed large-angle mammography tomosynthesis system. 6142(1):61420C–61420C–11.

[Entrekin et al., 2001] Entrekin, R. R., Porter, B. A., Sillesen, H. H., Wong, A. D., Cooperberg, P. L., and Fix, C. H. (2001). Real-time spatial compound imaging: application to breast, vascular, and musculoskeletal ultrasound. *Semin Ultrasound CT MR*, 22(1):50–64.

[Fowler et al., 1990] Fowler, P. A., Casey, C. E., Cameron, G. G., Foster, M. A., and Knight, C. H. (1990). Cyclic changes in composition and volume of the breast during the menstrual cycle, measured by magnetic resonance imaging. *Br J Obstet Gynaecol*, 97(7):595–602.

[Goldberg et al., 1994] Goldberg, B. B., Liu, J. B., and Forsberg, F. (1994). Ultrasound contrast agents: a review. *Ultrasound Med Biol*, 20(4):319–33.

[Gooding et al., 2010] Gooding, M. J., Finlay, J., Shipley, J. A., Halliwell, M., and Duck, F. A. (2010). Three-dimensional ultrasound imaging of mammary ducts in lactating women: a feasibility study. *J Ultrasound Med*, 29(1):95–103.

[Hadjiiski et al., 2004] Hadjiiski, L., Chan, H.-P., Sahiner, B., Helvie, M. A., Roubidoux, M. A., Blane, C., Paramagul, C., Petrick, N., Bailey, J., Klein, K., Foster, M., Patterson, S., Adler, D., Nees, A., and Shen, J. (2004). Improvement in radiologists' characterization of malignant and benign breast masses on serial mammograms with computer-aided diagnosis: an roc study. *Radiology*, 233(1):255–65.

[Helvie et al., 1994] Helvie, M. A., Chan, H. P., Adler, D. D., and Boyd, P. G. (1994). Breast thickness in routine mammograms: effect on image quality and radiation dose. *AJR Am J Roentgenol*, 163(6):1371–4.

[Jackson et al., 1993] Jackson, V. P., Hendrick, R. E., Feig, S. A., and Kopans, D. B. (1993). Imaging of the radiographically dense breast. *Radiology*, 188(2):297–301.

[Joachims, 2008] Joachims, T. (2008). Svm light.

[Jolliffe, 1986] Jolliffe, I. T. (1986). *Principal Component Analysis*. Springer-Verlag.

[Kapur et al., 2004] Kapur, A., Carson, P. L., Eberhard, J., Goodsitt, M. M., Thomenius, K., Lokhandwalla, M., Buckley, D., Roubidoux, M. A., Helvie, M. A., Booi, R. C., LeCarpentier, G. L., Erkamp, R. Q., Chan, H.-P., Fowlkes, J. B., Thomas, J. A., and Landberg, C. E. (2004). Combination of digital mammography with semi-automated 3d breast ultrasound. *Technol Cancer Res Treat*, 3(4):325–34.

[Kelly et al., 2010] Kelly, K. M., Dean, J., Comulada, W. S., and Lee, S.-J. (2010). Breast cancer detection using automated whole breast ultrasound and mammography in radiographically dense breasts. *Eur Radiol*, 20(3):734–42.

[Kim et al., 1997] Kim, B., Boes, J. L., Frey, K. A., and Meyer, C. R. (1997). Mutual information for automated unwarping of rat brain autoradiographs. *Neuroimage*, 5(1):31–40.

[Koenderink, 1984] Koenderink, J. J. (1984). The structure of images. *Biological Cybernetics*, 50(5):363–370.

[Kofler and Madsen, 2001] Kofler, Jr, J. M. and Madsen, E. L. (2001). Improved method for determining resolution zones in ultrasound phantoms with spherical simulated lesions. *Ultrasound Med Biol*, 27(12):1667–76.

[Kolb et al., 1998] Kolb, T. M., Lichy, J., and Newhouse, J. H. (1998). Occult cancer in women with dense breasts: detection with screening us–diagnostic yield and tumor characteristics. *Radiology*, 207(1):191–9.

[Kolb et al., 2002] Kolb, T. M., Lichy, J., and Newhouse, J. H. (2002). Comparison of the performance of screening mammography, physical examination, and breast us and evaluation of factors that influence them: an analysis of 27,825 patient evaluations. *Radiology*, 225(1):165–75.

[Kotropoulos and Pitas, 2003] Kotropoulos, C. and Pitas, I. (2003). Segmentation of ultrasonic images using support vector machines. *Pattern Recognition Letters*, 24:715–727.

[Kotsianos-Hermle et al., 2009] Kotsianos-Hermle, D., Wirth, S., Fischer, T., Hiltawsky, K. M., and Reiser, M. (2009). First clinical use of a standardized three-dimensional ultrasound for breast imaging. *Eur J Radiol*, 71(1):102–8.

[Krücker et al., 2002] Krücker, J. F., LeCarpentier, G. L., Fowlkes, J. B., and Carson, P. L. (2002). Rapid elastic image registration for 3-d ultrasound. *IEEE Trans Med Imaging*, 21(11):1384–94.

[Krücker et al., 2000] Krücker, J. F., Meyer, C. R., LeCarpentier, G. L., Fowlkes, J. B., and Carson, P. L. (2000). 3d spatial compounding of ultrasound images using image-based nonrigid registration. *Ultrasound Med Biol*, 26(9):1475–88.

[LeCarpentier et al., 1999] LeCarpentier, G. L., Tridandapani, P. B., Fowlkes, J. B., Roubidoux, M. A., Moskalik, A. P., and Carson, P. L. (1999). Utility of 3d ultrasound in the discrimination and detection of breast cancer.

[Lehman et al., 2000] Lehman, C. D., André, M. P., Fecht, B. A., Johansen, J. M., Shelby, R. L., and Shelby, J. O. (2000). Through-transmission us applied to breast imaging. *Acad Radiol*, 7(2):100–7.

[Lister et al., 1998] Lister, D., Evans, A. J., Burrell, H. C., Blamey, R. W., Wilson, A. R., Pinder, S. E., Ellis, I. O., Elston, C. W., and Kollias, J. (1998). The accuracy of breast ultrasound in the evaluation of clinically benign discrete, symptomatic breast lumps. *Clin Radiol*, 53(7):490–2.

[Madsen et al., 2006] Madsen, E. L., Berg, W. A., Mendelson, E. B., Frank, G. R., and Investigators for ACRIN Protocol 6666 (2006). Anthropomorphic breast phantoms for qualification of investigators for acrin protocol 6666. *Radiology*, 239(3):869–74.

[Madsen et al., 1982] Madsen, E. L., Zagzebski, J. A., and Frank, G. R. (1982). An anthropomorphic ultrasound breast phantom containing intermediate-sized scatterers. *Ultrasound Med Biol*, 8(4):381–92.

[Meyer et al., 1999] Meyer, C. R., Boes, J. L., Kim, B., Bland, P. H., Lecarpentier, G. L., Fowlkes, J. B., Roubidoux, M. A., and Carson, P. L. (1999). Semiautomatic registration of volumetric ultrasound scans. *Ultrasound Med Biol*, 25(3):339–47.

[Meyer et al., 1997] Meyer, C. R., Boes, J. L., Kim, B., Bland, P. H., Zasadny, K. R., Kison, P. V., Koral, K., Frey, K. A., and Wahl, R. L. (1997). Demonstration of accuracy and clinical versatility of mutual information for automatic multimodality image fusion using affine and thin-plate spline warped geometric deformations. *Med Image Anal*, 1(3):195–206.

[Moskalik et al., 1995] Moskalik, A., Carson, P. L., Meyer, C. R., Fowlkes, J. B., Rubin, J. M., and Roubidoux, M. A. (1995). Registration of three-dimensional compound ultrasound scans of the breast for refraction and motion correction. *Ultrasound Med Biol*, 21(6):769–78.

[Moss et al., 1999] Moss, H. A., Britton, P. D., Flower, C. D., Freeman, A. H., Lomas, D. J., and Warren, R. M. (1999). How reliable is modern breast imaging in differentiating benign from malignant breast lesions in the symptomatic population? *Clin Radiol*, 54(10):676–82.

[Nagashima et al., 2005] Nagashima, T., Hashimoto, H., Oshida, K., Shigeharu, N., Tanabe, N., and Nikaido, T. e. a. (2005). Ultrasound demonstration of mammographically detected microcalcifications in patients with ductal carcinoma in situ of the breast. *Breast Cancer*, 12(3):216–220.

[Narayanasamy et al., 2007] Narayanasamy, G., LeCarpentier, G. L., Zabuawala, S., Fowlkes, J. B., Roubidoux, M., Sinha, S., and Carson, P. L. (2007). Non-rigid registration of three-dimensional (3d) grayscale and doppler ultrasound breast images. *Conf Proc IEEE Eng Med Biol Soc*, 2007:91–4.

[NIH, 2010] NIH (2010). Imagej.

[Novak, 1983] Novak, D. (1983). Indications for and comparative diagnostic value of combined ultrasound and x-ray mammography. *Eur J Radiol*, 3 Suppl 1:299–302.

[Perona and Malik, 1990] Perona, P. and Malik, J. (1990). Scale-space and edge detection using anisotropic diffusion. *IEEE Transactions on pattern analysis and machine intelligence*, 12:629–639.

[Piliouras et al., 2004] Piliouras, N., Kalatzis, I., Dimitropoulos, N., and Cavouras, D. (2004). Development of the cubic least squares mapping linear-kernel support vector machine classifier for improving the characterization of breast lesions on ultrasound. *Comput Med Imaging Graph*, 28(5):247–55.

[Richter et al., 1997] Richter, K., Heywang-Köbrunner, S. H., Winzer, K. J., Schmitt, K. J., Prihoda, H., Frohberg, H. D., Guski, H., Gregor, P., Blohmer, J. U., Fobbe, F., Döinghaus, K., Löhr, G., and Hamm, B. (1997). Detection of malignant and benign breast lesions with an automated us system: results in 120 cases. *Radiology*, 205(3):823–30.

[Rizzatto et al., 1997] Rizzatto, G., Chersevani, R., Abbona, M., Lombardo, V. L., and Macorig, D. (1997). High-resolution sonography of breast carcinoma. *Eur J Radiol*, 24(1):11–9.

[Roubidoux et al., 2005] Roubidoux, M. A., LeCarpentier, G. L., Fowlkes, J. B., Bartz, B., Pai, D., Gordon, S. P., Schott, A. F., Johnson, T. D., and Carson, P. L. (2005). Sonographic evaluation of early-stage breast cancers that undergo neoadjuvant chemotherapy. *J Ultrasound Med*, 24(7):885–95.

[Sahiner et al., 2007] Sahiner, B., Chan, H.-P., Roubidoux, M. A., Hadjiiski, L. M., Helvie, M. A., Paramagul, C., Bailey, J., Nees, A. V., and Blane, C. (2007). Malignant and benign breast masses on 3d us volumetric images: effect of computer-aided diagnosis on radiologist accuracy. *Radiology*, 242(3):716–24.

[Saslow et al., 2007] Saslow, D., Boetes, C., Burke, W., Harms, S., Leach, M. O., Lehman, C. D., Morris, E., Pisano, E., Schnall, M., Sener, S., Smith, R. A., Warner, E., Yaffe, M., Andrews, K. S., Russell, C. A., and American Cancer Society Breast Cancer Advisory Group (2007). American cancer society guidelines for breast screening with mri as an adjunct to mammography. *CA Cancer J Clin*, 57(2):75–89.

[Seidel et al., 1997] Seidel, H., Herzel, H., and Eckberg, D. L. (1997). Phase dependencies of the human baroreceptor reflex. *Am J Physiol*, 272(4 Pt 2):H2040–53.

[Shipley et al., 2005] Shipley, J. A., Duck, F. A., Goddard, D. A., Hillman, M. R., Halliwell, M., Jones, M. G., and Thomas, B. T. (2005). Automated quantitative volumetric breast ultrasound data-acquisition system. *Ultrasound Med Biol*, 31(7):905–17.

[Sickles et al., 2005] Sickles, E. A., Miglioretti, D. L., Ballard-Barbash, R., Geller, B. M., Leung, J. W. T., Rosenberg, R. D., Smith-Bindman, R., and Yankaskas, B. C. (2005). Performance benchmarks for diagnostic mammography. *Radiology*, 235(3):775–90.

[Sinha et al., 2010] Sinha, S., Hooi, F., Syed, Z., Pinsky, R., and Carson, P. (2010). Machine learning for noise removal on breast ultrasound images (accepted). *IEEE Transactions on Ultrasonics, Ferroelectrics and Frequency Control*.

[Sinha et al., 2007a] Sinha, S. P., Goodsitt, M. M., Roubidoux, M. A., Booi, R. C., LeCarpentier, G. L., Lashbrook, C. R., Thomenius, K. E., Chalek, C. L., and Carson, P. L. (2007a). Automated ultrasound scanning on a dual-modality breast imaging system: coverage and motion issues and solutions. *J Ultrasound Med*, 26(5):645–55.

[Sinha et al., 2009] Sinha, S. P., Narayanan, R., Ma, B., Roubidoux, M. A., Liu, H., and Carson, P. L. (2009). Image registration for detection and quantification of change on digital tomosynthesis mammographic volumes. *AJR Am J Roentgenol*, 192(2):384–7.

[Sinha et al., 2007b] Sinha, S. P., Roubidoux, M. A., Helvie, M. A., Nees, A. V., Goodsitt, M. M., LeCarpentier, G. L., Fowlkes, J. B., Chalek, C. L., and Carson,

P. L. (2007b). Multi-modality 3d breast imaging with x-ray tomosynthesis and automated ultrasound. volume 2007, pages 1335–8.

[Sommer et al., 2003] Sommer, H. L., Janni, B., Rack, B., Klanner, E., Strobl, B., and Rammel, G. e. a. (2003). Average tumor size and overall survival of patients with primary diagnosis of breast cancer influenced by a more frequent use of mammography. volume 22, page abstr 3487.

[Stacey-Clear et al., 1993] Stacey-Clear, A., McCarthy, K. A., Hall, D. A., Pile-Spellman, E., White, G., Hulka, C. A., Whitman, G. J., Halpern, E. F., and Kopans, D. B. (1993). Mammographically detected breast cancer: location in women under 50 years old. *Radiology*, 186(3):677–80.

[Stavros et al., 1995] Stavros, A. T., Thickman, D., Rapp, C. L., Dennis, M. A., Parker, S. H., and Sisney, G. A. (1995). Solid breast nodules: use of sonography to distinguish between benign and malignant lesions. *Radiology*, 196(1):123–34.

[Sun et al., 2004] Sun, Q., Hossack, J. A., Tang, J., and Acton, S. T. (2004). Speckle reducing anisotropic diffusion for 3d ultrasound images. *Comput Med Imaging Graph*, 28(8):461–70.

[Taylor et al., 2002] Taylor, K. J. W., Merritt, C., Piccoli, C., Schmidt, R., Rouse, G., Fornage, B., Rubin, E., Georgian-Smith, D., Winsberg, F., Goldberg, B., and Mendelson, E. (2002). Ultrasound as a complement to mammography and breast examination to characterize breast masses. *Ultrasound Med Biol*, 28(1):19–26.

[Tozaki et al., 2010] Tozaki, M., Isobe, S., Yamaguchi, M., Ogawa, Y., Kohara, M., Joo, C., and Fukuma, E. (2010). Optimal scanning technique to cover the whole breast using an automated breast volume scanner. *Jpn J Radiol*, 28(4):325–8.

[Treece et al., 2007] Treece, G. M., Gee, A. H., and Prager, R. W. (2007). Ultrasound compounding with automatic attenuation compensation using paired angle scans. *Ultrasound Med Biol*, 33(4):630–42.

[van Wijk and Thijssen, 2002] van Wijk, M. C. and Thijssen, J. M. (2002). Performance testing of medical ultrasound equipment: fundamental vs. harmonic mode. *Ultrasonics*, 40(1-8):585–91.

[Vapnik, 1999] Vapnik, V. N. (1999). An overview of statistical learning theory. *IEEE Trans Neural Netw*, 10(5):988–99.

[Wenkel et al., 2008] Wenkel, E., Heckmann, M., Heinrich, M., Schwab, S. A., Uder, M., Schulz-Wendtland, R., Bautz, W. A., and Janka, R. (2008). Automated breast ultrasound: lesion detection and bi-rads classification–a pilot study. *Rofo*, 180(9):804–8.

[WHO, 2009] WHO (2009). Who cancer statistics.

[Widrow and Lehr, 1990] Widrow, B. and Lehr, M. (1990). 30 years of adaptive neural networks: Perceptron, madaline, and backpropagation. volume 78, pages 1415–1442.

[Yu and Acton, 2002] Yu, Y. and Acton, S. T. (2002). Speckle reducing anisotropic diffusion. *IEEE Trans Image Process*, 11(11):1260–70.

[Zhang et al., 2006] Zhang, Y., Chan, H.-P., Sahiner, B., Wei, J., Goodsitt, M. M., Hadjiiski, L. M., Ge, J., and Zhou, C. (2006). A comparative study of limited-angle cone-beam reconstruction methods for breast tomosynthesis. *Med Phys*, 33(10):3781–95.